January 2009

Optical Measurements in Gas-Liquid Stirred Tanks

Sean Mueller
Washington University in St. Louis

WASHINGTON UNIVERSITY IN ST. LOUIS

School of Engineering and Applied Science

Department of Energy, Environmental and Chemical Engineering

Dissertation Examination Committee:
Milorad Dudukovic, Chair
Muthanna Al-Dahhan, Co-Chair
John Gleaves
David Peters
Palghat Ramachandran
Bala Subramaniam
Susan Williams

OPTICAL MEASUREMENTS IN

GAS-LIQUID STIRRED TANKS

by

Sean G. Mueller

**A dissertation presented to the Graduate School of Arts and Sciences
of Washington University in partial fulfillment of the
requirements for the degree of**

DOCTOR OF PHILOSPHY
August 2009
Saint Louis, Missouri

ABSTRACT OF THE DISSERTATION

Optical Measurements in Gas-Liquid Stirred Tanks

by

Sean G. Mueller

Doctor of Philosophy in Energy, Environmental and Chemical Engineering

Washington University in St. Louis, 2009

Research Advisor: Professor Milorad Dudukovic

This dissertation outlines the development of novel, in-situ and relatively inexpensive optical measurement techniques for use in opaque multiphase reactors at elevated temperature (350 °C) and pressure (180 bar) environments where conventional measurement techniques either cannot be used or are difficult or expensive to implement. Important parameters (such as gas holdup, specific interfacial area, bubble velocity, bubble chord lengths, liquid level, and phase transition) in opaque, multiphase reactors at industrially relevant conditions are lacking in the literature.

A miniaturized 4-point probe is developed and methodology outlined that can simultaneously capture local gas holdup, interfacial area, size, and velocities of bubbles in a multiphase stirred tank reactor where small bubble sizes can be expected, especially at elevated pressures and/or high agitation rates. The miniaturized 4-point probe

accurately captures bubble dynamics of bubbles as small as 850 microns at elevated temperature and pressure.

Single-point probes are also developed that are moveable under high pressure that can measure liquid level in a reactor as well as the volumetric expansion of carbon dioxide expanded liquids (CXLs are an emerging green technology). A reflectance-based probe (a 7-fiber, hexagonally packed bundle) that detects critical opalescence and thus the phase transition of complex, multicomponent systems from the subcritical to the supercritical state is also developed for the investigation of CXLs.

Most importantly, detailed instructions for construction of all of the above optical probe technologies are provided in a step-by-step manner.

Acknowledgments

Thanks to Muthanna Al-Dahhan and Milorad Dudukovic for their advising and helping me form this dissertation.

Special thanks to the National Science Foundation Engineering Research Centers Program, Grant EEC-0310689 and the Chemical Reaction Engineering Laboratory for their financial support.

Dedicated to John Gleaves for starting me on this path; to Bala Subramaniam and Susan Williams for allowing me to grow in the REU programs at KU; to Muthanna Al-Dahhan, Palghat Ramachandran and Milorad Dudukovic for welcoming me into CREL and for their guidance; to Andrea Heugatter, John Kardos, James McKelvey and David Peters for their support through the years; to Steve Picker, Pat Harkins, Jim Linders, Rose Baxter, Mindy Price, Jean Kirby, and Ruth Hartstein for all their invaluable help; to all my fellow graduate students and researchers, especially Vesna Havran, Chengtian Wu, Rajneesh Varma, Radmila Jevtic, Arnaud Denecheau, Dan Combest, Pablo Vasquez, Bia Thomas, Xiaolin Zheng, Subramanya Nayak, Zeljko Kuzeljevic, Evgeniy Redekop, Mohamed Awad, Ahmed Youssef, Debangshu Guha, Petar Rakocevic, Adam Wehrmeister, Rebecca Fushimi, Mike Rude and Dave French, for carrying me along the way; to my family and friends for their constant support; to Monsignor Charles McGlinn for his encouragement from my youth; and to my Mother for being my font of wisdom and my cornerstone. This would not have been possible without each and every one of you. Thank you!

<div align="right">Sean G. Mueller</div>

Washington University in St. Louis
August 2009

Contents

Notation

<u>Uppercase</u>

D	–	impeller diameter (cm)
Fl	–	flow number (dimensionless)
Fr	–	Froude number (dimensionless)
H	–	height of ungassed liquid level in reactor (cm)
L	–	chord length (cm)
N	–	rotations per second
P	–	pressure (bar)
Q	–	gas flow rate (L/min)
R	–	radius of reactor (cm)
Re	–	Reynolds number (dimensionless)
T	–	radius of reactor (cm) or temperature (°C)
U	–	velocity (cm/s)
U_{tip}	–	impeller tip speed (cm/s)
V	–	volume (L)
VE	–	volumetric expansion (%)

<u>Lowercase</u>

a	–	specific interfacial area (cm^2/cm^3)
d_{32}	–	Sauter mean diameter
n	–	normal of a surface or refractive index
r	–	radial distance from the center of the tank (cm)
t	–	time (sec)
v	–	bubble velocity (cm/s)
x, y, z	–	coordinates
z	–	height from base of reactor (cm)

<u>Subscript</u>

avg	–	average
c	–	critical
exp	–	experimental
i	–	counter
local	–	local location in the reactor
G	–	gas
L	–	liquid
T	–	tank
0	–	central probe tip or reference state
1	–	tip one

| 2 | – | tip two |
| 3 | – | tip three |

Greek

ε	–	gas holdup (%)
θ	–	angle of incidence between the axis of the probe and the bubble velocity vector (°)
ϕ	–	angle between the bubble velocity vector and normal vector from the bubble surface (°)
φ	–	angle of approach (°)

Abbreviations

3-D	–	three dimensional
BSD	–	bubble size distribution
CFD	–	computational fluid dynamics
COP	–	critical opalescence probe
CT	–	computed tomography
CXL	–	carbon dioxide expanded liquid
ET	–	electrical tomography
G	–	gas
HPLC	–	high-performance liquid chromatography
ID	–	inner diameter (cm)
L	–	liquid
LDA	–	laser Doppler anemometry
LDV	–	laser Doppler velocimetry
MRI	–	magnetic resonance imaging
NMR	–	nuclear magnetic resonance
OD	–	outer diameter
PDA	–	phase Doppler anemometry
PEPT	–	postitron emission particle tracking
PIV	–	particle image velocimetry
rpm	–	rotations per minute
RPT	–	radioactive particle tracking
S	–	solid
SIA	–	specific interfacial area
SS	–	stainless steel
ST	–	stirred tank
X	–	times

List of Figures

xi

Chapter 1

Multiphase Reactors and Challenges in Stirred Tank Reactors

1.1   Introduction to Multiphase Reactors

Multiphase reactors are used throughout the petroleum, chemical, mining, biochemical

and pharmaceutical industries to contact reactants that are in different phases – gas (G),

liquid (L), and solid (S).
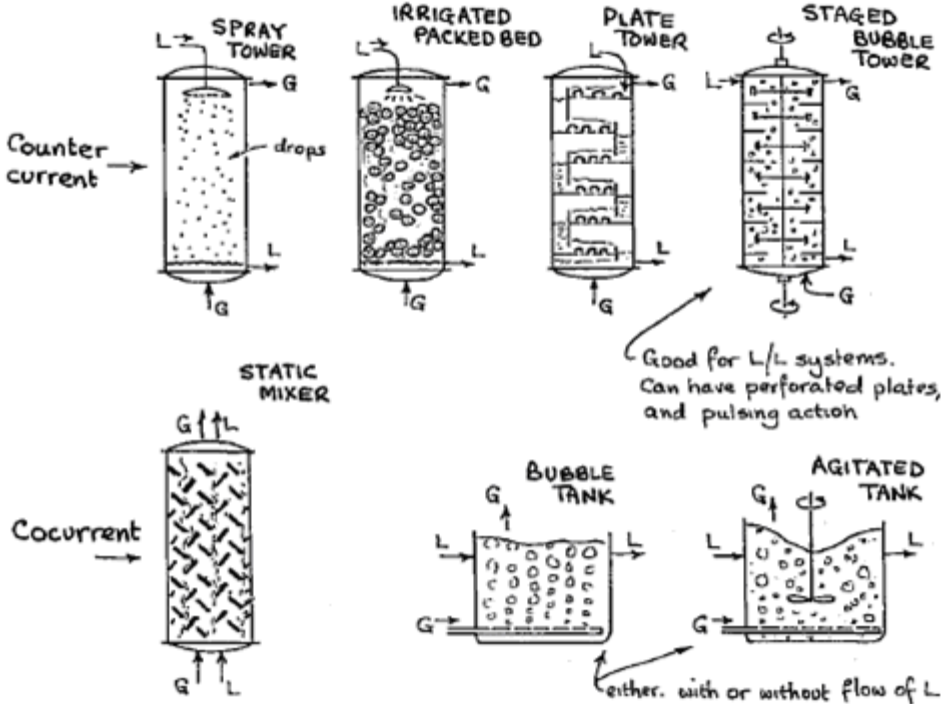
Figure 1.1: Common G-L reactors (Source: Levenspiel, 2002)

1

Stirred tanks (shown in the bottom right in Figure 1.1) are used widely in chemical production (polymerization, alkylation, oxidation, chlorination, fermentation etc.) because they reliably allow for high levels of backmixing, for efficient contacting between liquid and gas to ensure good mass transfer, for the suspension of solids, and for ease of heat transfer leading to isothermal operation. However, in systems that are highly reactive or contain very active catalysts, it is often difficult to remove mass transfer limitations, which can adversely affect the rate of reaction. Poor yields and reduced selectivities due to inefficient mixing can cause excessive production of byproducts requiring disposal or unproductive downstream processing, excessive separation costs, greater use of harsh solvents – all of which reduce profitability of the process and create a large environmental footprint.

The ability to understand, properly model and design fluid flow within a multiphase stirred tank (ST) would allow for better reactor scale-up and therefore maximize reactor performance and decrease waste due to inadequate reactor design. More than 15 years ago, Tatterson et al. (1991) estimated that nearly half of the $750 billion annual output from the chemical industry alone passed through a ST at one point and that losses incurred by inadequate reactor design were on the order of tens of billions of dollars. Unfortunately, things have not improved much in the past couple of decades.

1.2   Challenges in STs

There are three challenges in the realm of multiphase stirred tank reactors:

- Scale-up

- Computational Fluid Dynamic Modeling

- Implementation of Green Engineering in Reactor Design Principles

Reactor scale-up – from the laboratory scale reactor, to the pilot plant reactor, and all the way up to the industrial scale reactor – is the single biggest challenge with multiphase reactors. As reactors are scaled up to larger sizes geometric, bubble, mixing and kinetic lengths and characteristic times do not scale in proportion. Otherwise, we would see chemical plants that look something like that shown in Figure 1.2.
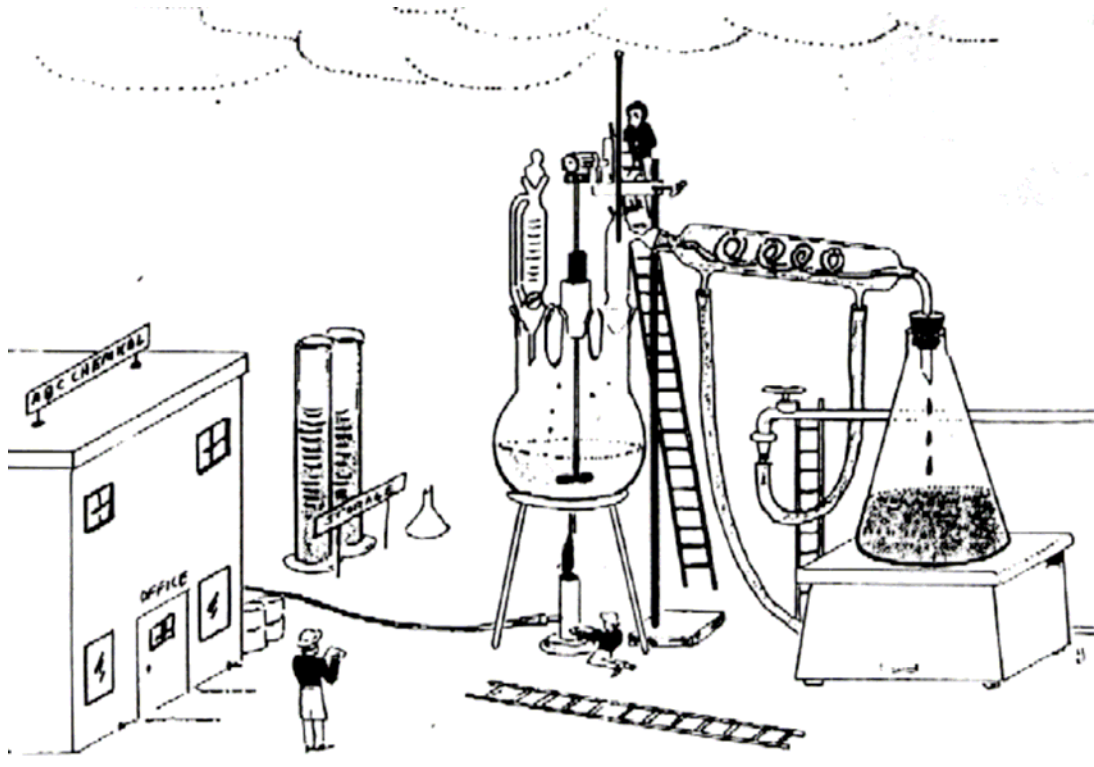
Figure 1.2: "The bench scale results were so good we that we by-passed the pilot plant."
(Source: Stitt, 2002)

Rather than beginning with the mass, energy, and momentum transport equations within a multiphase stirred tank, flow models with empirical correlations are generally used to describe the multiphase flow in the reactor. This approach has provided a foundation for reactor design and scale-up; however, care must be taken that the correlations are appropriately used. The empirical information available for modeling usually describes global properties in the system of interest (overall gas holdup, etc.) but often does not provide the detailed information regarding local properties that are important for the design and scale-up of process equipment.

In the age of ever increasing computing power, computational fluid dynamic (CFD) models have been developed to provide quantitative descriptions of flows in multiphase STs. Yet, even the most powerful CFD models require experimental validation. D. Guha (Guha, 2007; Guha et al., 2006; Guha et al., 2007; and Guha et al., 2008) developed a CFD-based model for single-phase (liquid) flow and reactions in a ST. The Fluent®-computed Euler-Euler flow model was validated by experiments and showed that decoupling of the momentum balance and species balance becomes possible when the interacting cell model for the ST is based on the information obtained from CFD. While the same approach is, in principle, possible in multiphase STs, difficulties arise in validating and improving the CFD codes. Guha et al. (2008) have shown that current CFD attempts fail to properly capture flows in liquid-solid systems and Rammohan et al. (Rammohan, 2002 and Khopkar et al., 2005) have documented the same for gas-liquid STs. Clearly, more experimental evidence is essential for guiding the

4

improvement in the CFD codes. It is on this experimental front that data for G-L STs is lacking – especially concerning bubble dynamics. CFD models are inadequate, and there simply is not enough data to empower the predictive capabilities of CFD for multiphase stirred tank reactors (Scargiali et al., 2007; Sommerfield & Dekker, 2004; and Joshi & Ranade, 2003).

With the rising government regulation and global awareness of the type and scale of industrial impact on the environment, green engineering has rightly moved to the forefront in the design of chemical processes. To transform the manufacture and use of chemicals into inherently safe, ecologically responsible, and economically viable processes, one of the visions of the green engineering is to either eliminate or significantly replace the harsh, conventional mineral acids as well as organic and chlorinated solvents used in catalytic processes with benign solvents such as carbon dioxide. Dense phase carbon dioxide (CO_2), including liquid and supercritical CO_2, has been gaining acceptance for potential use in industrial applications due to benefits of pressure-tunable density and transport properties, ease of separation, solvent replacement, enhanced miscibility of reactants, optimized catalyst activity, and increased product selectivities, all of which decrease waste and pollution (Wei et al., 2002; Musie et al., 2001). Carbon dioxide expanded liquids (CXL's) also provide the benefit up of to 80% solvent replacement with dense phase carbon dioxide. However, the basic information – such as how much organic solvent can be replaced with CO_2 at a given

condition or when the supercritical phase change occurs in the mixture – is scant in the literature.

To add to the complexity of investigating G-L STs, most of the experimental thrusts in the literature use techniques that either require transparent vessels operating at low gas holdups, or are often expensive, or can be used only under limited conditions (Laakonen et al., 2005a; Laakonen et al., 2005b; Machon et al., 1997; Boden et al., 2008; Alves et al., 2002; Thatte et al., 2004; Wang et al., 2006a; Sun et al., 2006; Schafer et al., 2000; Khopkar et al., 2005; Paglianti et al., 2001; Nassar et al., 2004; Montante et al., 2007; Lu and Ju, 1986; Hu et al., 2006; Bombac et al., 1997; and Sudiyo & Andersson, 2007). Industrial STs are often opaque (stainless steel construction and high holdups) and operate at temperatures and pressures well outside the range of atmospheric conditions – rendering many of the experimental techniques outlined in the literature useless for industrial investigations. Therefore, relatively inexpensive tools are needed that can be used to capture local, quantitative information at industrially relevant conditions.

1.3   Motivation of Research

The thrust of this work is to provide just a few of those investigative tools: innovative, in-situ, optical techniques that can accurately obtain bubble dynamics in a G-L ST, readily track liquid level height to determine the volumetric expansion of CXLs, and determine the phase transition of fluids from the subcritical to the supercritical state –

all across a wide range of operating pressures, temperatures, and fluids. With these tools in hand, the knowledge and understanding of optical probes and G-L STs as well as supercritical and dense phase reactors will be advanced, valuable knowledge for CFD modeling will be provided, and new engineering science will be generated in systems at higher pressures and temperatures never before reported in the literature.

1.4   Objectives of Research

The goals of this work are to:

- Develop an optical probe that can capture the gas holdup, bubble size distribution, velocity distribution and interfacial area of the bubble spectrum commonly encountered in STs.

- Develop a measurement technique to quantify bubble dynamics (gas holdup, size, velocity and interfacial area) in a ST using the optical probe and validate the measurements using borescopy.

- Develop a probe capable of traversing the height of a vessel under high pressure (< 200 barg) to determine the height of the liquid level in an opaque vessel for the determination of volumetric expansion, and investigate the volumetric expansion of some common CXLs.

- Develop a probe capable of accurately and precisely detecting phase transition from a heterogeneous (subcritical) state to a homogeneous (supercritical) state, and investigate common fluids used in CXLs.

7

Chapter 2

Types of Measurement Techniques Used in Multiphase Flows and Basis for Selection of Optical Probes for G-L STs

2.1   Available Measurement Techniques

There is abundant literature on various techniques that have been used to describe the flow in multiphase reactors. Yang et al. (2007) and Boyer et al. (2002) review articles on these techniques give a picture somewhat like that shown below in Figure 2.1.
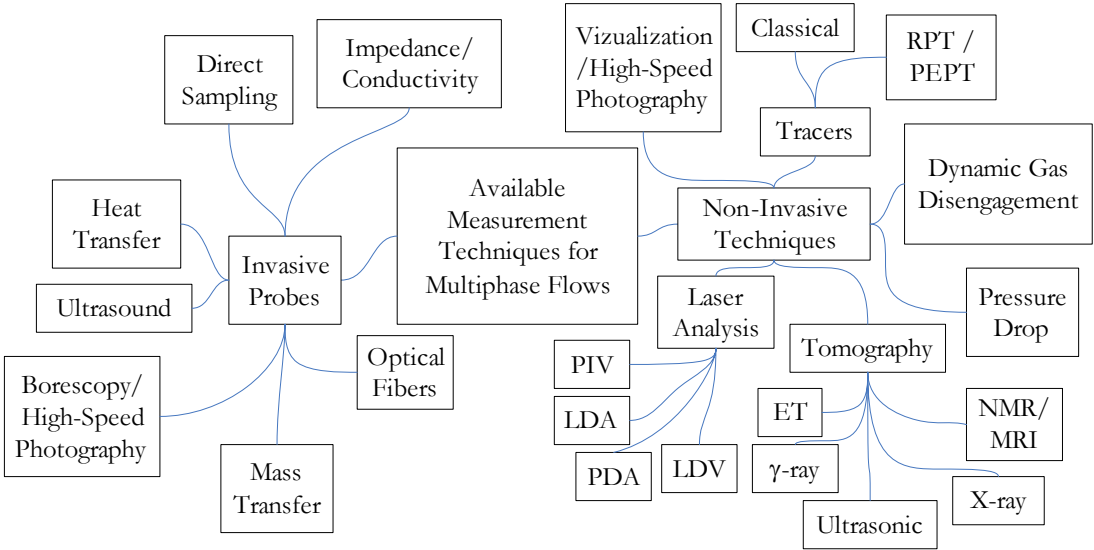
Figure 2.1: Available measurement techniques for multiphase flows

Clearly, there are two options when considering a measurement technique: invasive probes or non-invasive techniques. The former is inserted into the reactor so that it can interact with the flow, and the latter is mounted on or positioned closely to the reactor in order to obtain information about the flow without directly interacting with the flow. Each option and subsequent technique has its own tradeoff.

2.1.1   Non-Invasive Techniques

While non-invasive techniques do not disturb the flow within the reactor, they can have significant limitations (cost, difficult to learn or setup, safety regulations, etc.). For example, the laser techniques such as Particle Image Velocimetry (PIV), Laser Doppler Velocimetry (LDV), Laser Doppler Anemometry (LDA), and Phase Doppler Anemometry (PDA) can obtain very accurate information in a multiphase system (holdup, bubble or particle dynamics in the micron and millimeter size range, liquid velocity, etc.) and have been used extensively throughout the literature (Chen and Fan, 2002; Delnoij et al., 1999; Bauckhage, 1996; Vial et al., 2001; Deen & Hjertager, 2002; Reese et al., 1996; Lee et al., 1999; Kulkarni et al., 2004; Laakonen et al., 2005; Brenn et al., 2002; Mudde et al., 1998; Montante et al., 2007; Nassar et al., 2004; Schafer et al., 2000; Sudiyo et al., 2007; Simmonet et al., 2007; Roizard et al. 1999; and Ellingsen & Risso, 2001). However, the laser beam used in the technique must have a clear path to penetrate the reactor as is shown in Schafer et al.'s (2000) PDA setup shown below in Figure 2.2.
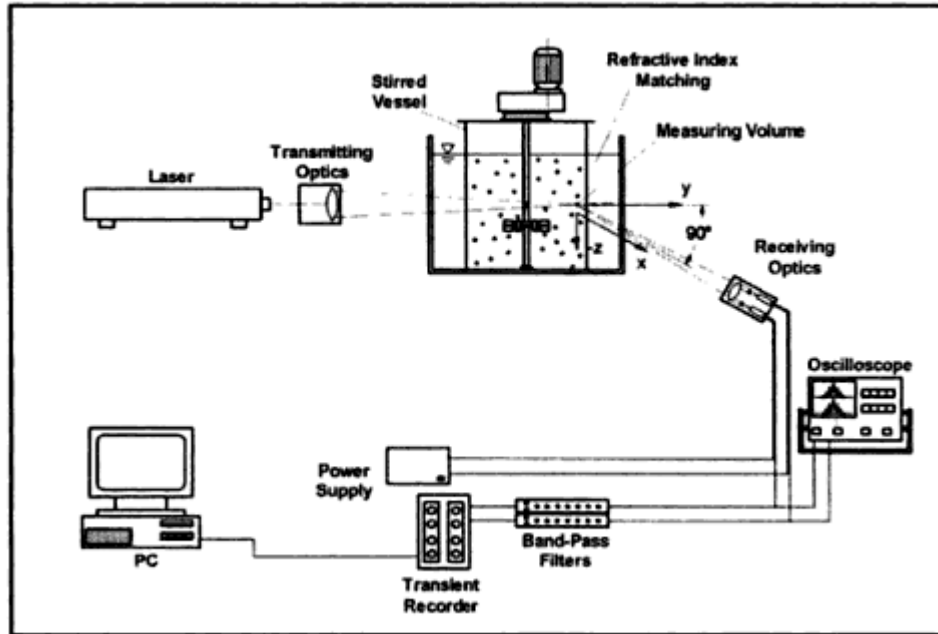
Figure 2.2: A common PDA experimental setup (Source: Schafer et al., 2000)

Thus, these laser techniques are usually used in transparent vessels and fluids at conditions of low holdups of the dispersed phase (to be able to see anything beyond the reactor wall), often involve complicated optics, can be very expensive, and are not suited for industrial reactors or a wide range of operating conditions.

Vizualization/high-speed photography techniques encounter the same limitations as the laser techniques in that a transparent vessel (or windows on the reactor) is required. In order to see anything beyond the wall the reactor must be run at low holdup conditions (Reith & Beek, 1968; Jiang et al., 1995; Luo et al., 1999; Yang et al., 2000; Miyahara et al., 1986; Hu et al., 2005; Hu et al., 2006; Hu et al. 2007; Kazenin et al., 2008; Martin et al., 2008; and Taboada et al., 2006). However, cost of high-speed photographic

equipment has decreased significantly in the past years, and images on the micron scale can be readily captured.

Tomographic techniques such as X-ray, γ-ray, electrical capacitance (ECT), electrical resistance (ERT), electrical impedance (EIT), ultrasonic, and nuclear magnetic resonance (NMR) are beautifully developed tools for capturing cross sectional information (and in some instances 3-D information) in opaque reactors. There are specific intricacies with each type of tomography: X-ray tomography (Heindel, 2000; Hubers et al., 2005; Schmitz & Mewes, 2000; Kumar et al., 1995; Toye, 1996; and Ford et al., 2008) can have a very high spatial resolution (600 μm^2 in Ford et al., 2008) with good temporal resolution, but is limited to low attenuating materials or small diameter reactors due to the low energy level of X-rays.

(i) CT measurement   (ii) Predicted
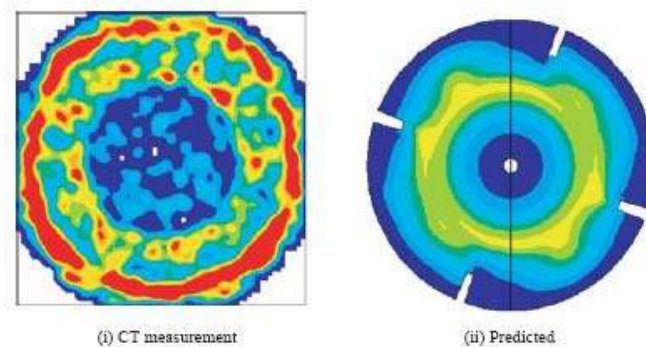
Figure 2.3: γ-ray CT scan of a G-L ST compared to a model (Source: Khopkar et al., 2005)

γ-rays have higher energy and are therefore more penetrative than X-rays but have a lower spatial resolution (1 mm^2), require long scan times, and thus give only time averaged properties (shown above in Figure 2.3), and cannot give phase dynamics (Veera & Joshi, 2000; Khopkar et al., 2005; Kumar et al., 1995; Jin et al., 2005; and

11

Froystein, 1997). ECT, ERT and EIT are much cheaper tomographic options and do not have the safety/regulatory issues associated with X-ray or γ-ray tomography. However, electrical tomography still has the complicated reconstructions associated with any tomography technique, requires fluids with dielectric properties, and often has good temporal resolution but poor spatial resolution (Mann et al., 1997; Warsito & Fan, 2005; Reinecke & Mewes, 1997; Bolton & Primrose, 2006; Schmitz & Mewes, 2000; and Kim et al., 2005). The ultrasonic tomography technique outlined by Warsito et al. (1999) and Utomo et al. (2001) can only be used in gas or solid holdups of up to 20% due to the significant attenuation cause by the large number of the dispersed phase. NMR/MRI methods can have both excellent spatial and temporal resolution (and one can be decreased to improve the other) but are still very expensive and have certain physical restraints (Chaouki et al., 1997; Gladden, 2003; and Lim et al., 2004). Thus, tomography can handle a wide array of fluids and vessel types but usually requires a very large capital investment and imposes a number of constraints.

Physical tracers can be used to gain information on the mean holdup of a phase, the characteristic mixing of a phase, or phase trajectories. Liquid tracers are usually salts detected by conducimetry, seeded radioactive isotopes, or colored dyes (Blet et al., 1999; Larachi et al., 1991; Garcia-Ochoa et al., 1997; Gupta et al., 2000; Manikowski, 1993; and Vrabel et al., 2000). Gas tracers are more difficult to use but have been employed by Joseph & Shah (1986). Solid tracers can be colored (Fortin, 1984), magnetic (Euzen & Fortin, 1987), fluorescent (Flaschel et al., 1987) or radioisotopes (Hoffmann et al.,

12

2005). There are two widely used types of particle tracking: radioactive particle tracking (RPT) and positron emission particle tracking (PEPT). In RPT (Dudkovic et al., 1991; Chen et al., 1999; Cassanello et al., 1995; Larachi et al., 1995; and Chauoki et al., 1997; Rammohan et al., 2001; and Nedeltchev et al., 2003), a radioactive particle that emits γ-rays is seeded inside a neutrally buoyant sphere for liquid measurements (or inside a pellet mimicking the properties of the solid for solid measurements), and the particle trajectories are tracked by multiple detectors that are arranged around the reactor. However, there is a very tedious and complicated calibration that must be followed in the process. PEPT tracks particle trajectories like RPT, but, with PEPT, a compound is radioactively labeled (commonly with a fluorine isotope). As the isotope decays two, back-to-back, high energy γ-photons are ultimately emitted. Sensors placed around the reactor can then triangulate the back-to-back emission to determine the position of the particle. PEPT is largely used in the medical field and has only been used to study process equipment over the past decade or so (Abellon et al., 1997; Sneiders et al., 1999; Stein et al., 2000; and Hoffmann et al., 2005); thus, most of the software is geared toward medical applications. Shown below in Figure 2.4, PEPT can give particle location within 1 mm every 2 ms at velocities up to 1 m/s. While PEPT accurately describes the majority of the flow in a ST, Fangary et al. (2000) found that it underestimated liquid velocities in the impeller region up to 100%.

13
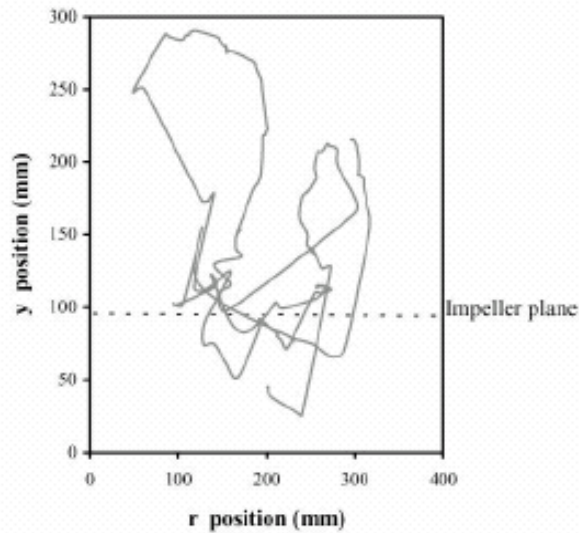
Figure 2.4: PEPT trajectory of a tracer in a ST (Source: Fangary et al., 2000)

RPT and PEPT are very elegant measurement techniques for opaque multiphase flows but are still very expensive and have stringent safety and regulatory constraints.

Pressure drop measurements (Joshi et al., 1990; and Vial et al., 2000) and dynamic gas disengagement (Camarasa et al., 1999; and Lee et al., 1999) can be used to identify overall phase holdups and can give insights into flow transitions, but do not provide the local measurements needed for the proper description of a multiphase reactor.

2.1.2 Invasive Techniques

If the flow in an opaque reactor needs to be described, invasive probes are usually employed because they can readily capture local phase dynamics across a wide range of operating conditions and are relatively inexpensive when compared to most of the non-invasive techniques. However, the drawback of an invasive probe is that it must be inserted into the reactor to interact with the flow itself and can therefore distort the

14

flow – commonly referred to as the observer effect. The challenge of using an invasive probe is to understand how the probe interacts with its environment at the scales of interest (to characterize any flow distortion effects caused by the probe) and to minimize any distorting effects it imposes on the flow.

Hot-film anemometry/heat transfer probes rely on the dependency of convective heat transfer on the local Reynolds number of the flowing liquid (King, 1914). The amount of heat removed from the probe can then be used to quantify the liquid phase velocity as well as the gas holdup (Wang & Ching, 2001; Utiger et al., 1999; Hogsett & Ishii, 1997; Menzel et al., 1990; Lu & Ju, 1987). There is no limitation on holdup measurements as will be seen shortly with the ultrasonic probes. Since the heat transfer probe assumes a uniform temperature distribution in the measured volume, it cannot be used to capture liquid velocities in systems where temperature fluctuations occur regularly. The calibration of the probe must also be checked routinely in order to obtain accurate results. The sensors themselves can be made very small (shown below in Figure 2.5) but are quite fragile and can be damaged in systems with high solids loadings.
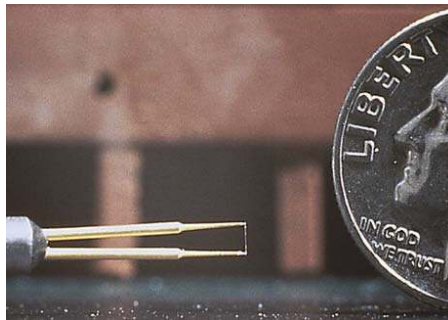
Figure 2.5: Heat transfer probe size (Source: American Association for Wind Engineering)

Impedance probes (shown below in Figure 2.6) act as electrodes and rely on the difference in conductivity between the liquid and the gas can be used to accurately obtain gas holdup and bubble dynamics (Hills & Darton, 1976; Matsuura & Fan, 1984; Tang & Fan 1989; Liu, 1993; Chen et al., 1998; Frohlich et al., 1991; Sun et al., 2006; Paglianti et al., 2001; Munholand & Soucy, 2005; and Bouaifi et al., 2001).
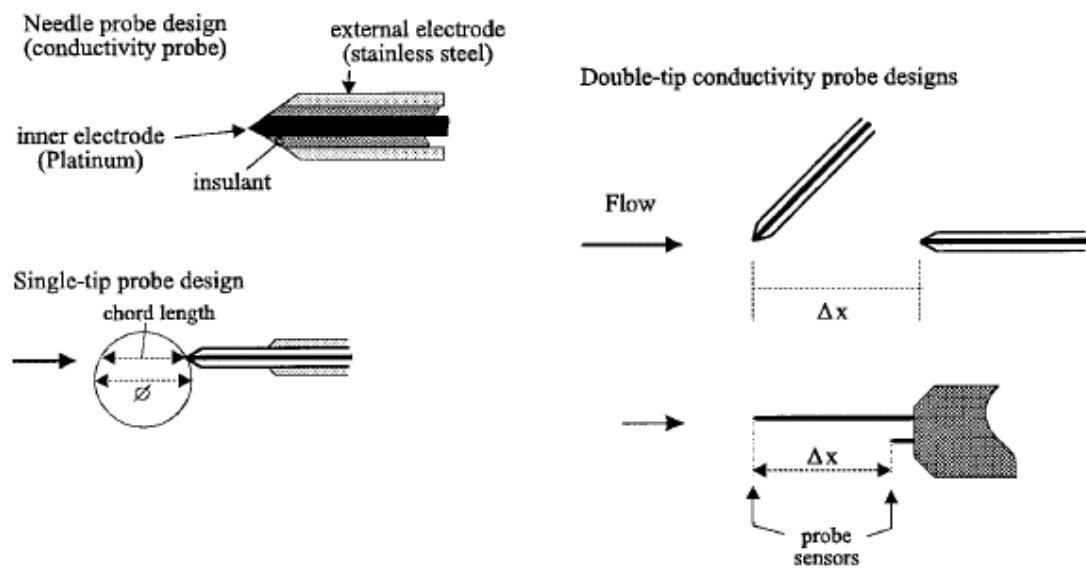
Figure 2.6: Impedance probe designs (Source: Chanson, 2002)

In order to achieve a good difference in signal between the liquid and the gas, the liquid must be conductive. Otherwise, salts must be added to improve the conductivity of the liquid. As with the heat transfer probes, the calibration of impedance probes can become very tedious. Impedance probes are extremely sensitive to changes in flow patterns; thus, different calibrations are necessary if the flow pattern in the reactor varies. The sensors of the impedance probe can be as small as 50 μm so that they interact with smaller bubbles.

Ultrasound probes have been developed because of their fast response times and ability to be used in opaque, viscous or high-pressure/high-temperature applications. The generated acoustic wave from the probe is reflected or scattered when it hits a boundary between two fluids or materials of different acoustic properties. The resultant wave is then analyzed to determine particle size, bubble dynamics and phase holdups (Stolojanu & Prakash, 1997; and Al-Masry, 2005). However, ultrasound probes do not work well in high holdup applications due to the significant acoustic attenuation caused by the reflection of gas bubbles (Broering et al., 1991). Stravs et al. (1987) also found that while ultrasound probes accurately measured spherical bubbles, ellipsoidal bubble measurements could have errors as high as 20%.

Direct sampling techniques use a suction tube inserted into the reactor to draw out samples for analysis (Barigou & Greaves, 1992, Wang et al., 2006b; and Garcia-Salas et al., 2007). This method allows for the determination of phase holdups and bubble size distributions. The capillaries are able to capture bubbles sizes down to 300 μm (Alves et al., 2002) all the way up to 8 mm. However, none of the applications presented in the literature use this method at industrial conditions.

With the development of oxygen sensors, mass transfer probes have developed into a good intrusive method for determining the local specific area in a reactor (Martin et al., 2008; Linek et al., 2004; Lau et al., 2006; Han & Al-Dahhan, 2007; Cents et al., 2005; Lin & Luo, 1997; and Bouaifi et al., 2001). There are many variations of mass transfer

probes; however, the large drawback is often the slow response time (up to a minute in liquids) because the probe response is dependant upon the diffusion of oxygen. Also, the mass transfer probes based on fluorescence are affected by ambient light as well as temperature changes.

Endoscopy/borescopy coupled with high-speed photography (shown below in Figure 2.7) has been used selectively to study multiphase flows (Peters et al., 1983; Angst & Kraume, 2006a; and Angst & Kraume, 2006b). This technique allows for the in-situ visualization of multiphase flow and thus can be used in opaque reactors. While the image processing software is well developed for determining phase distributions, the software for determining bubble dynamics is not well developed, and thus very tedious image analysis is required to extract further information in multiphase flows. The imaging itself, especially using the appropriate lighting to obtain good images, is also a nontrivial task. Borescope lengths can also limit how far one can peer into a reactor and they cannot be used at very high pressures or temperatures.
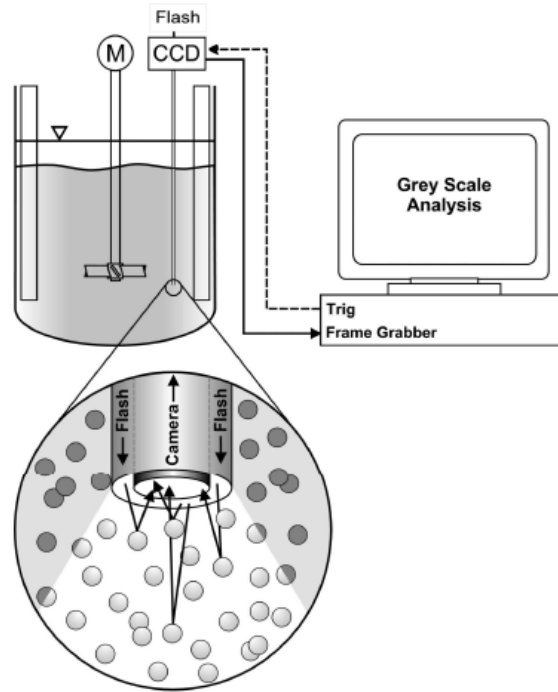
Figure 2.7: Angst & Kraume's (2006a) in-situ imaging system

Optical probe densitometers have become widely used since the price of fiber-optic cable decreased in the 1980's and rely on the difference of refractive indices between two fluids (Lee & DeLasa, 1987; Frijlink, 1987; Chabot & DeLasa, 1993; Chabot et al., 1998; Groen et al., 1995; Wang et al., 2006a; Hu et al., 2007; Schweitzer et al., 2001; Julia et al., 2005; and Barrau et al., 1999). As long as there is a distinguishable difference in the refractive indices of the gas and liquid phases (the refractive index of a fluid is related to its density), light refracts from the probe tip in the presence of liquid and reflects in the presence of gas. Thus, optical probes can accurately measure gas holdup and bubble dynamics (velocity, chord lengths, and interfacial area) in a wide array of fluids at high sampling rates (40 kHz - Xue et al., 2003). Optical probes can also be used in high-pressure (Mueller et al., 2007) and high-temperature systems. Probe sizes

can be as small as 50 μm and typically have very good signal to noise ratios. The drawback of using optical probes is that the bare fiber tips must be fully exposed to the flow, and thus the tips of optical probes are very fragile and must be handled with care – see Figure 2.8 below.
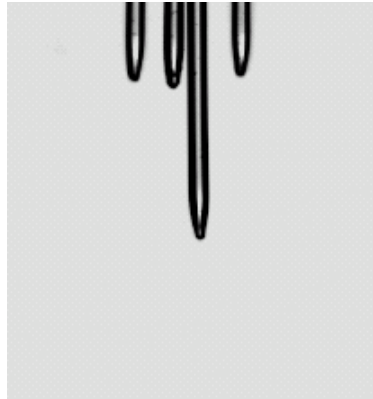
Figure 2.8: A 4-point optical probe composed of 200 μm fibers (Source: Xue et al., 2003)

Reflectance/transmission probes (Farag et al., 1997; Yang & Wang, 1993) are more hardy optical probes that also have the ability to measure solid holdups, but cannot readily capture the same bubble dynamics that the densitometry optical probes can and are usually much larger than a densitometry probe.

2.2 Basis of Optical Probe Selection for Investigation of G-L STs

Before a measurement technique is to be selected to investigate a particular multiphase reactor, it is important to have a qualitative picture of the flow that occurs within the reactor. Then, the best technique can be implemented to gain quantitative flow descriptions.

2.2.1 G-L ST Flows

When it comes to G-L STs (and any multiphase reactor for that matter) the most important parameter is the generation of high contact area between the gas and liquid phases – which in turn allows for high mass transfer and improved reaction rates. G-L STs achieve high specific areas (100-500 m^2/m^3 – Middleton, 1985) by using an impeller to disperse the gas in the liquid in a radial direction (Rushton turbine, concave blade impeller, etc.) or axial direction (marine impeller, pitched blade impeller, etc.) as depicted in Figure 2.9 below.
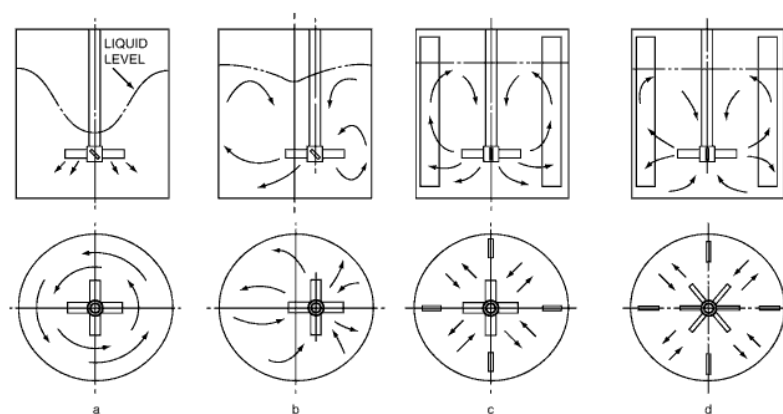
Figure 2.9: Flow patterns in a) unbaffled, b) offcenter, c) baffled axial and d) baffled radial STs (Source: Couper et al., 2004)

The reactor under investigation in this work is a fully baffled ST equipped with a standard Rushton turbine, which is commonly studied in the literature and used in industry although other impeller designs (hydrofoils, etc.) have been proven more efficient in dispersing the gas in the liquid. We have chosen this setup since it enables us to compare our data with other studies reported in the literature.

Once a reactor and impeller design is chosen, the next qualitative picture to obtain is the structure of the different flow regimes for that type of reactor. Nienow et al. (1977) provide that picture for a baffled ST equipped with a Rushton turbine shown below in Figure 2.10. As the impeller speed increases from zero at a constant gas flow rate, the dispersion in the reactor transitions from the flooded regime where the gas sparging dominates and creates a bubble column type flow with gas rising in the center, to the loaded regime where the impeller begins to have an effect, to the transition regime where the circulation loops characteristic of a stirred vessel just begin to form, to the completely dispersed regimes where the circulation loops are well developed and the impeller dominates the effects of the gas sparging.
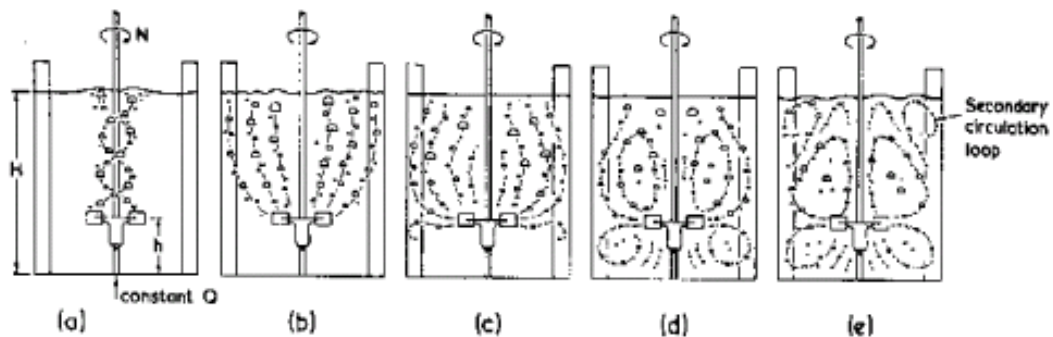
Figure 2.10: Flow regimes in a baffled ST with increasing Rushton turbine speed: a) flooded, b) loading, c) transition, d) complete dispersion and e) complete dispersion with secondary recirculation (Source: Nienow et al., 1977)

Shown in Figure 2.11 these flow regime transitions are commonly mapped out as a function of the flow number, Fl – the dimensionless ratio of the gas sparging rate to the fluid pumping action of the impeller:

$$Fl = \frac{Q_G}{N \cdot D^3} \qquad (1)$$

and the Froude number, *Fr* – the dimensionless ratio of the inertial forces to gravitational forces:

$$Fr = \frac{N^2 \cdot D}{g} \qquad (2)$$

where Q_G is the gas flow rate, N is the impeller rotational speed, D is the diameter of the turbine, and g is the gravitational constant.
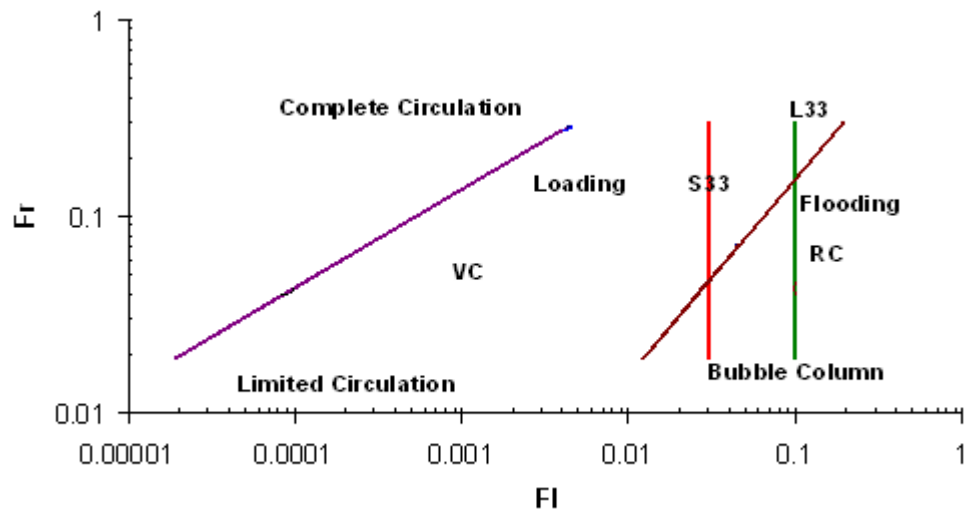
Figure 2.11: Map of ST flow regimes

Middleton & Smith (2004) state that in the homogeneous regime (where the impeller dominates) the bubbles have a monomodal size distribution and range from 0.5 to 4 mm in size. But, in the heterogeneous regime (higher superficial gas velocities) the distribution is bimodal and some large bubbles on the order of 10 mm.

In STs many studies have confirmed that bubble diameters can vary from the order of a hundred microns all the way up to the order of millimeters. Machon et al. (1997) also

found that bubble sizes decreased with height in the vessel. Schafer et al. (2000) compared a ST equipped with a Rushton turbine and a pitched blade impeller and found that the bubble diameters ranged from 0.65 to 1.5 mm in both instances. Contrary to what is usually assumed, they measured larger bubble diameters in the discharge stream than in other parts of the reactor. Shown below in Figure 2.12, Hu et al. (2006) and Laakonen et al. (2005a) confirmed the expected range of bubble sizes.
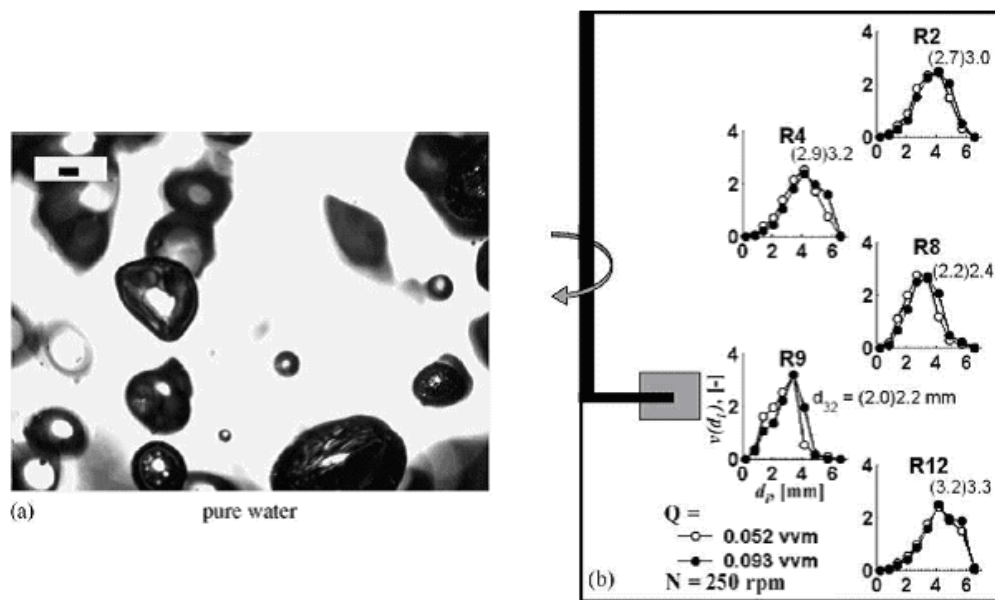
Figure 2.12: a) Air bubbles in water at the black scale of 200 μm (Source: Hu et al., 2006) & b) bubble size distributions in air/water (Source: Laakonen et al., 2005)

In a high-pressure bubble column Luo et al. (1999) observed the common effect that bubble sizes decrease and mean rise velocities decrease with pressure thus increasing gas holdup. These effects have yet to be reported in the literature for a ST but should be expected.

2.2.2 Basis for the Selection of Optical Probes

Thus, to investigate bubble dynamics in an opaque ST, such as a reactor used in industry, an inexpensive tool is needed that can capture gas holdup and bubble dynamics (chord lengths, velocity, and interfacial area) from the micron scale of spherical bubbles to the millimeter scale of ellipsoidal bubbles. Referring back to Figure 2.1, all the non-invasive techniques (except for possibly a very cleaver tracer technique) cannot capture bubble dynamics in an industrial reactor. Ultrasound probes would also be ineffective. Direct sampling cannot provide gas velocities, heat transfer probes have not been used well to measure bubble dynamics, mass transfer probes provide no bubble dynamics, and borescopy/endoscopy has limited application. Thus, the only invasive tools at one's disposal are impedance probes and optical probes.

Optical probes have four distinct advantages over impedance probes: 1) optical probes do not require a conductive liquid and thus can handle a wider array of fluids, 2) do not require routine calibration, 3) generally have a better signal-to-noise ratio, and 4) have been used at high-pressure conditions (Mueller et al., 2007) and can be used in high-temperature conditions (aluminum jacketed fibers can operate up to 400ºC). But, it should be noted that there still are limitations of the current technology for the use of optical probes in STs (also, optical probes give no information concerning the velocity of the liquid phase).

Chapter 3

Advancing Optical Probe Techniques into the Realm of Industrial STs

3.1   Current State of the Art of Optical Probes

Optical probe techniques have been used largely in bubble columns and pipe flows, but have scarcely been used in STs. Wang et al. (2006a) implemented a single-point optical probe with a reported diameter of 62.5 μm to measure the gas holdup distributions in a ST. A single-point probe is able to interact well with smaller bubbles expected in a ST, but it cannot be used to capture bubble velocity and therefore cannot capture bubble chord lengths or interfacial area. Bubble velocity, chord lengths, and interfacial areas have not been investigated in STs using optical probes.

In order to capture the velocity of a bubble a 2-tip probe has been most commonly used (Wu & Ishii, 1999; Choi & Lee, 1990; Chabot et al., 1992; and Fan et al., 1999). However, Lim & Argawal (1992) correctly point out that 2-point probes can give very large errors if the bubbles do not move in the direction that the probe is oriented. If curvature effects of the bubble are taken into account, the relative error of a 2-point probe velocity measurement is:

$$\text{Relative error (\%)} = (\tan\theta)^2 \cdot 100 \qquad\qquad (3)$$

where θ is the angle of incidence between the velocity vector of the rising bubble and

the axis of the probe shown below in Figure 3.1.
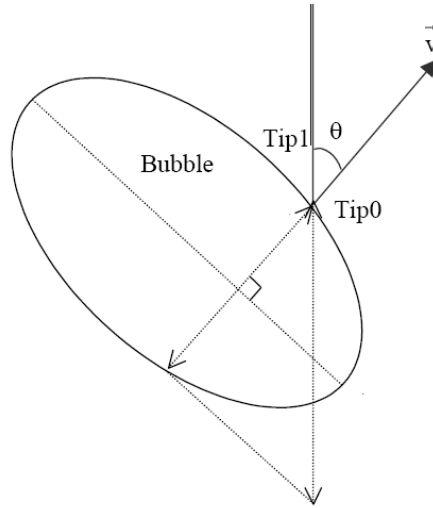
Figure 3.1: Two-point probe/bubble orientation

A quick inspection of the relative error shows that it is always positive and that as long

as θ is less than 12.5° the error is less than 5%. However, in most bubbly flows, this

cone of acceptance of ~25° is not acceptable since bubbles deviate from the axial

direction of the probe by a great extent. Thus, 2-point probes can only be used with

certainty where the probe is oriented parallel to a highly directional flow to obtain a

scalar velocity. To overcome this limitation, Frijlink (1987) developed the 4-point

optical probe, which essentially acts as three 2-point probes and screens for bubbles that

move only in the direction of the probe axis and that are pierced only near the center of

the bubble. While Frijlink's (1987) 4-point probe improves the accuracy of the

measured bubbles, the number of bubbles accepted for measurement is greatly reduced and velocity is still scalar.

Xue (2004) noted that 99% of the bubbles hitting a 4-point probe were rejected and that there were too many needless constrictions involved with the data processing algorithm, so the thrust of his work was to improve the algorithm to accurately measure bubble dynamics (including bubble velocity vectors, chord lengths, and interfacial area), increase the acceptance ratio of the probe, ease the constraints needed to manufacture the 4-point probe. The beauty of Xue's work (Xue, 2004, Xue et al., 2008a; and Xue et al., 2008b) was that it demonstrated that the 4-point probe does not need to be aligned with the flow to obtain accurate measurements.

3.1.1   Basis of 4-Point Optical Probes

Xue's optical probe design (Xue, 2004; Xue et al., 2008a; and Xue et al., 2008b) consists of 4 polymer-jacketed, fiber-optic cables with glass cores of 200 μm arranged in the geometrical configuration (similar to Frijlink, 1987) shown in Figure 3.2. The fibers are then glued into 1/8" stainless steel tubing for insertion into the reactor.
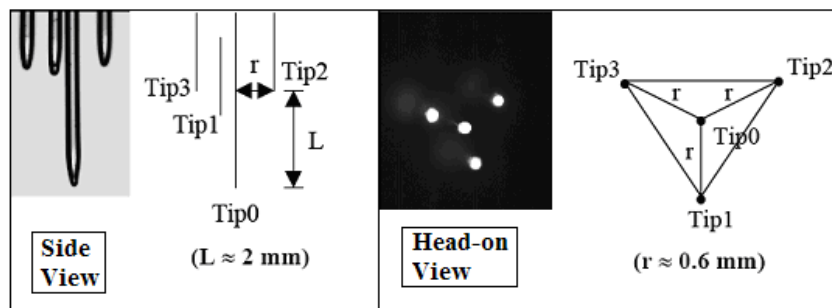
Figure 3.2: Probe dimensions of Xue (2004)

28

The dimensions of tips 1, 2, and 3 are all relative to tip 0. Looking at the dimensions, the cross sectional diameter of the probe is 1.4 mm (including the actual dimensions of the glass cores). A typical bubble strike hitting all four probe tips is shown below in Figure 3.3.
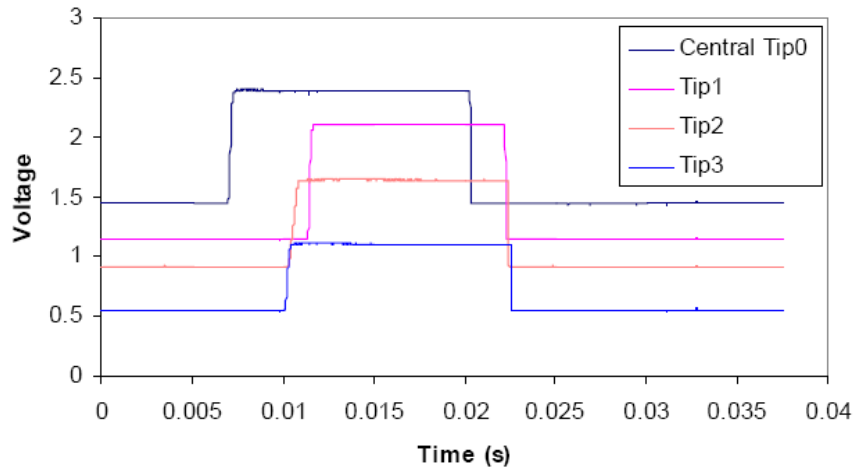
Figure 3.3. A bubble striking a 4-point probe (Source: Xue, 2004)

By analyzing these bubble interactions, the local bubble dynamics can be obtained.

The overall gas hold-up is defined as the ratio of the volume occupied by gas divided by the total volume of the G-L mixture:

$$\varepsilon_{G,overall} = \frac{V_G}{V_L + V_G} \qquad (4)$$

However, local gas holdup – the average holdup at a specific point in the reactor – is much more valuable for describing fluid motion within the reactor. Local gas holdup is defined as the fraction of volume occupied by gas within a certain volume of interest within the fluid mixture:

$$\varepsilon_{G,local} = \frac{V_{G,local}}{V_{L,local} + V_{G,local}} \qquad (5)$$

By invoking the ergodic hypothesis, which states that the ensemble average is equivalent to the time average, the spatially (volume) averaged local holdup can be replaced by its equivalent time-averaged local holdup:

$$\varepsilon_{G,local} = \frac{t_G}{t_G + t_L} \qquad (6)$$

Here the time-averaged local gas hold-up is defined as the ratio of time spent in the gas phase divided by the overall measurement time for a particular point of space within a vessel. By placing a single-tip optical probe in a specific point in a G-L system, the local hold-up is readily obtained by counting the total time spent in the gas phase (hundreds of bubble strikes) and comparing that time to the total measurement time (provided that the total measurement time is sufficiently long to provide a good statistical representation for the sampled point). The overall hold-up can then be deduced from the radial and axial local hold-up profiles.

For the determination of bubble velocity and chord lengths, imagine a bubble striking the probe as is shown in Figure 3.4.
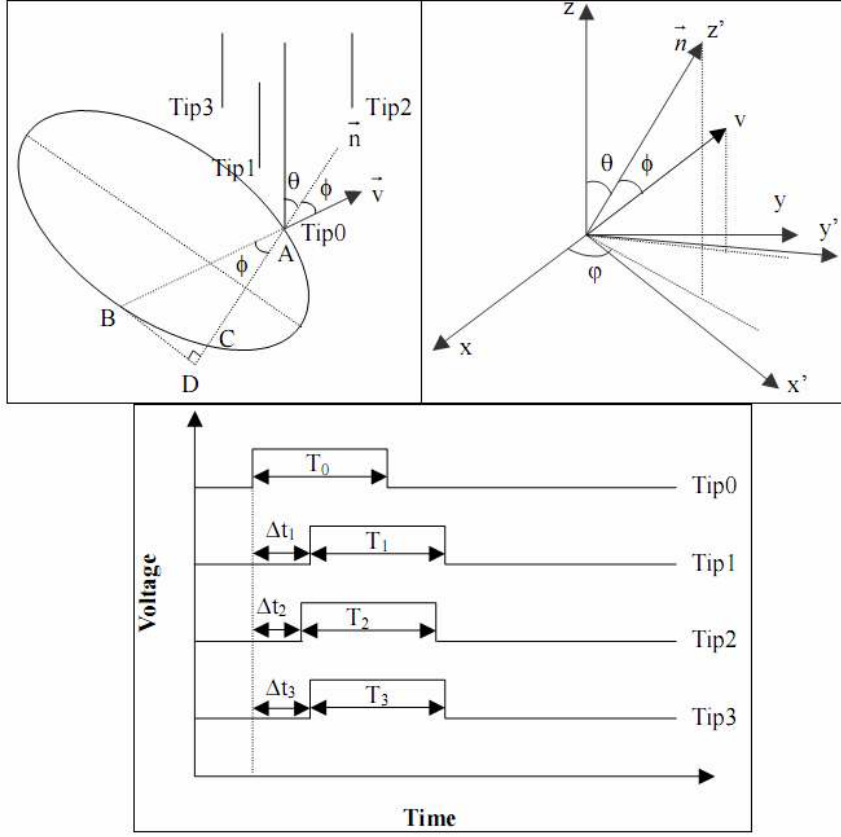
Figure 3.4: A Bubble-Probe Interaction (Source: Xue, 2004)

Here, $\vec{n}$ is the normal vector of the bubble, $\vec{v}$ is the velocity vector of the bubble, ϕ is

the deviation of $\vec{v}$ from $\vec{n}$ (usually very small), and φ and θ are the angles of approach

of the bubble. After the appropriate coordinate transformation, the time intervals

between the instant when a bubble hits the central tip, Tip 0, and when it hits Tips 1, 2,

and 3 are:

$$\Delta t_1 - \frac{T_0 - T_1}{2} = \frac{x_1 \cdot \sin(\theta)\cos(\varphi) + y_1 \cdot \sin(\theta)\sin(\varphi) + z_1 \cdot \cos(\theta)}{v \cdot \cos(\phi)}$$

$$\Delta t_2 - \frac{T_0 - T_2}{2} = \frac{x_2 \cdot \sin(\theta)\cos(\varphi) + y_2 \cdot \sin(\theta)\sin(\varphi) + z_2 \cdot \cos(\theta)}{v \cdot \cos(\phi)} \qquad (7)$$

$$\Delta t_3 - \frac{T_0 - T_3}{2} = \frac{x_3 \cdot \sin(\theta)\cos(\varphi) + y_3 \cdot \sin(\theta)\sin(\varphi) + z_3 \cdot \cos(\theta)}{v \cdot \cos(\phi)}$$

31

The 3 unknowns in the above equations are θ, φ, and $v \cdot \cos(\phi)$. The three equations are non-linear but can be solved numerically. Thus, assuming that the deviation of the bubble's velocity vector from the normal is small (and therefore $\cos(\phi)$ is approximately one), the velocity vector can be determined when a bubble interacts with the 4 probe tips. Once the velocity is known, the bubble chord length pierced by tip i is simply:

$$L_i = v \cdot \cos(\phi) \cdot T_i \qquad (8)$$

With the interaction of multiple bubbles with the probe, a chord length distribution is obtained. Bubble size can then be determined if a bubble geometry (spherical, ellipsoidal, etc) is assumed. Millimeter bubbles (about 1.5 mm and larger) in ST would be expected to be ellipsoidal and all the smaller bubbles spherical. However, bubbles in turbulent flows often fluctuate from a specific geometry (Bhaga & Weber, 1981). Thus, while a Sauter mean diameter can be calculated for an ellipsoidal bubble, it does not physically describe the actual bubble. An accurate method to determine bubble size from chord length distributions does not exist unless a specific geometry is assumed.

Kataoka et al. (1986) derived the equation for specific interfacial area:

$$a = \frac{1}{\Delta T} \cdot \sum_N \frac{1}{v \cdot \cos(\phi)} \qquad (9)$$

Here N is the total number of the gas-liquid interfaces passing by the probe during the measurement time ΔT, and ϕ is the angle between the velocity vector and the normal vector of the bubble's surface (Figure 3.5).
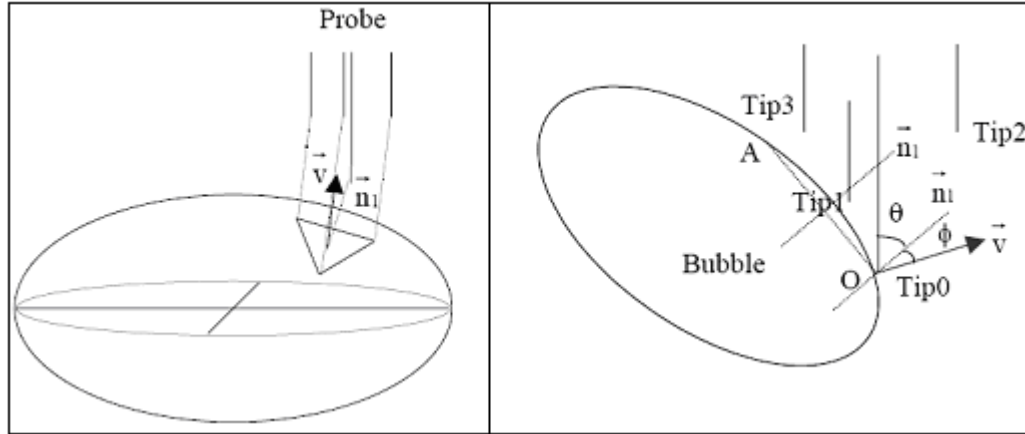
Figure 3.5. Measurement of interfacial area (Source: Xue, 2004)

The equations describing the velocity of the bubble's surface section pierced by the probe are:

$$\Delta t_1 = \frac{x_1 \cdot \sin(\theta)\cos(\varphi) + y_1 \cdot \sin(\theta)\sin(\varphi) + z_1 \cdot \cos(\theta)}{v \cdot \cos(\phi)}$$

$$\Delta t_2 = \frac{x_2 \cdot \sin(\theta)\cos(\varphi) + y_2 \cdot \sin(\theta)\sin(\varphi) + z_2 \cdot \cos(\theta)}{v \cdot \cos(\phi)} \qquad (10)$$

$$\Delta t_3 = \frac{x_3 \cdot \sin(\theta)\cos(\varphi) + y_3 \cdot \sin(\theta)\sin(\varphi) + z_3 \cdot \cos(\theta)}{v \cdot \cos(\phi)}$$

The unknowns are now θ, φ, and $v \cdot \cos(\phi)$, and the three equations can be solved to

find $v \cdot \cos(\phi)$ which can then be used in Kataoka's (1986) equation to directly

determine interfacial area without assuming bubble geometry.

3.2   Requirements for an Optical Probe in a ST

Xue (2004) investigated bubble columns where mean bubble sizes were much larger

than the diameter of the 4-point probe diameter of 1.4 mm. From the expected bubble

sizes in a ST, it is evident that this probe size will not be able to sample bubbles at least smaller than its own diameter although smaller bubbles should be expected in a ST, especially at higher pressures. Thus, if the 4-point probe size can be reduced, it would be able to sample the spectrum of smaller bubbles expected in a ST.

It is also necessary to keep the size of each of the individual probe tips as small and as sharp as possible so that they can pierce and interact with the smaller, spherical bubbles. However, even the smallest possible probe may not interact at all with the smallest of bubbles; this is where borescopy can be used in tandem with an optical probe to quantify the effect of a 4-point probe missing a portion of the bubble population.

One should note that the impeller discharge stream can impart a highly directional flow. Consider the radial discharge stream of bubbles from a Rushton impeller; in specific instances such as this example, it is possible to accurately employ a 2-point probe oriented in the tangential direction of the discharge stream. This would reduce the probe dimensions as compared to the 4-point probe and could be used to capture smaller bubbles in the discharge stream.

The final requirement of an optical probe in a ST is the ability to use the probe in high-pressure and high-temperature conditions. The probes used by Xue (2004) could withstand pressures of 10 barg but were used only at room temperatures. Using the same type of fiber as Xue (2004), Mueller et al. (2007) greatly increased the working

pressure of optical probes to 120 barg. But, the type of fiber used by both had a temperature limitation of 100ºC. By using a more rugged, aluminum jacketed fibers that can withstand temperatures up to 400ºC and that bind very well with the sealing epoxy, the working temperature of the optical probes can also be greatly increased.

Chapter 4

Bubble Dynamics in Stirred Tanks

A single point optical probe is developed for the determination of local gas holdup, and a 4-point fiber-optic probe is developed for the determination of local gas holdup, bubble velocity, bubble chord length and interfacial area distributions in stirred tanks (ST) for potential use in stirred tank reactors. Experiments with water sparged with air were conducted to demonstrate the usefulness of the fiber-optic probes in accurately in describing bubble dynamics. In the 20 cm ID plexiglass ST and the 1-liter autoclave that have been used, the single-point probes accurately captured the complex 3-D holdup profiles within the vessels. The 4-point mini-probe was found to accurately capture bubble dynamics of bubbles as small as ~ 0.85 mm. The developed optical probes can withstand elevated temperatures and pressures and thus can be used in opaque multiphase flows at industrially relevant conditions.

4.1 Introduction to Stirred Tanks (STs)

An introduction to STs is given in Chapter 2.2.1. The experimental studies, described below, were conducted and consisted of three specific experiments: 1) Determination of local gas holdup in a pressurized ST (up to 69 barg). 2) Investigation of local holdups in a standard ST at atmospheric conditions using the old fiber used by Xue (2004) and the

method employed by Wang et al. (2006). 3) An extensive 4-point mini-probe investigation of local bubble dynamics at atmospheric conditions.

4.2 Experimental

4.2.1 Materials

St. Louis city tap water and air were used for the experiments in the 20 cm ID ST. St. Louis city tap water and pressurized air (AirGas) were used in the 1-liter autoclave experiments.

4.2.2 Apparati

The experimental setup for the 20 cm ID plexiglass ST is shown below in Figure 4.1. The standard ST is fully baffled - each of the four baffles has a width of $D_T/10$. The ST is also equipped with a 6-bladed Rushton impeller $D_T/3$ in diameter.
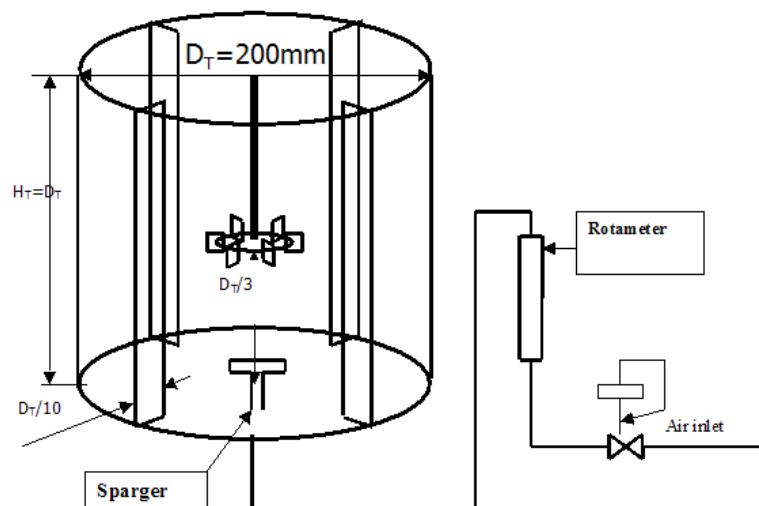
Figure 4.1: Experimental setup for 20 cm ID ST (Source: Rammohan, 2002)

The type of sparger used to introduce the air in the ST is shown in Figure 4.2.
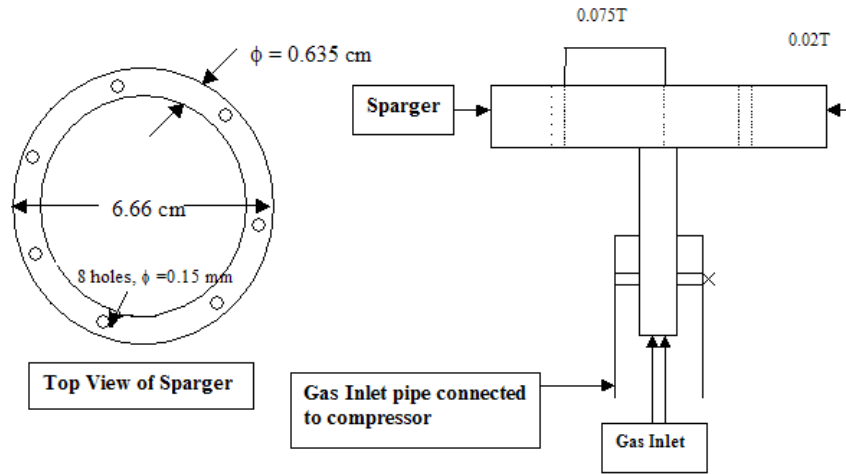
Figure 4.2: Sparger for the 20 cm ID ST (Source: Rammohan, 2002)

The above ST is used for all experiments except for the high-pressure experiments, in which the 1-liter autoclave (shown below in Figure 4.3) is used. All experiments were conducted at room temperature.
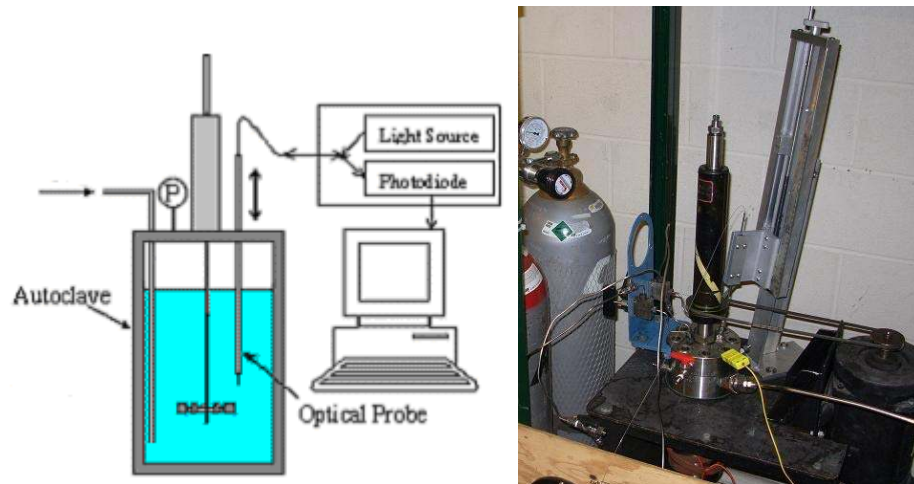
Figure 4.3: Experimental setup, fiber-optic probe and actuating arm for high-pressure studies

The 1-liter autoclave is 7.62 cm in diameter and 22.86 cm tall with a slightly concave bottom and is equipped with two baffles and a 3.175 cm diameter, standard 6-bladed

Rushton impeller with hollow shaft stirrer to induce air from the headspace into the liquid. A pressurized cylinder of air (AirGas) was used to introduce pressurized air into the autoclave. Pressure was controlled via a Tescom 4000 back-pressure regulator using Validyne pressure transducers for pressure measurements. All other experimental details (including the optical probe) are the same as described in Mueller et al. (2007).

Detailed descriptions of the optical probes, including manufacture and use, is provided in Appendix B.

4.3 Single-Point Probe and High-Pressure Holdup

Stegeman et al. (1995) investigated a standard ST with a 15.6 cm ID at pressures up to 66 barg and found that pressure does not influence the overall gas holdup, shown below in Figure 4.4.
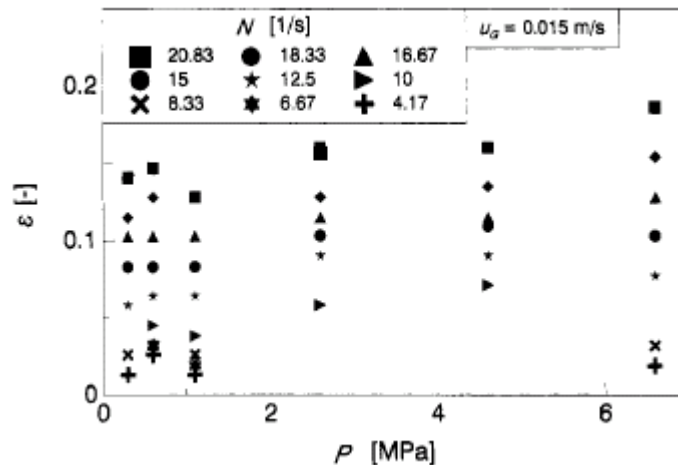
Figure 4.4: Effect of pressure on overall gas holdup (Source: Stegeman et al., 1995)

From Figure 4.4 it is clear that increasing the impeller rotational speed increases the overall gas holdup but that there is a negligible effect on the overall gas holdup as the pressure increases (although it appears there is a slight increase in overall holdup with pressure in some instances). However, the studies of Stegeman et al. (1995) suffered from a notable inaccuracy in their overall holdup measurements, which were obtained via the mounted view window on their stirred vessel. A 15% accuracy in estimating the overall holdup was estimated. Yet, the overall holdup is only a piece of the puzzle needed to describe the bubble dynamics in a G-L ST.

Our experimental runs were performed by placing 600 mL of water in the 1-liter autoclave (a total liquid height of $H = 12.25$ cm with the location of the midpoint of the impeller at $z/H = 0.35$). The autoclave was then sealed and runs were conducted at three different impeller speeds (2100, 2400 and 2700 rpm – higher impeller speeds are needed to ensure gas dispersion), three different locations ($z/H = 0.54$ & $r/R = 0.37$; $z/H = 0.78$ & $r/R = 0.45$; and $z/H = 0.94$ & $r/R = 0.47$), and four different pressures (0, 6.89, 27.58, 68.95 barg). Under these conditions the gas is completely dispersed in the reactor.

4.3.1 Results

The local holdup is needed to properly describe the phase distribution in a stirred vessel. Figures 4.5, 4.6, and 4.7 show the observed effect of pressure and impeller speed on the local gas holdup. Note that the mean relative error in local holdup is less than 5%
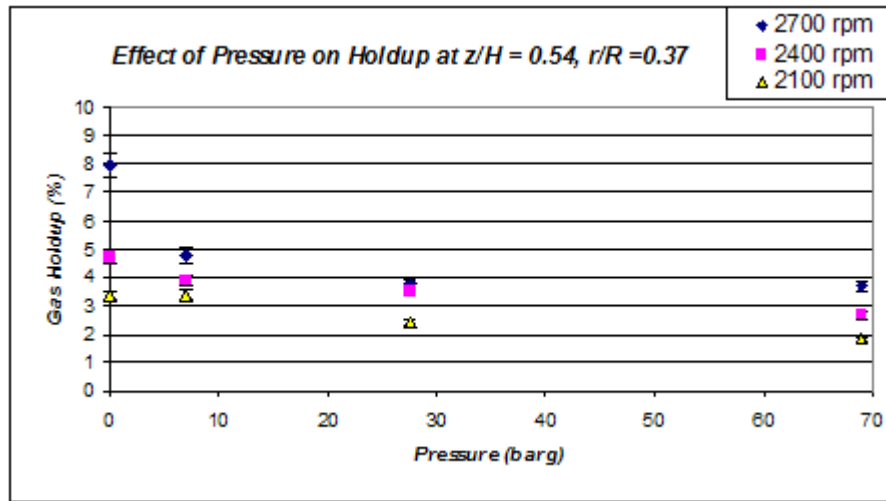
Figure 4.5: Local gas holdup as a function of pressure and rpm near the impeller
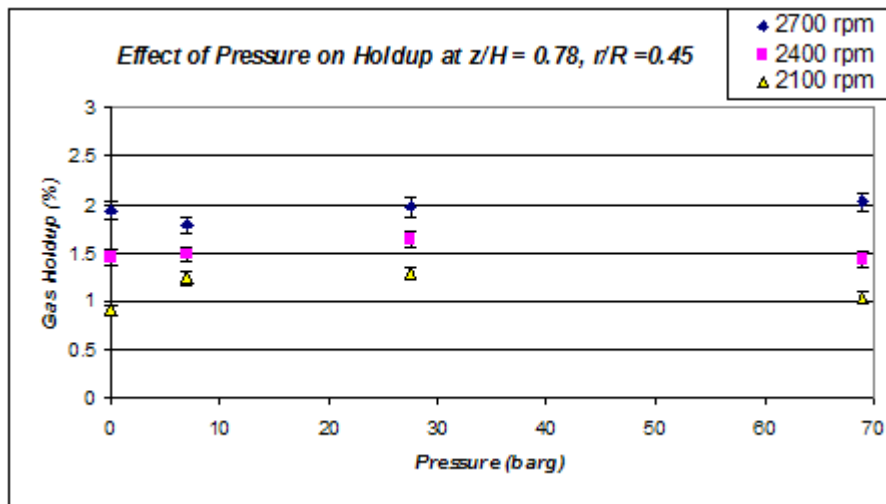
Figure 4.6: Effect of pressure and rpm on local gas holdup midway between the impeller and liquid surface
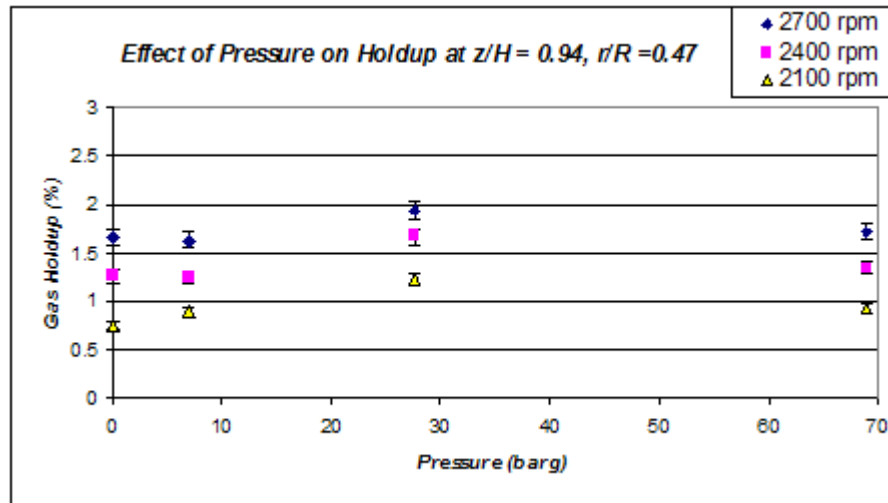
Figure 4.7: Effect of pressure and RPM on local gas holdup near the liquid surface

From the above figures, it is observed that increasing the impeller speed indeed increases the local gas holdup in each instance – as expected for a stirred vessel. However, it is also evident that the local gas holdup profiles do indeed change with pressure and can either decrease or even slightly increase depending on the local position within the reactor. Near the impeller discharge region (Figure 4.5), the local gas holdup decreases with increasing pressure. Changes in the local gas holdup farther above the discharge stream (Figures 4.6 and 4.7) are less drastic. Thus, while Stegemen et al. (1995) saw no apparent effect of pressure on overall gas holdup, the experiments conducted in this research indicate that pressure does indeed change the local holdup profiles throughout the reactor – indicating that increasing the pressure disperses the high holdup in the discharge stream more throughout the rest of the reactor, which can be attributed to the decreasing bubble size with pressure.

It is also qualitatively observed – since the radial position in this experiment varies slightly at each vertical position (due to the entrance angle of the probe in the reactor) – that in all instances (Figures 4.8, 4.9 and 4.10) the local gas holdup decreases as the height from the impeller discharge stream increases (to be expected in the dispersed flow regimes as reported by Bombac et al., 1997, Wang et al., 2006, Cents et al., 2005, and Ford et al., 2008).
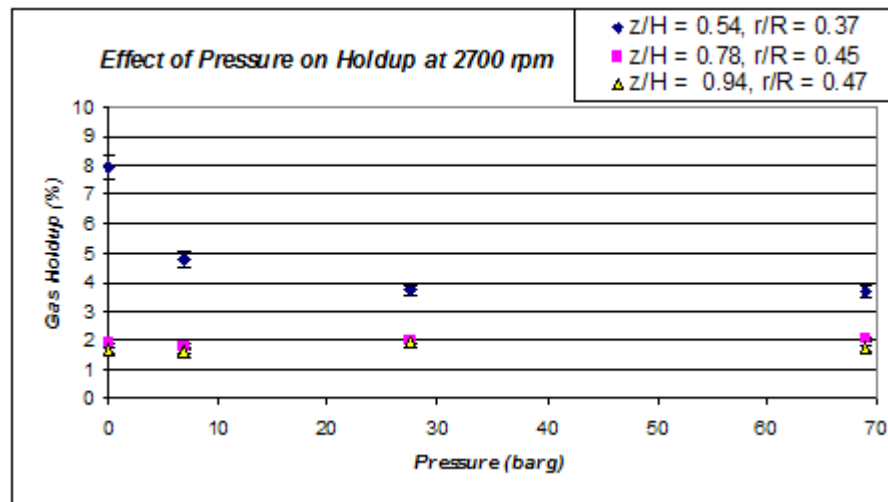
Figure 4.8: Effect of pressure and height on local gas holdup at 2700 rpm
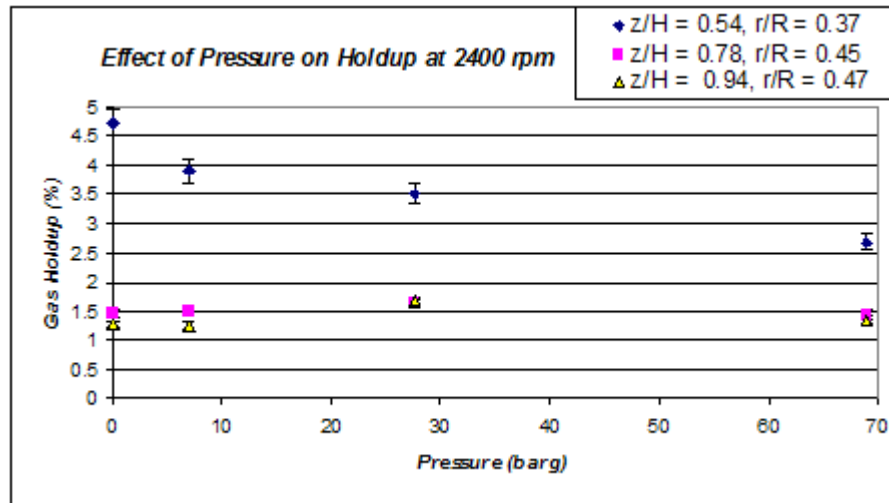
Figure 4.9: Effect of pressure and height on local gas holdup at 2400 rpm
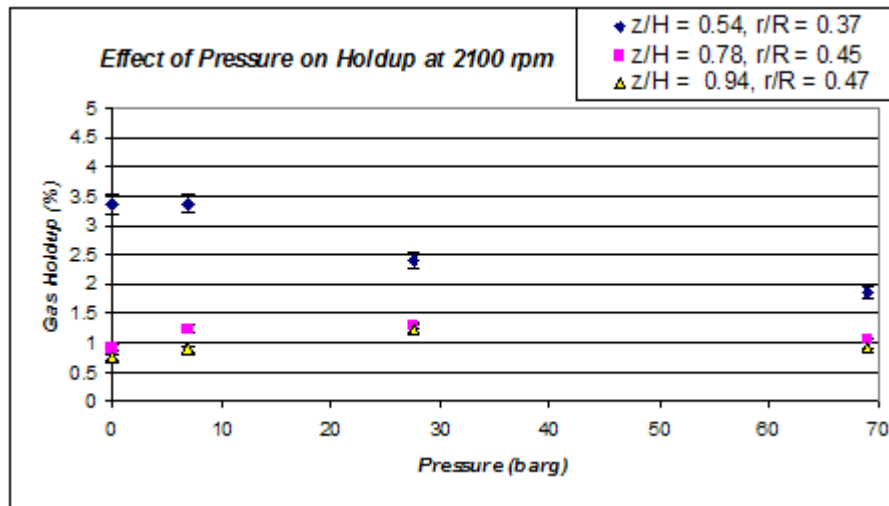
Figure 4.10: Effect of pressure and height on local gas holdup at 2100 rpm

4.4 Single-Point Probe and Holdup Experiments in the 20 cm ID ST at Atmospheric Pressure

Rammohan (2002) studied the same ST setup employed in this study using gamma ray

computed tomography (CT) to determine gas holdup cross-sectional distributions at a

number of elevations. Unfortunately, most of his experiments were conducted in the flooded flow regime (gas flow rates up to 7.5 L/min and rotational speeds up to 400 rpm). Shown below in Figure 4.11 are his results at the z/H = 0.5 cross-section.
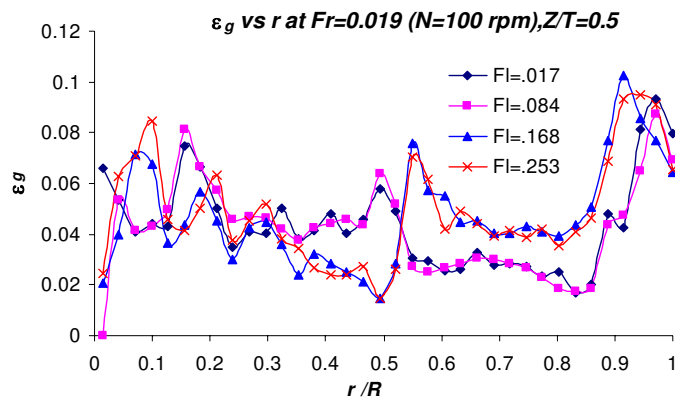
Figure 4.11: Radial gas holdup profiles in the flooded regime at z/H = 0.5 (Source: Rammohan, 2002)

It should be noted that the above figure is not consistent with other observations. In the flooded regime most of the bubbles rise up in the core of the stirred vessel, along the impeller shaft to the top of the free liquid surface with very little to no recirculation of bubbles along the walls. Thus, the highest holdups should be in the core of the stirred vessel and there should be a distinct drop in gas holdup in the radial direction outside the core. Ford et al. (2008) studied a 21 cm ID ST (very close to the 20 cm ID ST used in this and Rammohan's study – although Ford et al.'s ST had a dished bottom). It is worth noting that even in the impeller discharge stream, where the highest holdups should be expected (shown below in Figure 4.12), the radial gas holdup values are mostly below 10%.

45
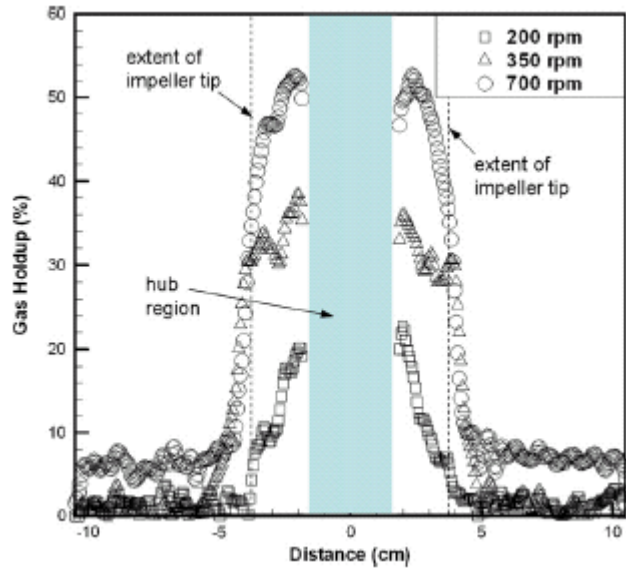
Figure 4.12: Radial gas holdup profiles in the impeller and discharge stream at 9 L/min (Source: Ford et al., 2008)

And, at the 200 rpm and a gas flow rate of 9 L/min, Ford et al.'s ST operates in the flooded regime, and holdups are near zero away from the impeller region. Lu & Ju (1987) also studied the impeller discharge stream in a 28.8 cm ID ST and noted the similar drop-off. At 600 rpm and a gas flow rate of 40.6 L/min (equivalent to 6.77 m^3/s shown below in Figure 4.13), the local gas holdup values outside the impeller discharge stream are much lower than 10%, even in this dispersed regime.
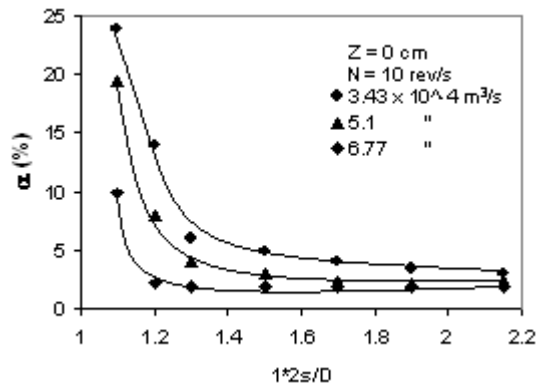
Figure 4.13: Radial holdup distribution outside the impeller sweep (Source: Lu & Ju, 1987)

46

Wang et al. (2006) also studied holdup values using a single-point optical probe in a 38 cm ID ST. They studied flow regimes at constant gas flow rate (13.3 L/min) and at various impeller speeds shown below in Figure 4.14.
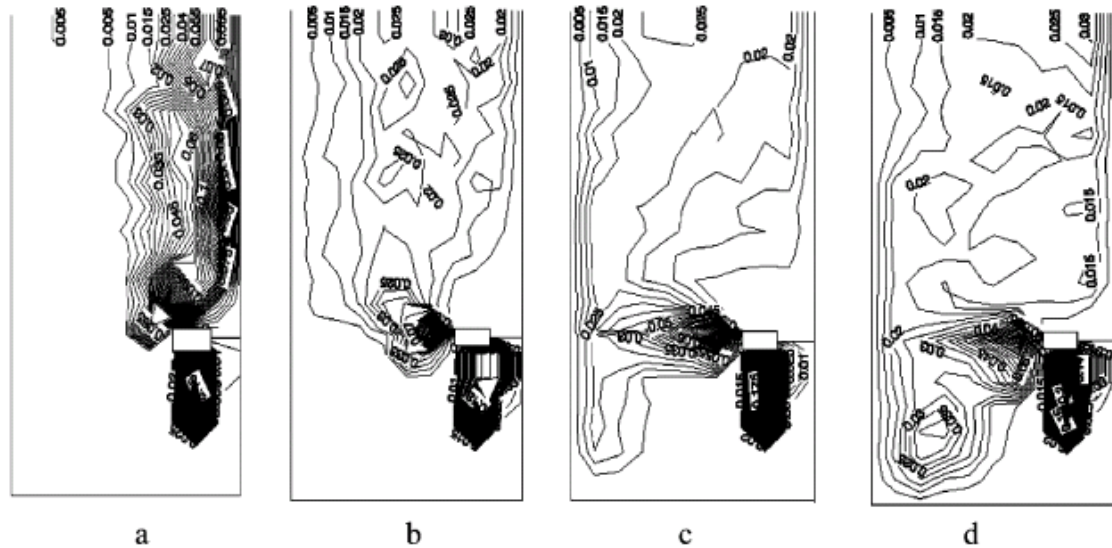
Figure 4.14: Holdup profiles a constant gas flow rate with increasing impeller speed a) 78 rpm, b) 134 rpm, c) 231, and d) 294 rpm (Source: Wang et al., 2006)

Again, in the flooded regime - a) in Figure 4.14 - it is evident that the holdup values drop significantly toward zero away from the core of bubbles.

Bombac et al. (1997) studied a 45 cm ID ST and studied the axial dependency of gas holdup, shown in Figure 4.15
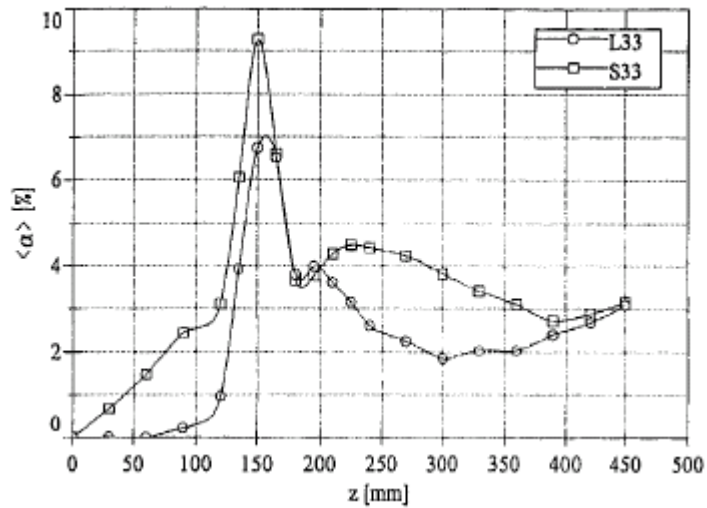
Figure 4.15: Radially integrated gas holdup values as a function of vessel height for different dispersed regimes (Bombac et al., 1997)

Cents et al. (2005) presented the following profiles (Figure 4.16) for the axial

dependency of gas holdup in a 40 cm ID ST.
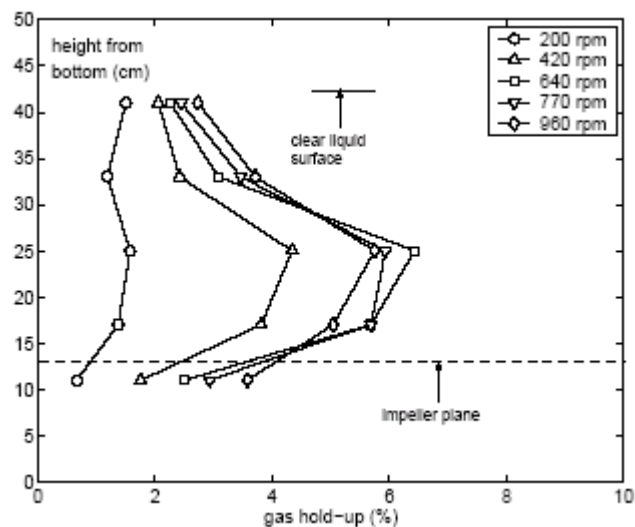
Figure 4.16: Gas holdup as a function of axial position at 43.7 L/min (Source Cents et al., 2005)

Ford et al. (2008) also provide a good picture of the transition from the flooded regime

(200 rpm, shown in Figure 4.17) to the rest of the dispersed regimes in their 21 cm ID

ST.
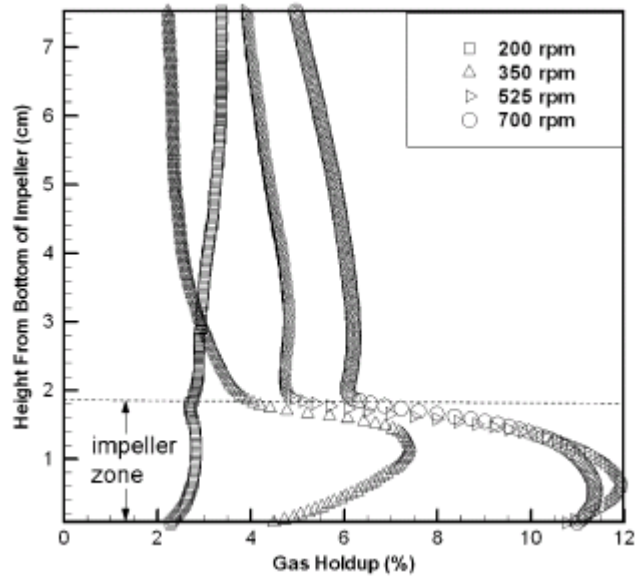
**Figure 4.17: Axial transitions in holdup from flooded to the dispersed regimes at 9 L/min
(Source: Ford et al., 2008)**

From Figures 4.15, 4.16, and 4.17 it is evident that the gas holdup decreases with height above the impeller except in the case of the flooded regime where there is a slight increase.

4.4.1   Results

We first compared the holdup results of the single-point optical probe with Rammohan's (2002) work since both experiments employ the same experimental setup. A single point probe (200 μm in diameter) was positioned in the tank pointed downward parallel to the impeller shaft and then was moved radially outward from the impeller shaft toward the wall of the reactor at constant height midway between to baffles. Local measurements were taken at each point for the span of 5 minutes (as opposed to 1.5 minutes employed by Wang et al., 2006) to ensure accurate time-

averaged results for gas holdup at each location. The results for the 20 cm ID ST for Fr = 0.019 and Fl = 0.253 are shown below in Figure 4.18.
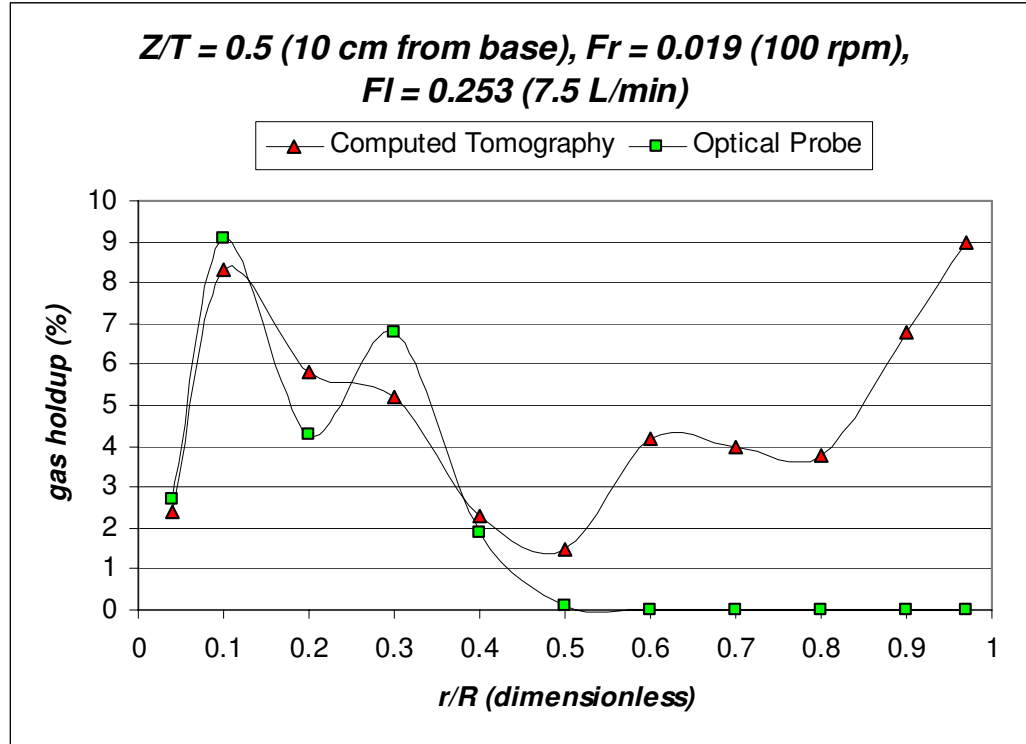
Figure 4.18: Differences between CT and optical probe results for gas holdup.

From inspection of the above figure, it is evident that the two measurement methods agree reasonably well with each other in the region $0 < r/R < 0.4$. However, for $r/R > 0.4$ the CT measurements indicate a region of high holdup near the wall, whereas the optical probe indicates holdups near zero. In this flooded regime, the air core of bubbles rise from the ring sparger, flow around the impeller and twist up along the impeller shaft (see Figure 4.19 below).
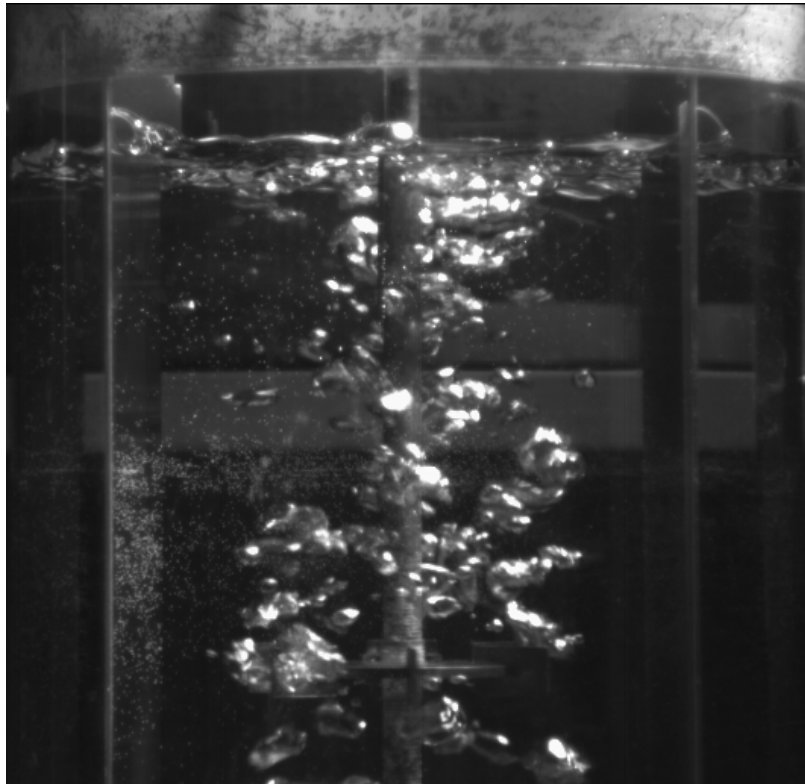
Figure 4.19: Typical flooding of the impeller

Thus, while a few bubbles (on the order of 10 – 100 microns, which would not be detected by the optical probe) are seen in the outer regions flowing with the liquid, it is not possible that these bubbles can account for the almost 10% gas holdup near the wall indicated at this flow regime by Rammohan. The optical probe and visual results shown in Figures 4.18 and 4.19 as well as the literature results in Chapter 4.4 indicate that the CT results of Rammohan (2002) in the region $0.4 < r/R < R$ are not trustworthy.

This above result was perplexing since Xue's (2004) results in bubble columns were found to agree quite well with CT results. Thus, another holdup comparison was made

with Liu et al.'s (2006) CT results for the same experimental setup (at 600 rpm and 18.9 L/min, or Fr = 0.680 and Fl = 0.106) shown below in Figure 4.20. But, again the CT and optical probe results do not show the same radial profiles. Since the CT values are averaged over the entire reactor and the optical probe measurements were taken at a single angular slice (45° - midway between the baffles), it is possible that there can be some discrepancies (how holdup varies with angle will be shown shortly). However, those discrepancies cannot account for the large minimum obtained by CT near the impeller shaft. That large minimum in the CT profile also rules out the possibility that the optical probe may be missing a large portion of the smaller bubble population since the probe yields higher holdup values in that region.
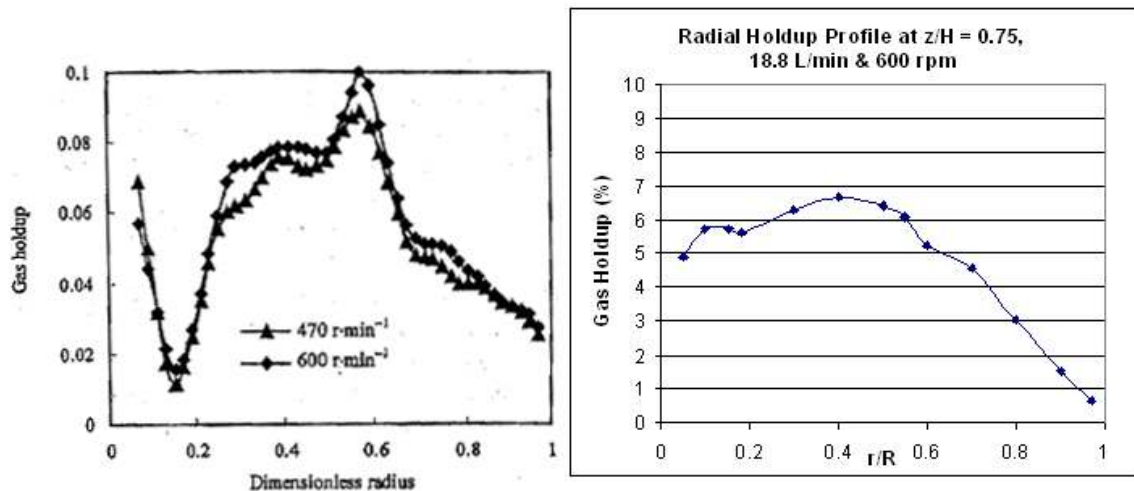
Figure 4.20: Radial gas holdup profiles at 18.8 L/min and z/H = 0.75
(Left: Liu et al., 2006 & Right: the single-point optical probe)

Visual inspection in the z/H = 0.75 plane at the above operating conditions shows that most bubbles rise vertically through that plane and that the highest number of bubbles (and thus holdup) should be somewhere near r/R = 0.5 (bubbles from the impeller

discharge stream curl back from the wall as they rise). Gas holdup contour maps in similar operating regimes provided by Wang et al. (2006) and Bombac et al. (1997) show no indication of the large minimum seen the in CT results of Liu et al. (2006). Thus, there are significant differences between the CT and optical probe results conducted in the same experimental setup at the same conditions, yet high-speed photography confirms the optical probe results.

Note that the previous examples in this chapter only show radial or axial dependency on gas holdup. Thus, simple holdup experiments were conducted using Wang et al.'s (2006) method at a flooded regime (150 rpm and 5 L/min, or Fr = 0.043 and Fl = 0.113) and at a completely dispersed regime (700 rpm and 9.4 L/min, or Fr = 0.926 and Fl = 0.045) to see what the radial, axial, and tangential dependency of the gas holdup was in the two regimes (shown in Figure 4.21).
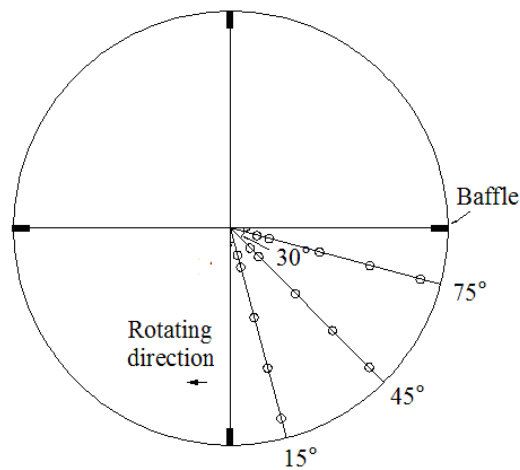
Figure 4.21: Radial and tangential measurement locations for z/H = 0.75, 0.5, and 0.25 for the single-point probe experiments

53

The radial holdup profile at z/H = 0.5 is shown below in Figure 4.22 for the flooded flow regime. Note that the gas holdup drops off significantly between 0.2 < r/R < 0.4 – a similar phenomenon as shown in Figures 4.14 and 4.18 for the flooded regime.
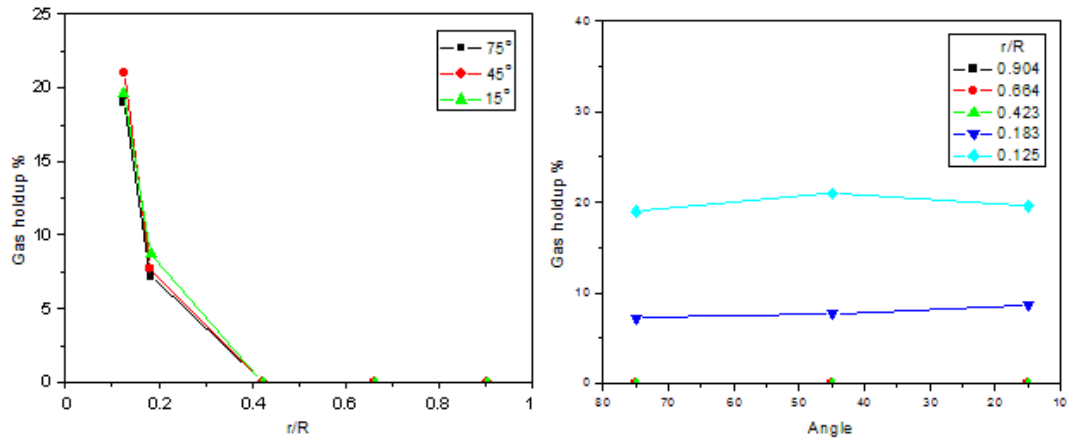
Figure 4.22: Radial and tangential holdup profiles at z/H = 0.5 for the flooded flow regime

In the flooded regime, the gas flow dominates the effect of the impeller, thus it is expected that the tangential holdup should not vary much in the flooded regime. The results in Figure 4.22 confirm that there is little difference in gas holdup with angle and that the gas holdup near the wall is negligible compared to that in the bubble core near the impeller shaft.

In the completely dispersed regime, the gas holdup is observed to vary much more with tangential location. Figure 4.23 confirms observations that the leeward baffle (near the 75° data points) and windward baffle (near the 15° data points) do indeed influence the tangential holdup profiles. This is rarely, if at all, discussed in the literature as most data is displayed in axially or radially averaged cross-sections.
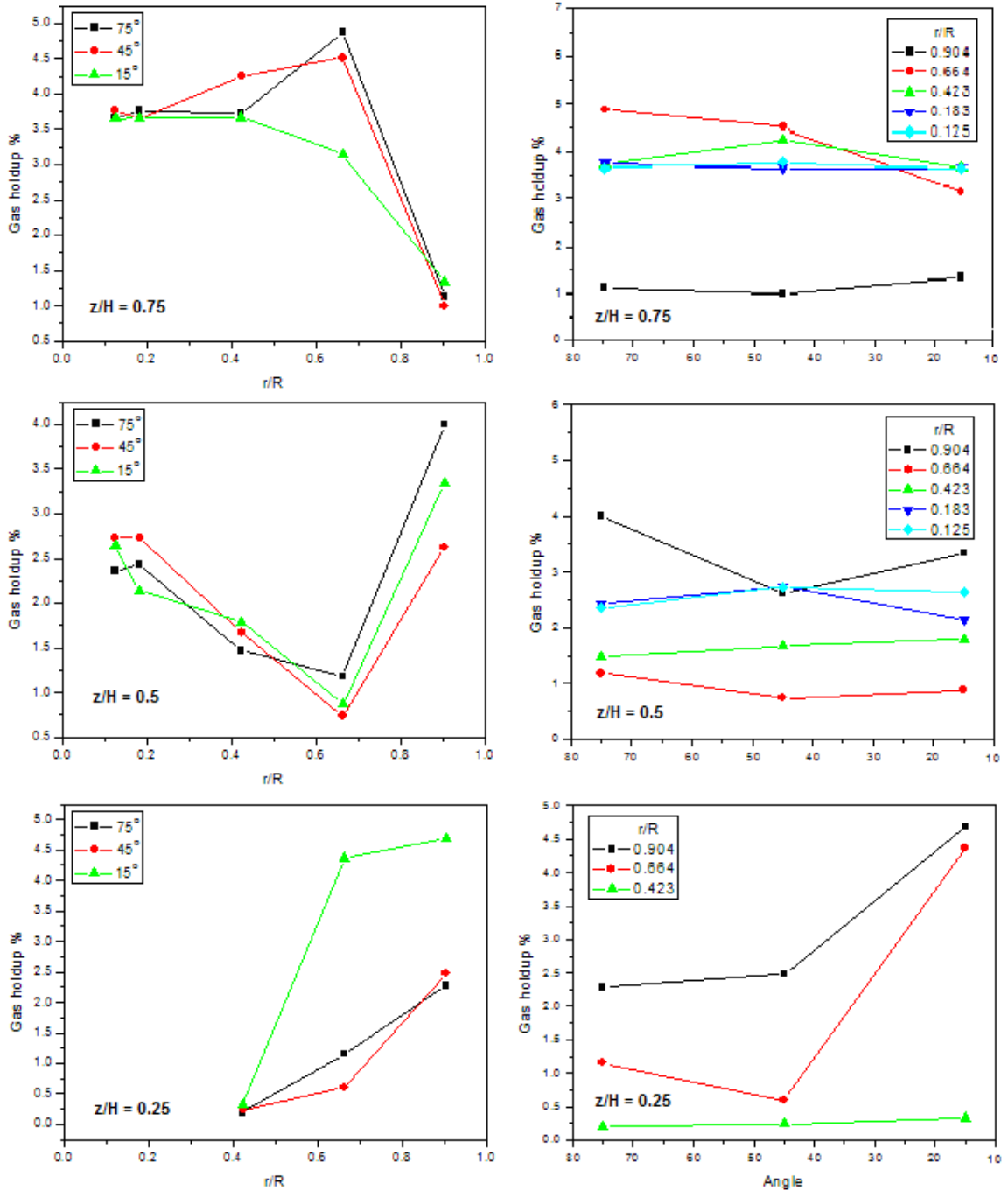
Figure 4.23: Radial and tangential holdup profiles at z/H = 0.5 for the dispersed flow regime

From the above figures it is clear that the baffles have a significant effect on tangential

holdup profiles for ~ r/R > 0.6. The two figures on the bottom show the accumulation

55

of gas below the discharge plane near the leeward baffle (15°) and wall that drops off moving toward the midpoint between the two baffles. The two middle figures confirm the upward flow vortex above the impeller discharge stream that develops near the windward baffle (75°) and wall as well as the overall upward flow along the wall between the two baffles. These results confirm the complex 3-D nature of the flow present in fully dispersed STs (the upward flow vortex on the windward baffle and gas accumulation on the leeward baffle are shown below in Figure 4.24.
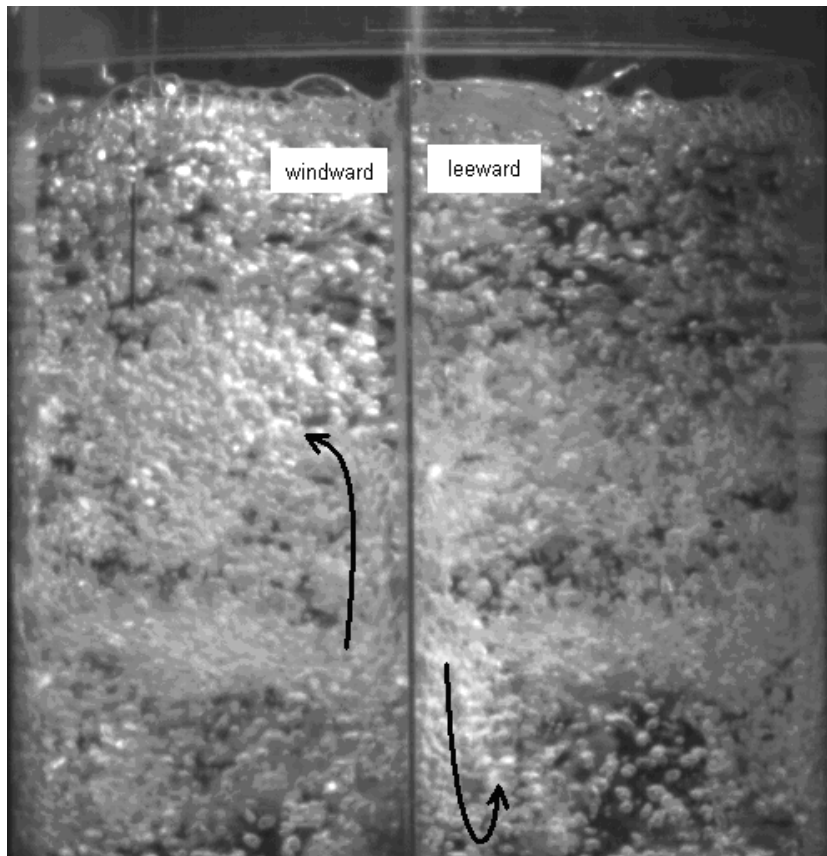
Figure 4.24: Complex 3-D flow above and below the discharge plane of the impeller at 700 rpm and 9.4 L/min

Yet, to the author's knowledge, the only papers quantitatively discussing tangential effects in a ST are those of Laakonen et al. (2005a) and Sudiyo et al. (2007). Their data

focus mostly on bubble sizes, shown below in Figure 4.25. There are many papers in the literature that seek to compare radial holdup profiles, but it is evident that local measurements should truly be compared point by point instead of radially averaging if the complex, 3-D structure of the flow is to be captured and then adequately modeled using CFD.
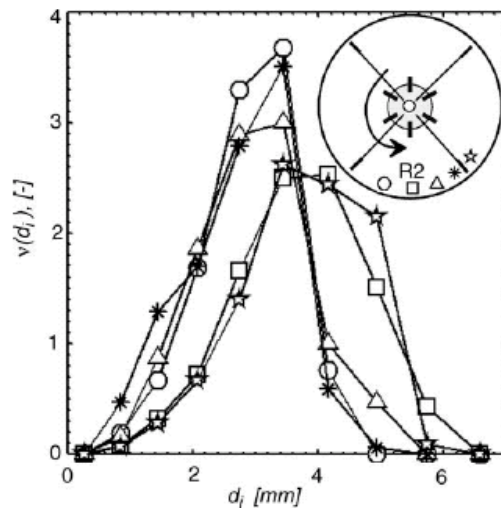
Figure 4.25: Bubble size dependence on tangential location (Source: Laakonen et al., 2005a)

Clearly, the single-point optical probe technique employed in this study (and Wang et al., 2006) is capable of quantitatively mapping the complex 3-D phase holdup structure in a ST. The experiments that follow, using the 4-point mini-probe, are designed not only to confirm and improve the optical probe technique for the quantitative determination of gas holdup but also to demonstrate that the 4-point mini-probe can also quantitatively capture bubble size, interfacial area and bubble velocity distributions.

4.5 4-Point Mini-probe and Bubble Dynamics

When dealing with multi-tip probes there are three concerns that must be addressed before the technique can be confidently used in a gas-liquid flow:

1) What is the cone of acceptance of the probe (the angle comprised by the bubble velocity vector and the probe axis, within which one can accept the results obtained by the probe)?

2) What are general flow patterns in the reactor? – or, more accurately, how many probe orientations are needed to properly characterize bubble dynamics in a complex, 3-D flow?

3) What is the smallest bubble that the probe can accurately measure?

Bombac et al. (1997) noted that there was a slight directional sensitivity in the single-point resistance probe they used to investigate holdup; they found that the sensitivity doesn't vary while the direction of impact with the probe is within the 180° cone of acceptance of the probe and that the holdup values are only slightly reduced (up to 10%) in a cone of acceptance of 320° shown in Figure 4.26. Sun et al. (2006) also used a single-point conductance probe pointed downward in a surface aerated ST, but did not address any directional sensitivity.
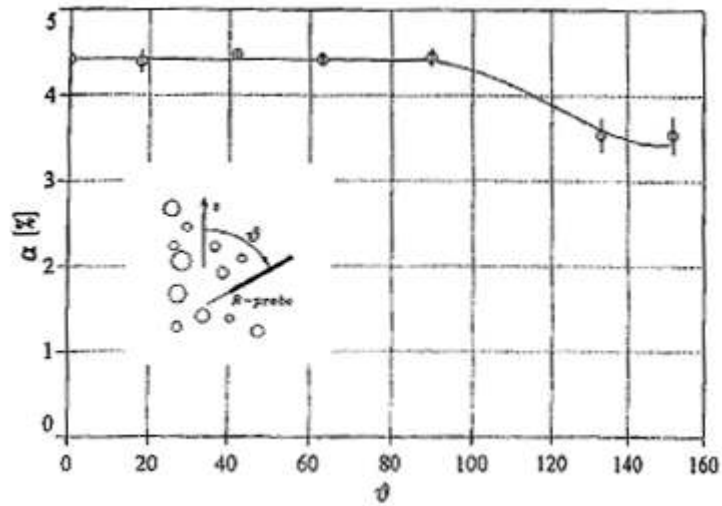
Figure 4.26: Directional sensitivity of a single-point probe (Source: Bombac et al., 1997)

Wang et al. (2006) pointed their single-point optical probe in one orientation (downward in their ST), but gave no discussion of the sensitivity to direction. It will be shown in Chapter 4.5.1 that this leads to error in their holdup measurements in the fully dispersed flow regimes – namely underestimations of gas holdups in the down-flow regions of the ST (near the wall below the impeller discharge stream and near the impeller shaft above the discharge stream).

Two-point probes were the next logical step from single-point probes so that scalar velocities (the bubble speed in the probe direction), and thus chord lengths and interfacial areas could be determined. However, it has been shown previously, in Chapter 3.1, that 2-point probes can only be used in highly directional flows since the 2-point probe creates large errors in velocity outside its cone of acceptance of 25°. Thus, 4-point probes and the necessary algorithm were developed by Xue (2004) so that the

59

probe need not be oriented to the flow to obtain accurate results for bubble velocity vectors, chord lengths and interfacial area.

Xue successfully used his 4-point probe to obtain accurate results in a highly churn-turbulent bubble column by pointing the probe in two directions: upward and downward along the axis of the column. These two required orientations show the need for good statistical sampling in a non-uniform flow. If the probe is only situated such that is was pointed with the major direction of flow, most bubbles are more likely to flow around the probe instead of interacting with the probe tips. By employing two opposing orientations at a location, an almost complete field of view of the flow is given to the probe so that accurate and representative bubble dynamics are obtained. It will be shown later that this orientation scheme is also suitable in most regions of a ST.

The smaller the probe size, the smaller the bubble it is able to detect. Thus, three things need to be taken into consideration with a probe:

- What bubble size distribution is to be expected?
- What data is required? – just gas holdup? or also bubble dynamics?
- Is the flow highly directional or very complex/chaotic?

If the expected bubble sizes are small (mean bubble diameter on the order of 1 mm) then the probe needs to be made as small as possible to capture the smaller spectrum of bubbles. If the expected size of bubbles is larger (on the order of 1 cm) the probe size used by Xue (2004) of 1.4 mm in diameter will work well. If bubble dynamics data is

required, then a 4-point probe will be required. But, if holdup is the only data needed, a single point probe will suffice and can be made very small (on the order of 100 microns). If the flow is highly directional, the 4-point probe can be reduced to a 2-point probe (further reducing the size). But, if the flow is very complex, only a 4-point probe will yield accurate results for bubble dynamics.

In the realm of well-dispersed STs small bubbles sizes can be expected, the spectrum of bubble dynamics are required, and the flow is very complex and chaotic. Thus, Xue's (2004) 4-point probe was reduced in diameter from 1.4 mm to 0.625 mm by using smaller fibers (125 μm in diameter) and by packing them closer together while still keeping the same geometrical aspects.

4.5.1 Results

Similar to Chapter 4.4.1, three horizontal planes at elevations of z/H = 0.75, 0.5, and 0.25 were examined along the axis of one quadrant in the 20 cm ID ST, shown below in Figure 4.27.
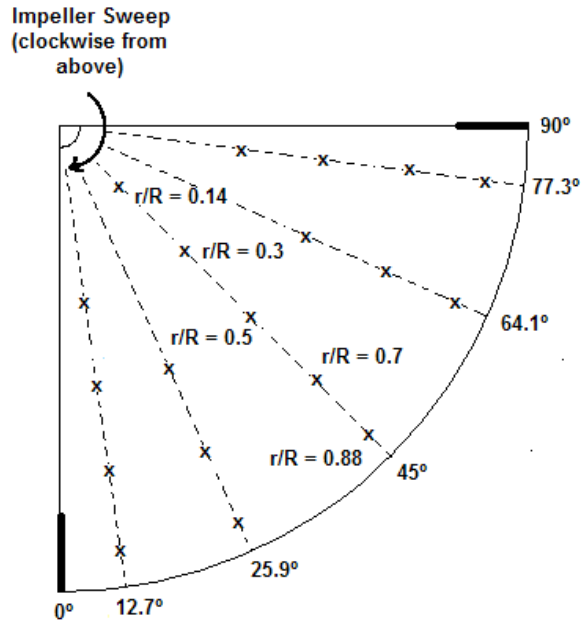
Figure 4.27: Measurement locations at z/H = 0.75, 0.5, and 0.25 (note: at z/H = 0.25, r/R = 0.14 and 0.3 are not taken do to interference of the probe in the impeller sweep)

A base case study at all radial, axial and tangential points was conducted at 500 rpm and 8.7 L/min (Fr = 0.472 and Fl = 0.058 – the dispersed regime in the S33 structure according to Figure 2.11). For comparison to this base case, radial and axial measurements at 45° were taken in four other operating conditions by either increasing or decreasing the impeller speed or gas flow rate from the base case. These other conditions studied were: 350 rpm (Fr = 0.231 and Fl = 0.083 – at the flooded/bubble column flow regime), 750 rpm (Fr = 1.063 and Fl = 0.039 – the S33 dispersed regime with recirculation), 12.5 L/min (Fr = 0.472 and Fl = 0.086 – the S33 dispersed regime), and 4.4 L/min (Fr = 0.472 and Fl = 0.030 – the VC dispersed regime). Images of the 5 operating conditions are shown below in Figure 4.28. Measurements were taken with the 4-point mini-probe pointing downward and upward for good statistical sampling and in triplicate to obtain an understanding of variance in the measurements.

Measurements were also taken in the impeller discharge stream with the mini-probe facing inward toward the flow.

500 rpm & 12.5 L/min

350 rpm & 8.7 L/min

500 rpm & 8.7 L/min

750 rpm & 8.7 L/min

500 rpm & 4.4 L/min
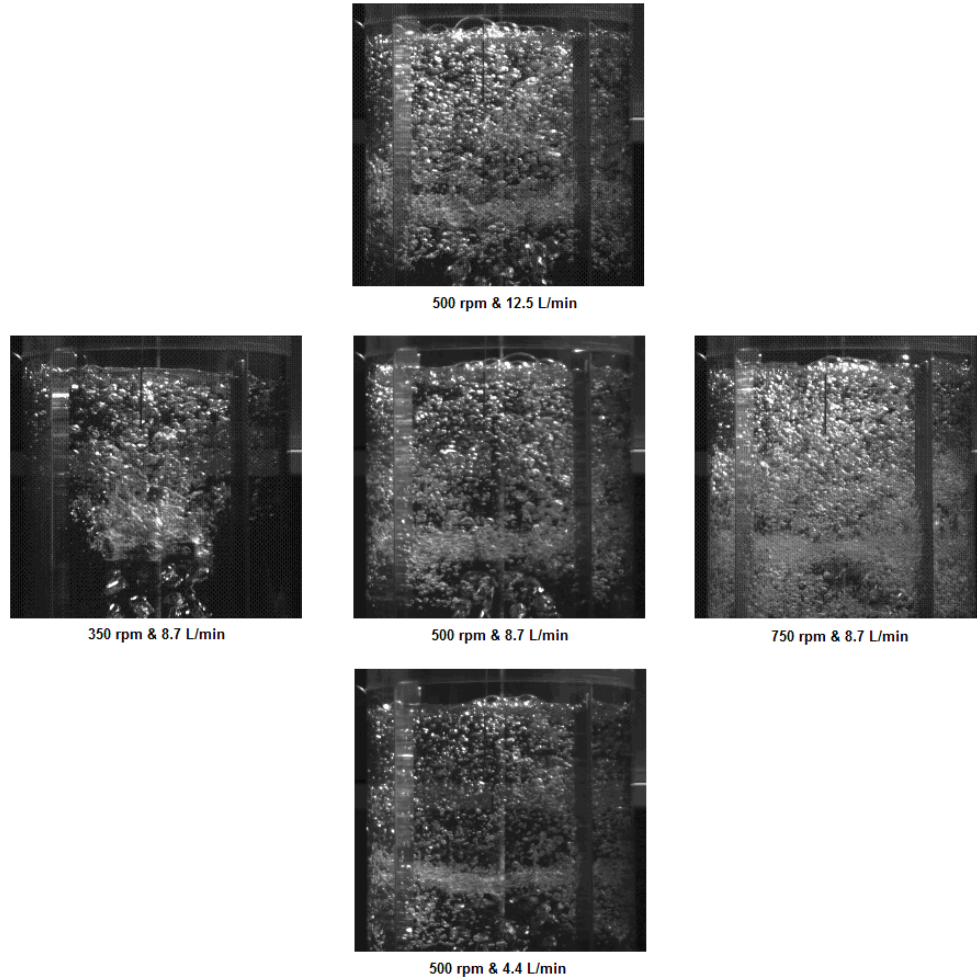
Figure 4.28: Pictures of the 5 investigated conditions (base case in the middle)

The need for two measurements (with the probe direction changed by 180 degrees from the upward to the downward direction) is highlighted in Figure 4.29 for the dispersed regime with recirculation. Here, the downward pointing probe consistently underestimates the gas holdup (by nearly 2X) compared to the upward pointing probe in the gas down-flow regions: $r/R < 0.8$ at the $z/H = 0.5$ plane and $r/R > 0.8$ in the

z/H = 0.25 plane.   (Note also that there is very little down-flow in the z/H = 0.75

plane.)   Flow outside the impeller discharge stream is mostly in the vertical directions.

Thus, outside the impeller discharge stream, opposing probe orientations were

implemented at each measurement point to obtain accurate bubble dynamics results.

Inside the impeller discharge stream, the probe is oriented facing the flow. These three

probe orientations are the minimum required.   For instance, if a scalar velocity

distribution is needed at a particular point and the flow field structure is unknown, six

orientations should be used to capture the axial, radial, and tangential velocities (2

opposing orientations for each direction).
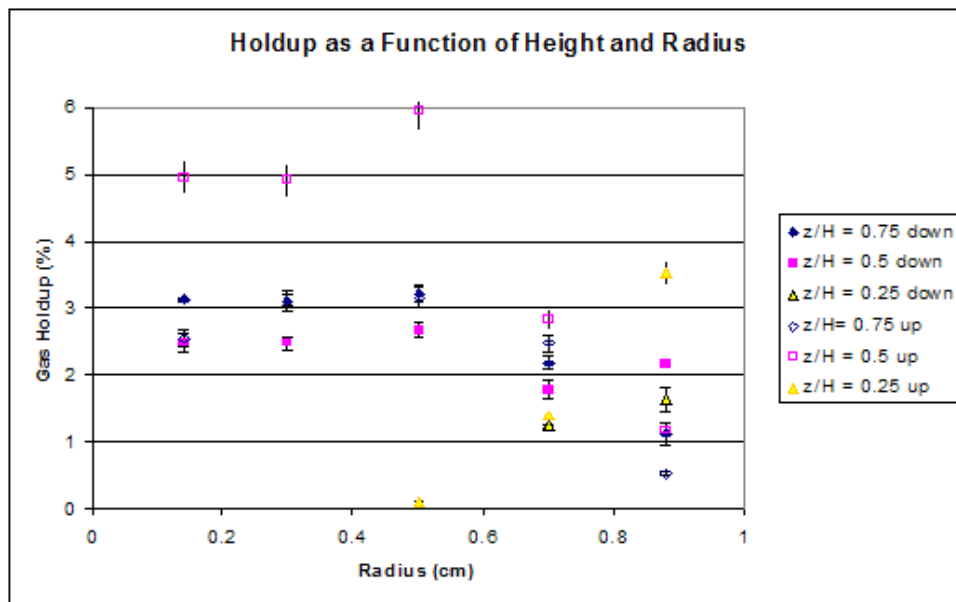
Figure 4.29: Holdup at 750 rpm and 8.7 L/min & need for opposing probe orientations

4.5.1.1 Gas Holdup

The results for gas holdup are presented in Figure 4.30 for the base case condition.
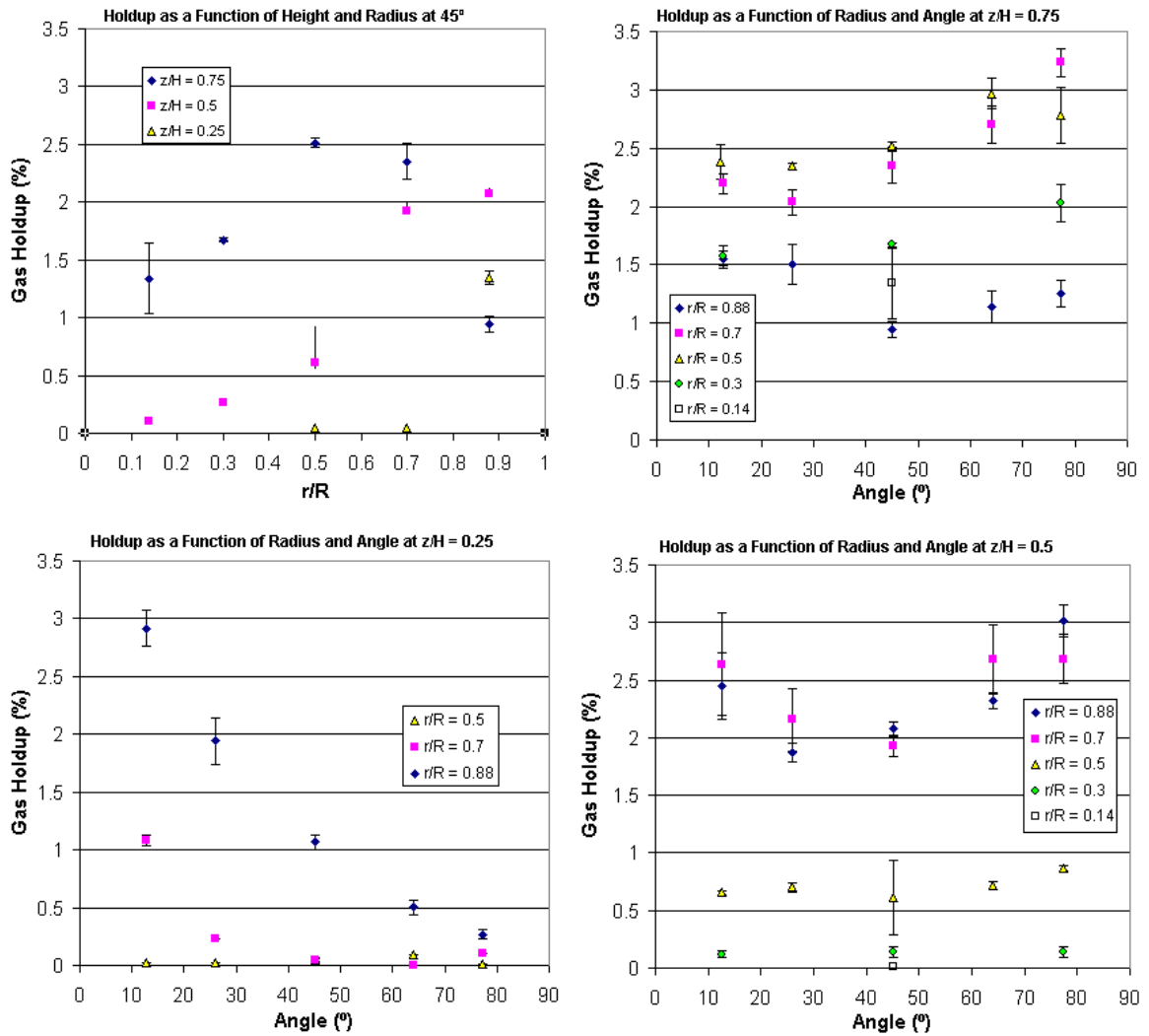
Figure 4.30: Holdup results at 500 rpm and 8.7 L/min (base case)

In the top left figure, the radial gas holdup profiles exhibit a somewhat concave

downward shape, with a maximum at ~ r/R = 0.5 at z/H = 0.75 (a shape similar to the

dispersed regime obtained in Figure 4.20). However, a monotonically increased gas

holdup with radial position is observed at the other two planes at z/H = 0.5 and 0.25.

The other three figures confirm the observations from Chapter 4.4.1 of gas

accumulation below the impeller plane near the leeward baffle that becomes less

pronounced moving away from the wall and of the upward flow vortex that forms above the impeller plane at the windward baffle. The variance at any one point is never more than one half of one percent of gas holdup.

Figure 4.31 shows how the gas holdup varies from the base case with gas flow rate and with impeller speed. As the gas flow rate increases, the gas holdups increase. Notice how the overall shape at $z/H = 0.75$ does not change with gas flow and how the maximum in gas holdup moves away from the wall at $z/H = 0.5$ as the gas flow rate increases (bubbles curl away from the wall as they rise away from the impeller discharge stream). Comparing the results at the different impeller speeds shows the changes in flow regimes: the characteristic drop-off in the flooded regime and the increasing holdups in the region near the impeller shaft in the dispersed regime with recirculation. In the dispersed regimes (not including the dispersed regime with recirculation), gas holdups in the impeller discharge plane are at least 3X larger than holdup values in the rest of the tank, decrease very rapidly moving away from the impeller toward the wall, and increase with gas flow rate. At constant gas flow rate, increasing the impeller speed decreases the gas holdup in the impeller discharge stream near the impeller since the gas is better distributed throughout the rest of the ST.

66
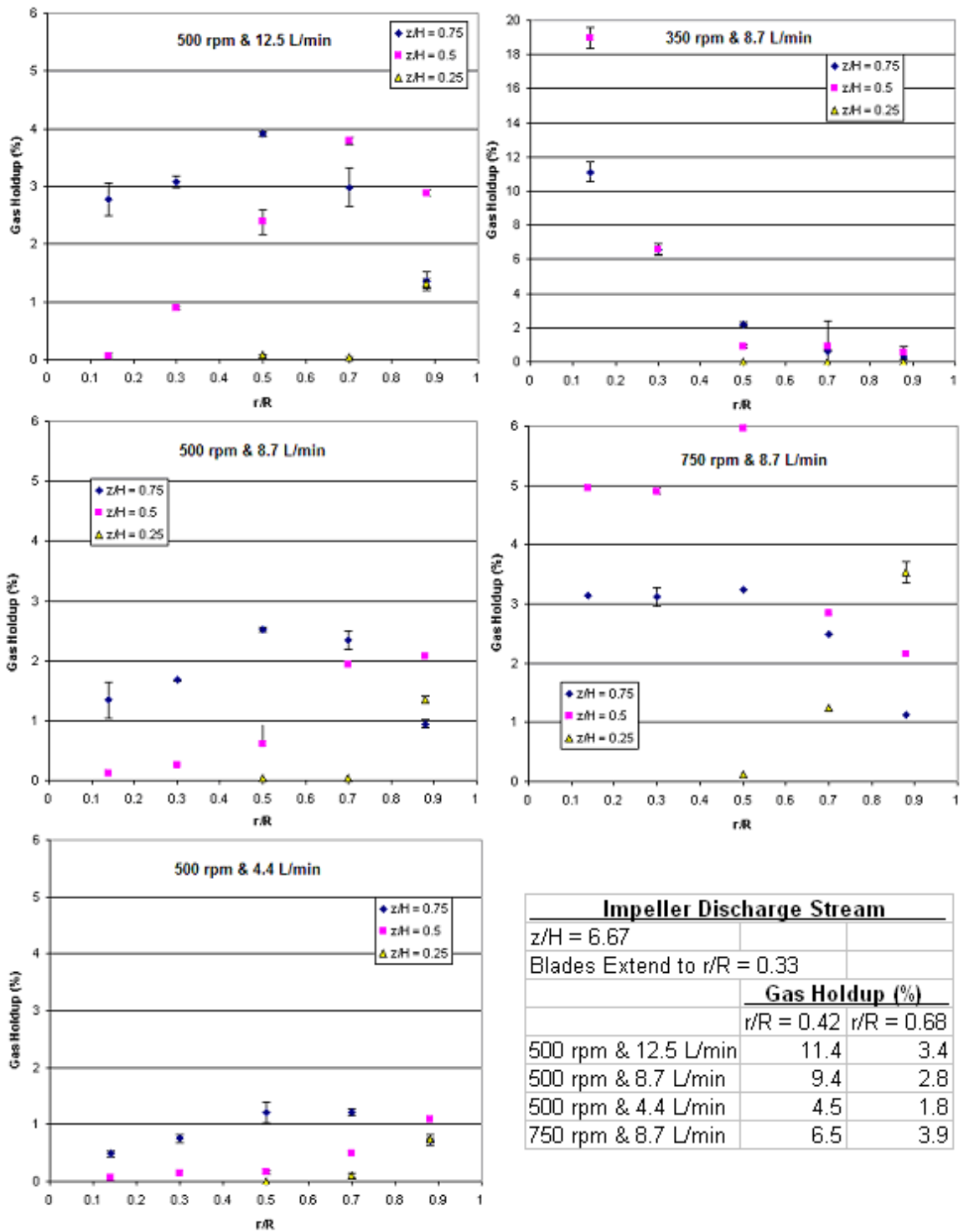
Figure 4.31: Variations in radial and axial gas holdups with impeller speed and gas flow rate

It should be stressed that to obtain accurate gas holdup values, upward and downward orientations of a single point probe are needed to obtain accurate results at any location in the tank. If there is a significant difference between the values obtained by upward and downward orientations, the larger gas holdup value should be reported since the probe (in that orientation) interacts with more of the bubble population.

4.5.1.2 Bubble Chord Length Distribution

Based on their measurements, Machon et al. (1997) presented the following mean Sauter diameters as a function height in a 15 cm ID ST for air-water at 770 rpm and a gas flow rate of 3 L/min in Figure 4.32.
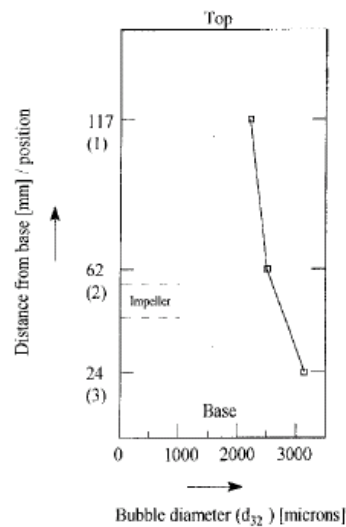
Figure 4.32: Mean Sauter diameter as a function of height near the wall
(Source: Machon et al., 1997)

Cents et al. (2005) studied a 45 cm ID ST at a sparging gas flow rate of 55.3 L/min and provided mean Sauter bubble diameters for an air-water system as a function of impeller speed as shown in Figure 4.33. Near the impeller, the mean Sauter diameter decreases

with increasing impeller speed. However, it should be noted that these results do not show the bubble size distribution at each location – the Sauter mean diameter accurately applies to spherical bubbles but does not precisely describe ellipsoidal bubbles that are also expected in Cents et al.'s (2005) experiments.
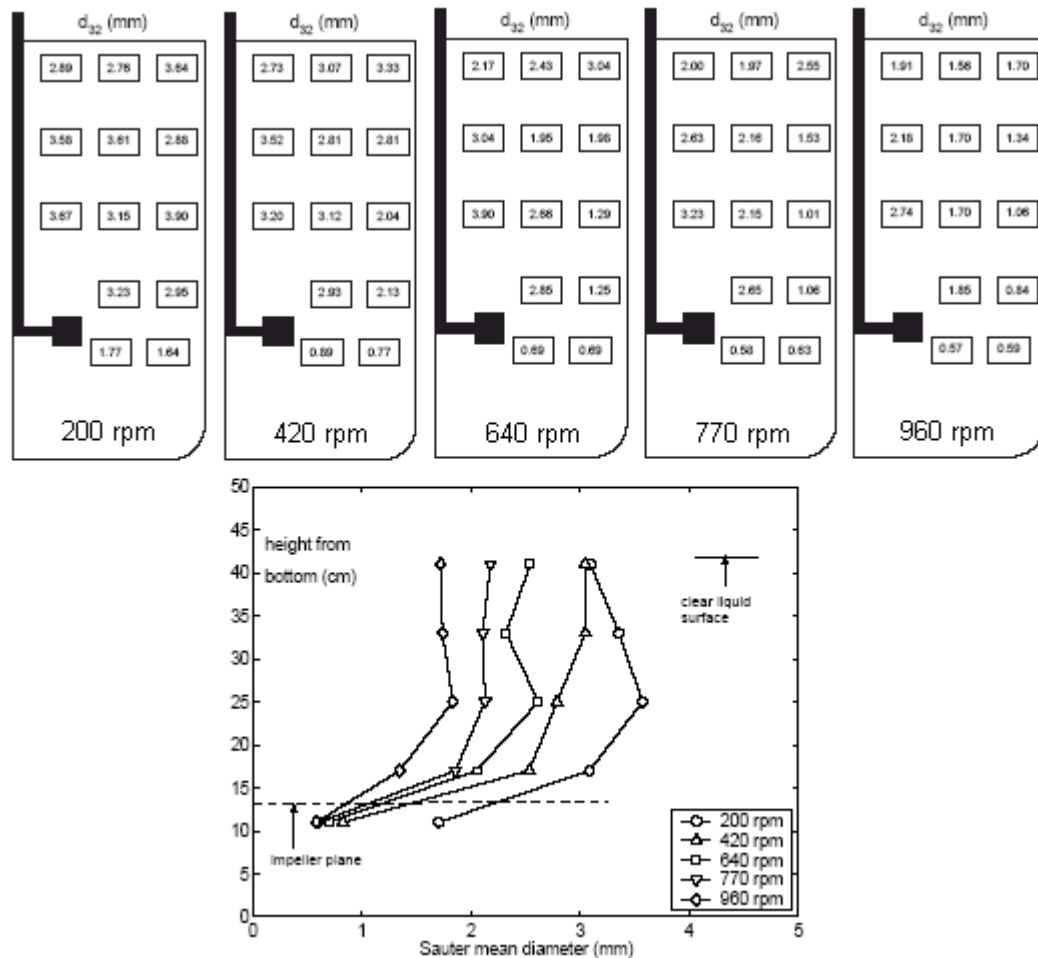
Figure 4.33: Influence of impeller speed on Sauter mean diameters (Source: Cents et al., 2005)

It should be stressed here that unless it is known that very small bubbles (so that they may be assumed hard spheres) exist in a gas-liquid system, a Sauter mean diameter does not truly describe the bubble size. In complex multiphase flow, bubbles often fluctuate

69

from a standard geometry, so the idea of a diameter describing size can only provide a qualitative description.

Laakonen et al. (2005a) investigated a 26 cm ID ST of air-deionized water at 500 rpm and very low gas flow rates (1 L/min and below) and provide estimated bubble size distributions in Figure 4.34 below (using a capillary suction method to obtain the Sauter mean diameter, which assumes a spherical geometry for all bubbles). Increasing the gas flow rate broadens the BSD which has a range of ~ 0.1 – 6 mm.
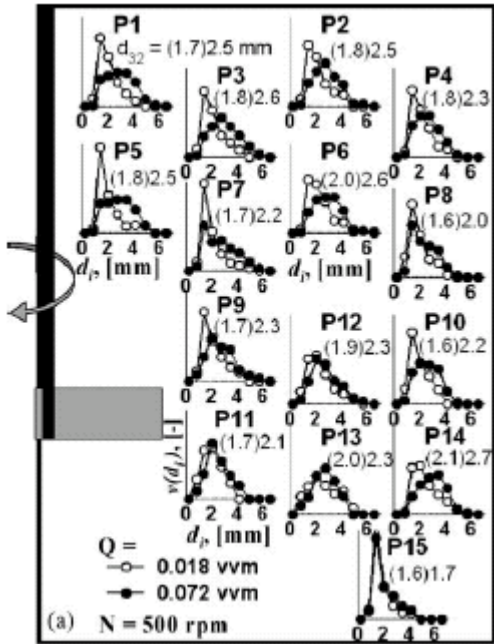
Figure 4.34: BSDs in a ST (Source: Laakonen et al., (2005)

Since bubble sizes have not been investigated at the experimental conditions carried out in this research, the bubble chord-length distribution obtained by the 4-point mini-probe was validated by using in-situ borescopy. The borescope (Hawkeye Rigid Pro by Gradient Lens Corporation) was inserted into the ST from the top so that it was

pointed downward. A thin filament of wire (5 mm long and 0.4 mm in diameter) was affixed in front of the end of the borescope (10 mm away from the face of the borescope) and used as an objective point, whereby the diameters of bubbles near the objective could be measured within an accuracy of 0.1 mm anywhere in the ST (shown below in Figure 4.35). In this manner, hundreds of frames of bubbles were investigated, and hundreds of bubble diameters near the objective were measured.
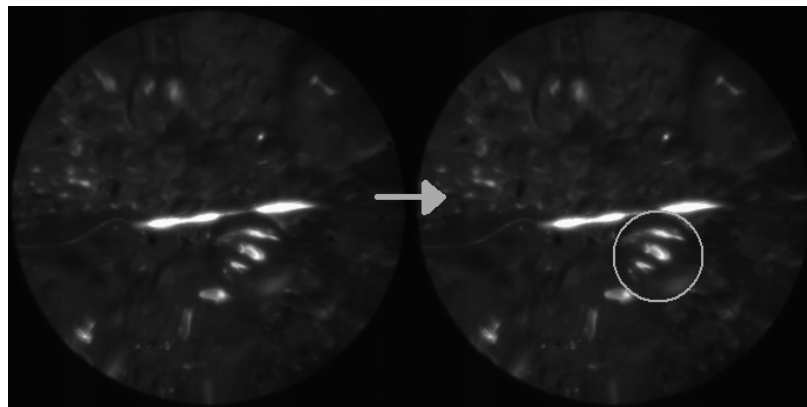
Figure 4.35: Bubble size captured by borescopy

Histograms of the base case at $z/H = 0.75$ & $r/R = 0.88$ are shown below in Figure 4.36.
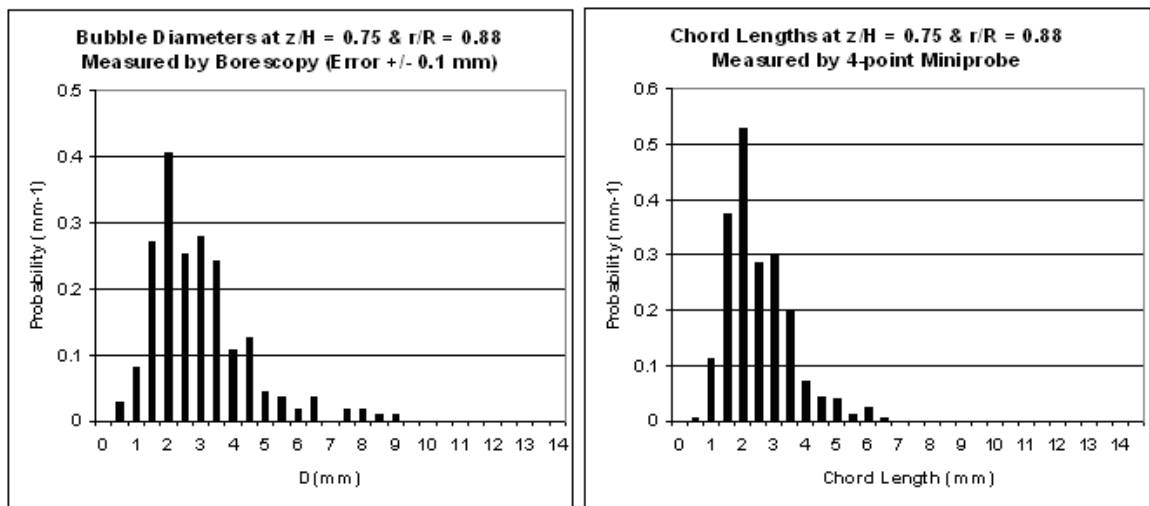
Figure 4.36: Comparison of BSD obtained by borescopy and the mini-probe

71

Note how the maximum of the two distributions match, each peaking at a length of about 2 mm and trailing off beyond 4 mm. The larger tail in the borescopy data can be explained as follows: larger bubbles are more ellipsoidal. Since the borescope is pointed downward, it sees the broader face of these ellipsoidal bubbles (major axis), whereas the mini-probe measures the length perpendicular to the broad face (minor axis) of ellipsoidal bubbles. For the smaller, spherical bubbles this effect vanishes. External high-speed photography at the positions along wall (that measures the minor axis of the ellipsoidal bubbles) match the distributions obtained by the 4-point mini-probe very well and do not show the longer tail that a downward oriented borescope shows.

The effect of operating conditions on the mean bubble chord length is shown below in Figure 4.37. The means for the dispersed regimes fall in the expected ranges for air-water systems reported by Machon et al. (1997), Laakonen et al. (2005) and Cents et al. (2005). Increasing the gas flow rate or decreasing the impeller speed increases the mean bubble chord length.

		r/R				
	z/H	0.14	0.30	0.50	0.70	0.88
500 rpm & 12.5 L/min	0.75	2.89	2.54	2.61	2.37	2.21
	0.50	2.48	3.27	2.86	2.75	2.70
	0.25	na	na	none	1.81	2.08
500 rpm & 8.7 L/min	0.75	2.39	2.30	2.21	2.25	2.26
	0.50	2.32	2.32	2.41	2.67	2.26
	0.25	na	na	3.67	1.68	2.10
500 rpm & 4.4 L/min	0.75	2.11	1.93	1.89	1.92	1.85
	0.50	none	1.77	2.36	1.85	1.89
	0.25	na	na	none	1.61	2.33
750 rpm & 8.7 L/min	0.75	2.37	2.32	2.25	2.22	2.12
	0.50	1.87	2.04	2.31	2.63	2.29
	0.25	na	na	1.87	1.95	1.83
350 rpm & 8.7 L/min	0.75	3.58	3.52	3.05	na	na
	0.50	4.66	3.27	2.56	na	na
	0.25	na	na	na	na	na

Figure 4.37: Effect of operating conditions on mean bubble chord length (in mm)

For the most part, bubble size decreases with an increase in height above the impeller discharge stream; however, it truly depends on the location (depending on the flow regime).

In Chapter 4.5.1.1, the gas holdup was found to vary significantly with tangential location. In Figure 4.38 below, the mean chord lengths show much less variance with tangential location, with a range between $\sim$ 2 – 2.4 mm at z/H = 0.75 and 2 – 2.8 mm at z/H = 0.5.

	Angle	r/R 0.14	0.30	0.50	0.70	0.88
500 rpm & 8.7 L/min z/H = 0.75	77.3	na	2.30	2.23	2.18	2.28
	64.1	na	na	2.22	2.18	2.09
	45.0	2.39	2.30	2.21	2.25	2.26
	22.9	na	na	2.28	2.14	2.01
	12.7	na	2.33	2.23	2.14	1.94
500 rpm & 8.7 L/min z/H = 0.50	77.3	na	2.36	2.76	2.71	2.32
	64.1	na	na	2.45	2.77	2.13
	45.0	2.32	2.32	2.41	2.67	2.26
	22.9	na	na	2.26	2.74	2.10
	12.7	na	2.03	2.42	2.58	2.17

Figure 4.38: Mean bubble chord length (in mm) dependence on tangential location above the impeller

But, truly the bubble chord length distributions should be considered when looking for insights on bubble size – especially for CFD modeling. At the conditions investigated in this work, the bubble chord length distributions follow a lognormal distribution. Consider the flooded flow regime below in Figure 4.39. As the location moves closer to the impeller, the chord length distribution begins to broaden. At z/H = 0.5 and r/R = 0.14, the mean chord length is (from Figure 4.37 above) 0.46 cm. Yet, the distribution spans an entire order of magnitude (0.1 cm to 1 cm and above).
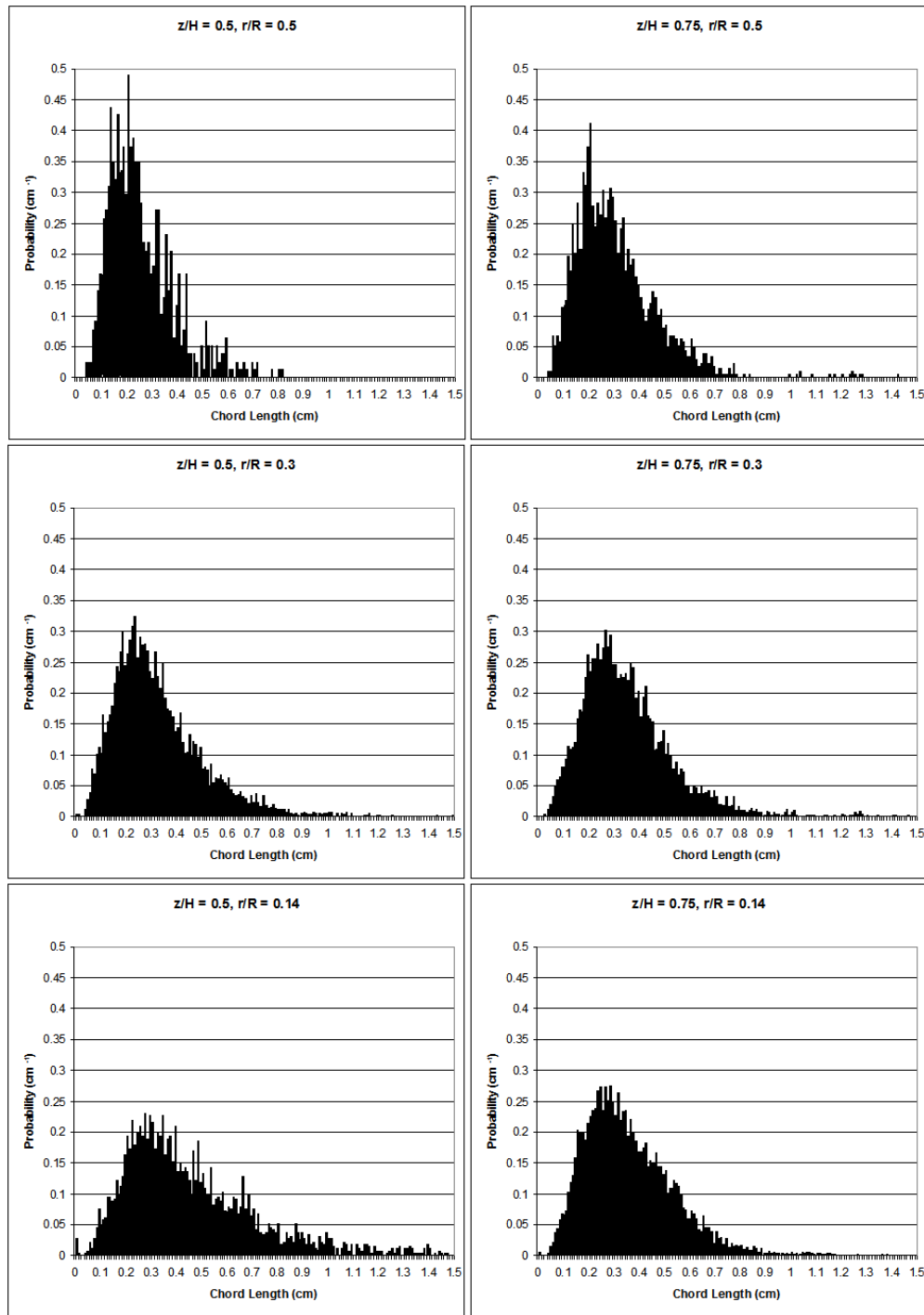
Figure 4.39: Shift in lognormal distribution with position in the flooded regime

This broad span in the distribution is characteristic for the flooded regime. Note how much narrower the distributions are for the dispersed regimes in Figure 4.40.

74
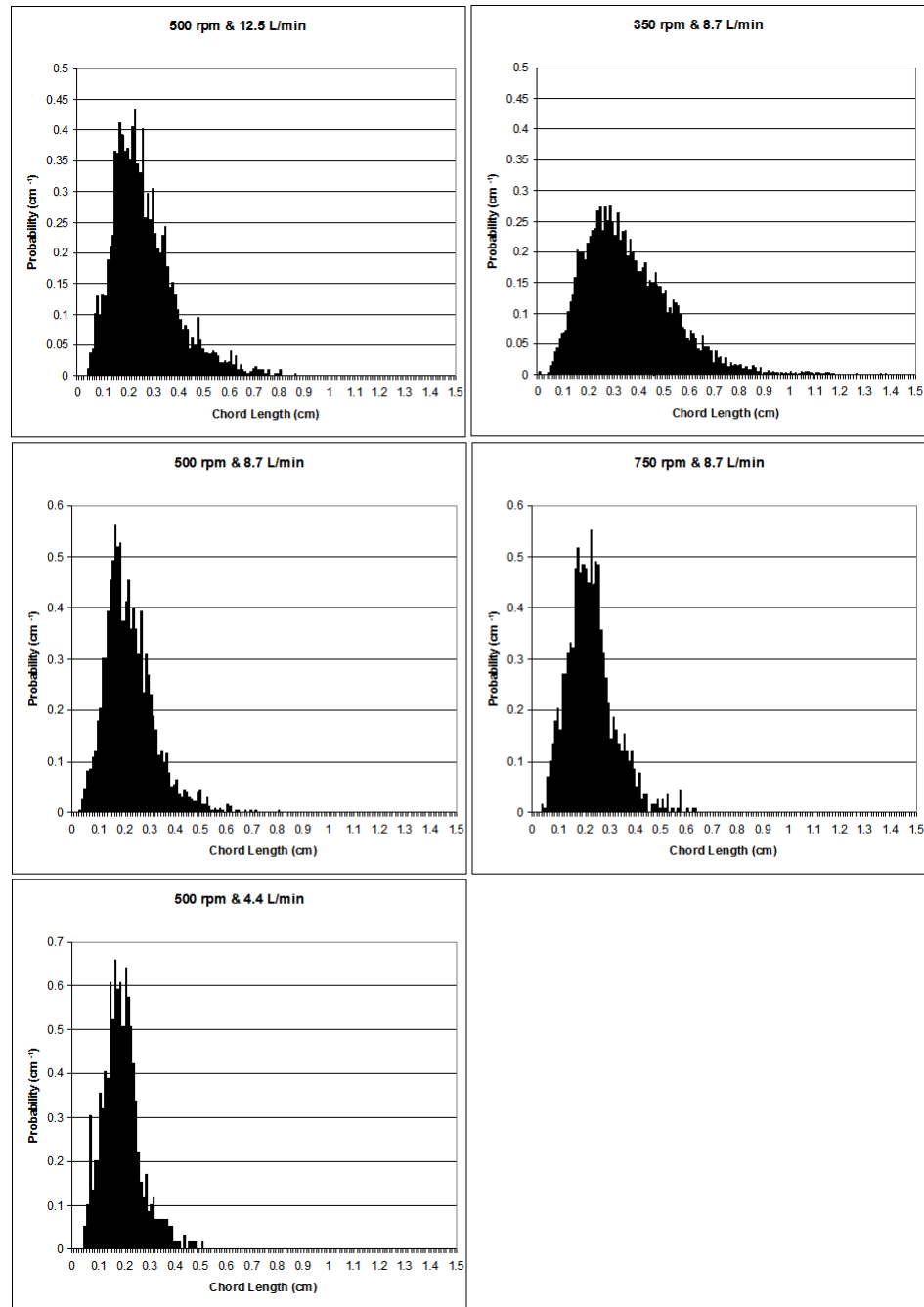
Figure 4.40: Change in distribution with operating conditions at z/H = 0.75 and r/R = 0.5

As the flow rate increases note how the distribution broadens and shifts to the right (from a range of 0.5 – 5 mm at the low gas flow rate to 0.5 – 8 mm at the high flow rate). Increasing the impeller speed did not shift the distribution range noticeably from

the dispersed regime to the dispersed regime with recirculation. Thus, low flow rates

and high impeller speeds produce a much narrower spectrum of bubble sizes – this is

greatly evidenced in the impeller discharge stream (shown in Figure 4.41).
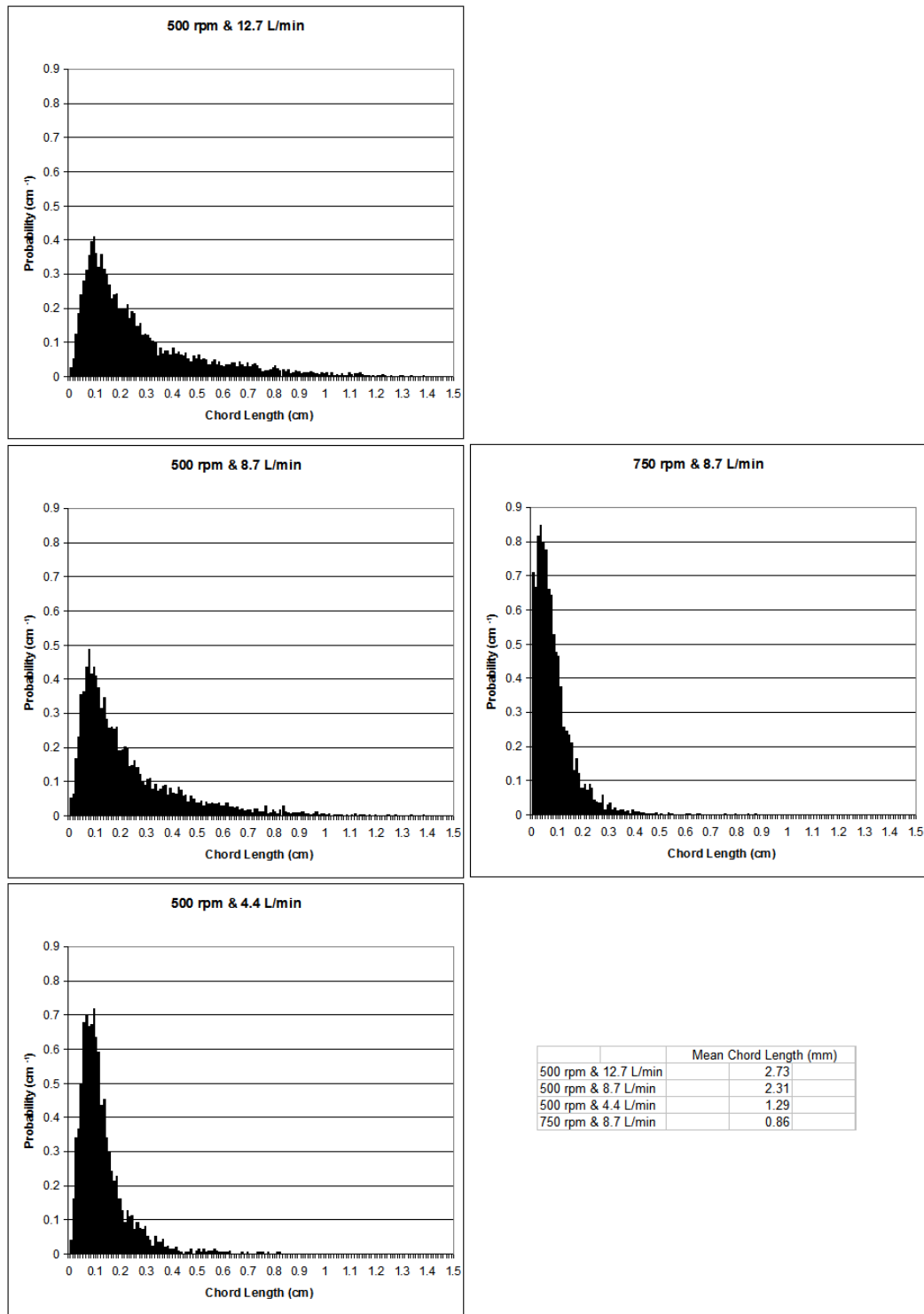
Figure 4.41: Chord length distributions at z/H = 0.67 and r/R = 0.42

	Mean Chord Length (mm)
500 rpm & 12.7 L/min	2.73
500 rpm & 8.7 L/min	2.31
500 rpm & 4.4 L/min	1.29
750 rpm & 8.7 L/min	0.86

In the impeller discharge stream, the same effect of the increase in gas flow rate on broadening the distribution can be seen. It should be noted that in the impeller discharge stream at the dispersed regime with recirculation, the mean bubble size is very close to the limit of the bubble size that the 4-point mini-probe is able to capture, yet the probe still describes the distribution very well.

An example of the effect of radial distance from the impeller tips on the chord length distributions is shown below in Figure 4.42. The lognormal distributions shift to the right but their ranges narrow.
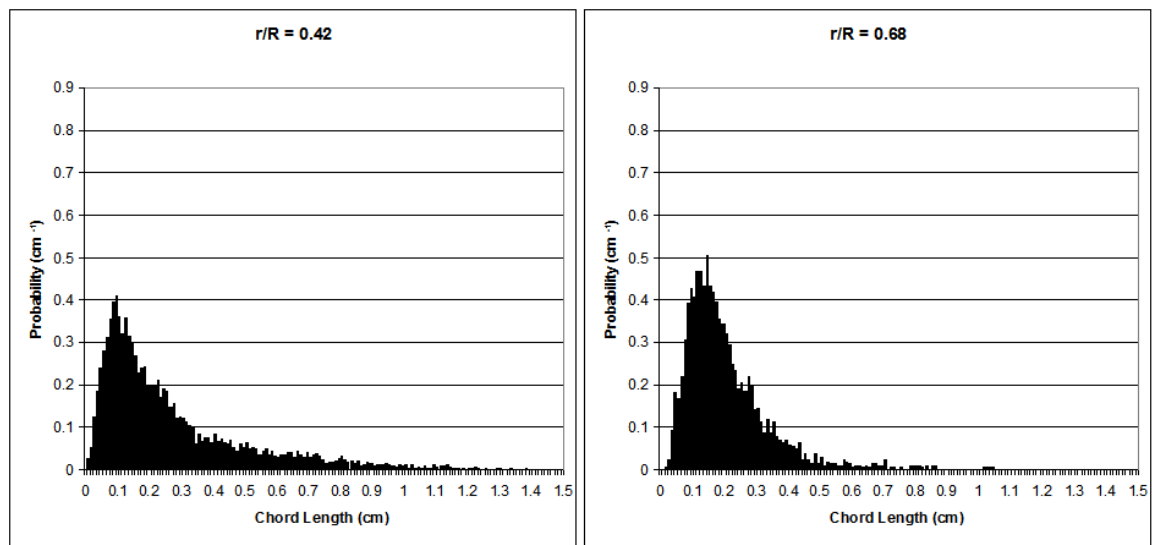
Figure 4.42: Shift in distribution in the impeller discharge plane (z/H = 0.67) with distance from the impeller tip (r/R = 0.33)

The above figure demonstrates that the mean chord length (2.73 mm at r/R = 0.42 and 2.06 mm at r/R = 0.68) does not tell the entire story of what occurs in the impeller discharge stream. The means would lead one to believe that the bubble sizes shrink as the distance from the impeller tips increases. Yet, the distributions show that this

shrinkage is due to a lesser presence of larger bubbles (the large bubble rising up from the sparger) and that the maximum in the distribution of chord length is actually larger further from the impeller tips.

The 4-point mini-probe was found to be able to capture bubble dynamics for bubbles diameters of ~ 0.85 mm and above. Thus, the chord length distributions obtained from the 4-point mini-probe are accurate, acceptable and have been confirmed by both in-situ borescopy and external high-speed photography at the wall. Since the chord lengths of each individual bubble are calculated from the velocity of each individual bubble (shown in Chapter 3.1.1), the velocities obtained by the mini-probe are also validated by the bubble chord length distributions.

4.5.1.3 Specific Interfacial Area

Middleton (1985) states that the overall specific interfacial area (SIA) in a ST should be expected in the range of $1 - 5$ cm^2/cm^3. The data in the literature confirms this range, and in most studies this range shifts to lower values. Cents et al. (2005) show the effect of impeller speed on interfacial area (at the same operating conditions described in Chapter 4.5.1.2) – values ranging from $0.2 - 4$ cm^2/cm^3 shown in Figure 4.43.
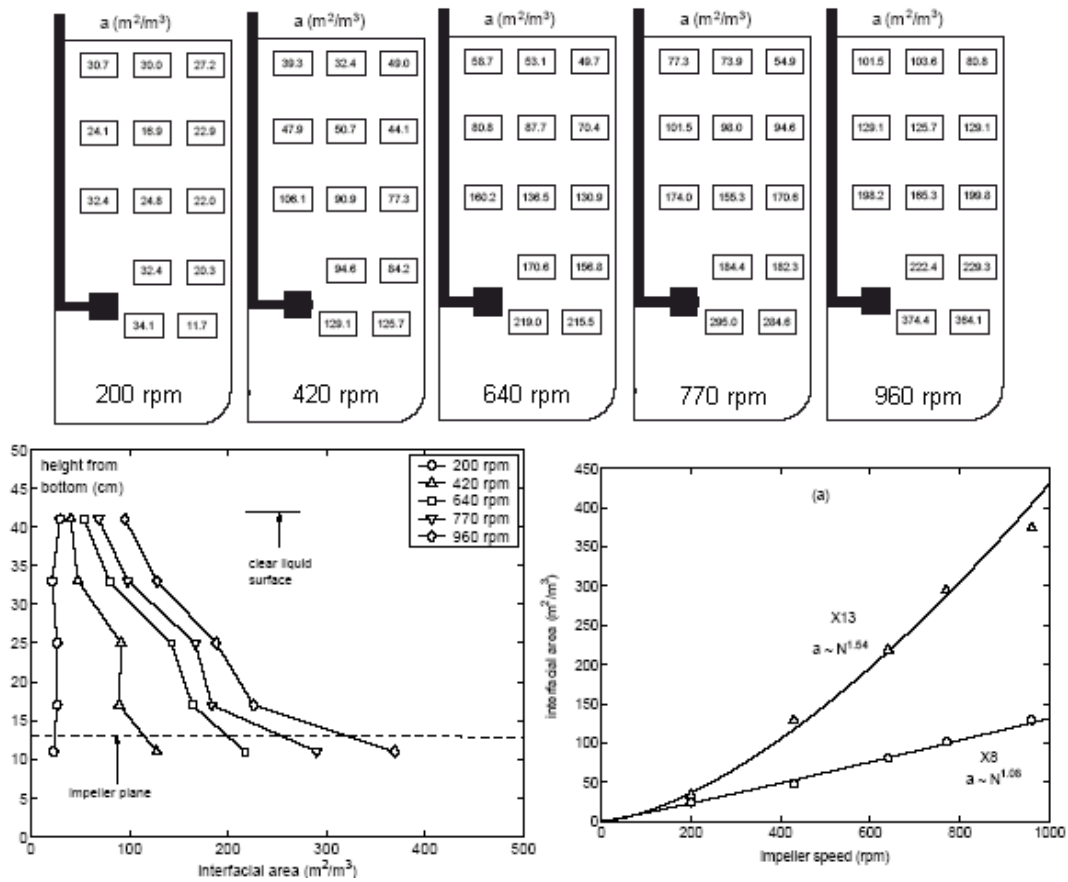
Figure 4.43: Effect of impeller speed on interfacial area (Source: Cents et al., 2005)

Clearly, increasing the impeller speed generates more interfacial area in a ST. However, a significant gradient in SIA is seen between the impeller discharge stream and the rest of the reactor as the impeller speed increases.

The results for specific interfacial area for the base case of this study are presented in Figure 4.44 and range from $0 – 0.9$ cm^2/cm^3 outside the impeller discharge stream.

80
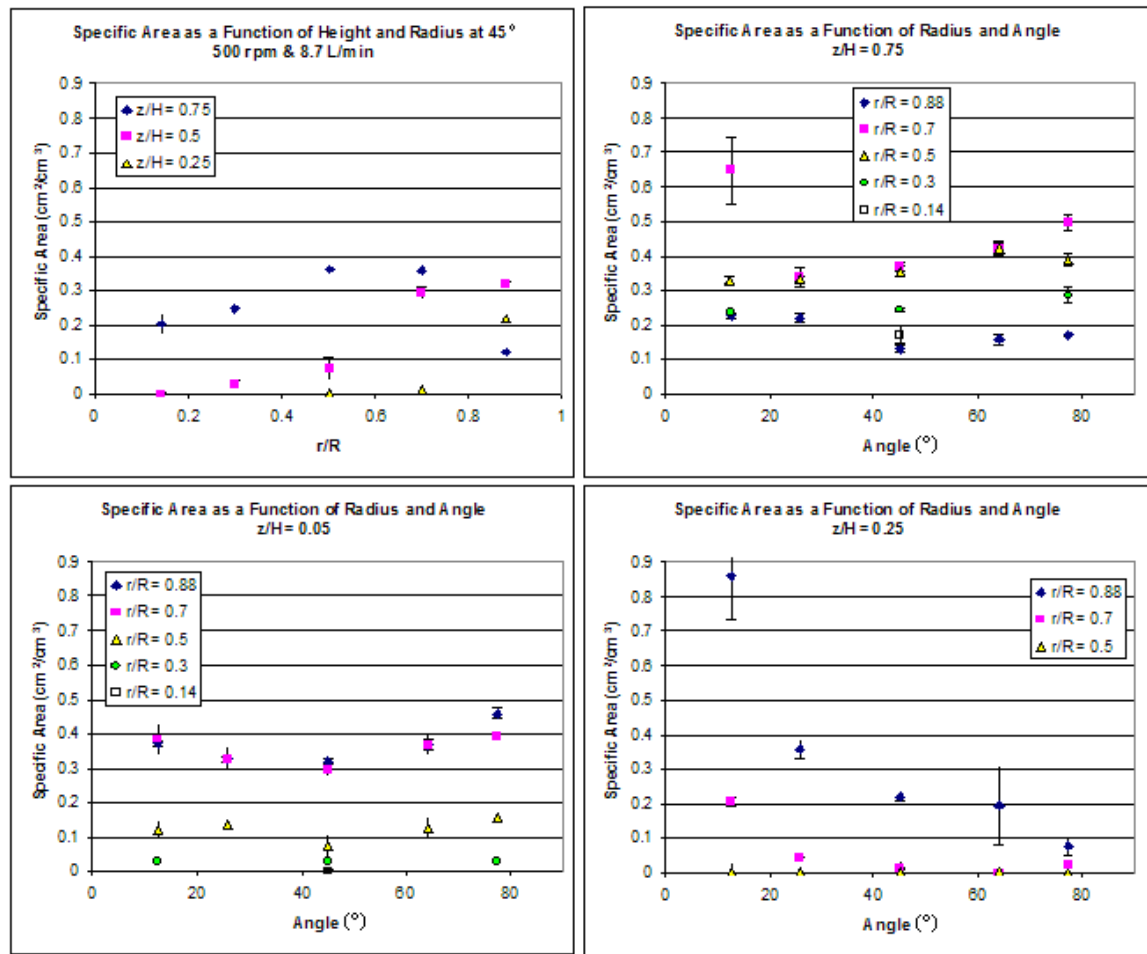
Figure 4.44: Specific interfacial area at the base case

Notice that the SIA varies dramatically depending on the location in the ST – in some instances the difference is an order of magnitude. The above figures highlight that most of the interfacial area, outside of the impeller discharge stream, is generated near the wall of the ST and shifts away from the wall of the ST closer to the free liquid surface (similar to Cents et al., 2005). The bottom right figure again highlights the accumulation of gas near the leeward baffle beneath the impeller discharge stream.

Figure 4.45 shows the effects of changing the gas flow rate or impeller speed.
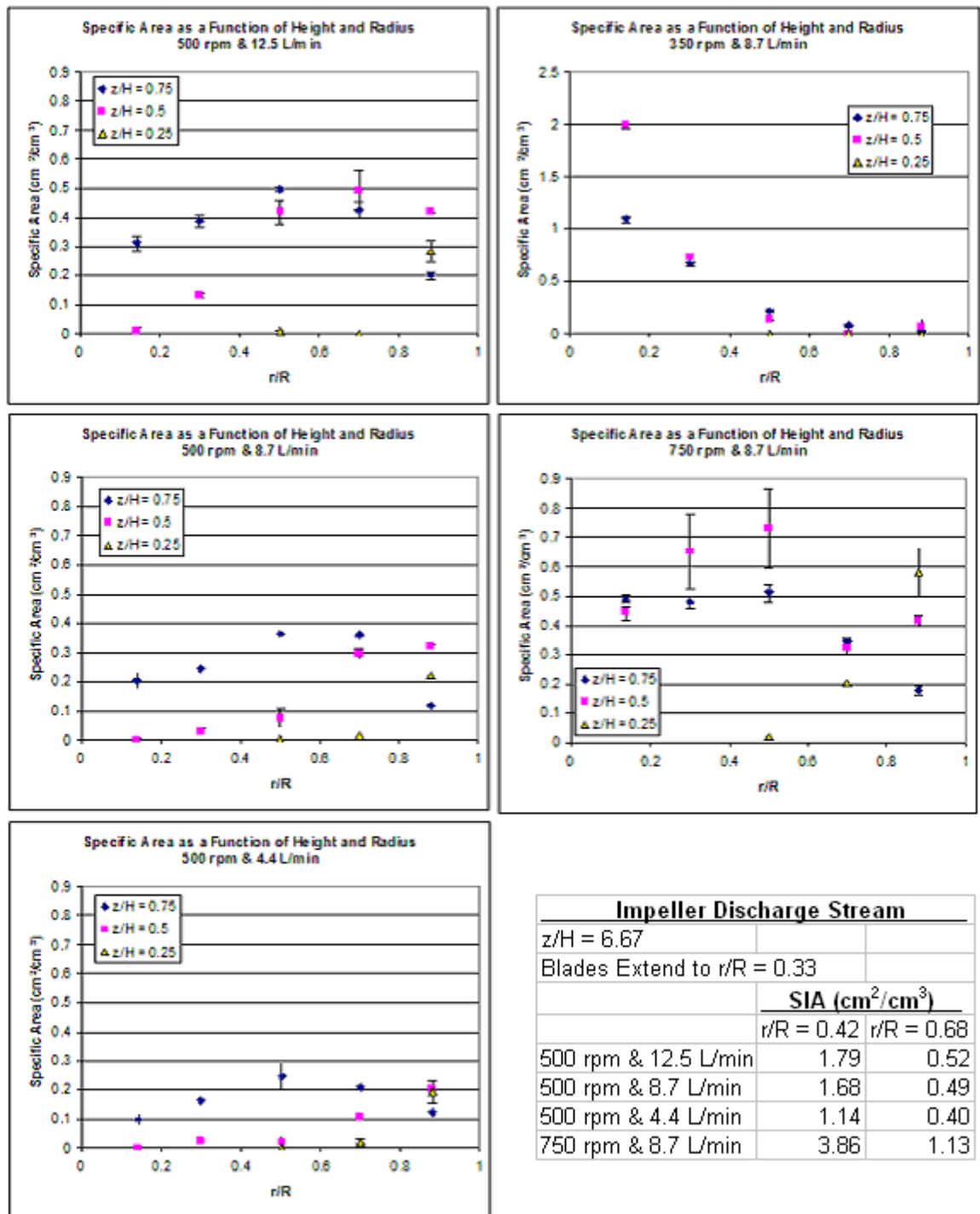
Figure 4.45: Effect of operating conditions on specific interfacial area at an angle of 45°

Impeller Discharge Stream		
z/H = 6.67		
Blades Extend to r/R = 0.33		
	SIA (cm^2/cm^3)	
	r/R = 0.42	r/R = 0.68
500 rpm & 12.5 L/min	1.79	0.52
500 rpm & 8.7 L/min	1.68	0.49
500 rpm & 4.4 L/min	1.14	0.40
750 rpm & 8.7 L/min	3.86	1.13

From the above figures, increasing the impeller speed creates higher SIA, and – as expected – increasing the gas flow rate at constant impeller speed increases the SIA. In all instances, much higher SIAs are found in the impeller discharge plane – for example, in the dispersed recirculation regime, the SIA near the impeller is almost an order of magnitude larger than in other regions in the ST. In the discharge stream as the location moves further away from the impeller and closer to the wall, the SIA quickly drops down near the average values found in the rest of the reactor. Since mass transfer is dependent on SIA, this vast difference in SIA creates regions of varying mass transfer (and hence reaction) rates.

4.5.1.4 Velocity Distribution

Bubble velocities, let alone bubble velocity distributions, in opaque STs are simply not reported in the literature. Only photography and the laser techniques have been used (Montante et al, 2008; Deen, 2001; and Morud & Hjertager, 1996), but those techniques can only be used in a transparent fluid and ST at the wall or at low gas holdups and available data is still scarce. Using those techniques, gas velocities in the impeller discharge stream are often reported normalized to the impeller tip speed (shown in Figure 4.46).
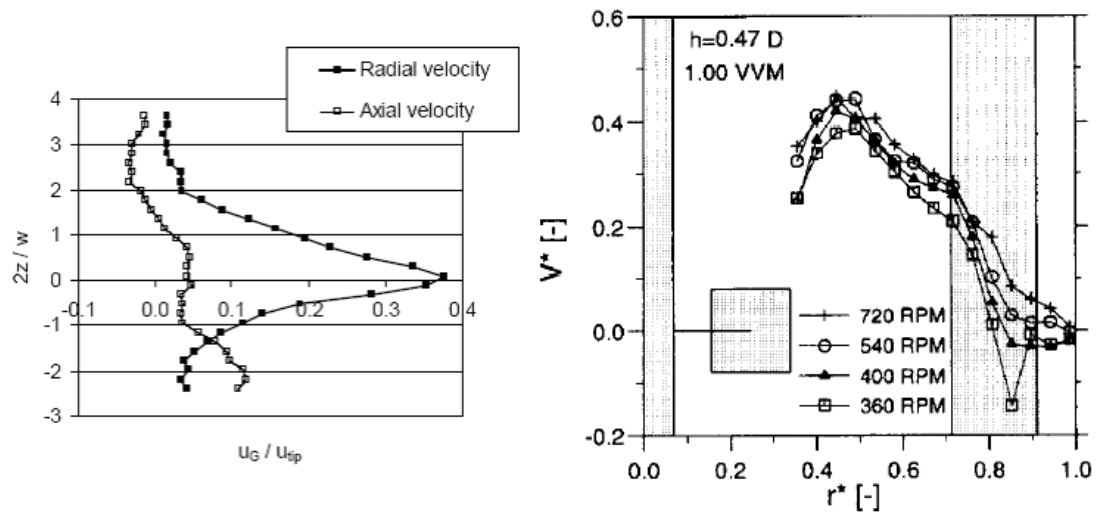
Figure 4.46: Mean radial gas velocities in impeller discharge stream (Source: Deen, 2001 - left and Morud and Hjertager, 1996 - right)

The ST (22 cm ID with a dished bottom) used by Morud and Hjertager (1996) is fairly close to the ST used in this work. In this study, the results obtained in the impeller discharge stream obtained by the 4-point mini-probe match very well with the expected trends although the vessel and operating conditions are not exactly the same – see Figure 4.47 below (Note that 1 vvm = 7.5 L/min and 0.49 vvm = 5.625 L/min). At the conditions in this work, the impeller tip speeds are 262, 175, and 122 cm/s at 750, 500, and 350 rpm respectively.
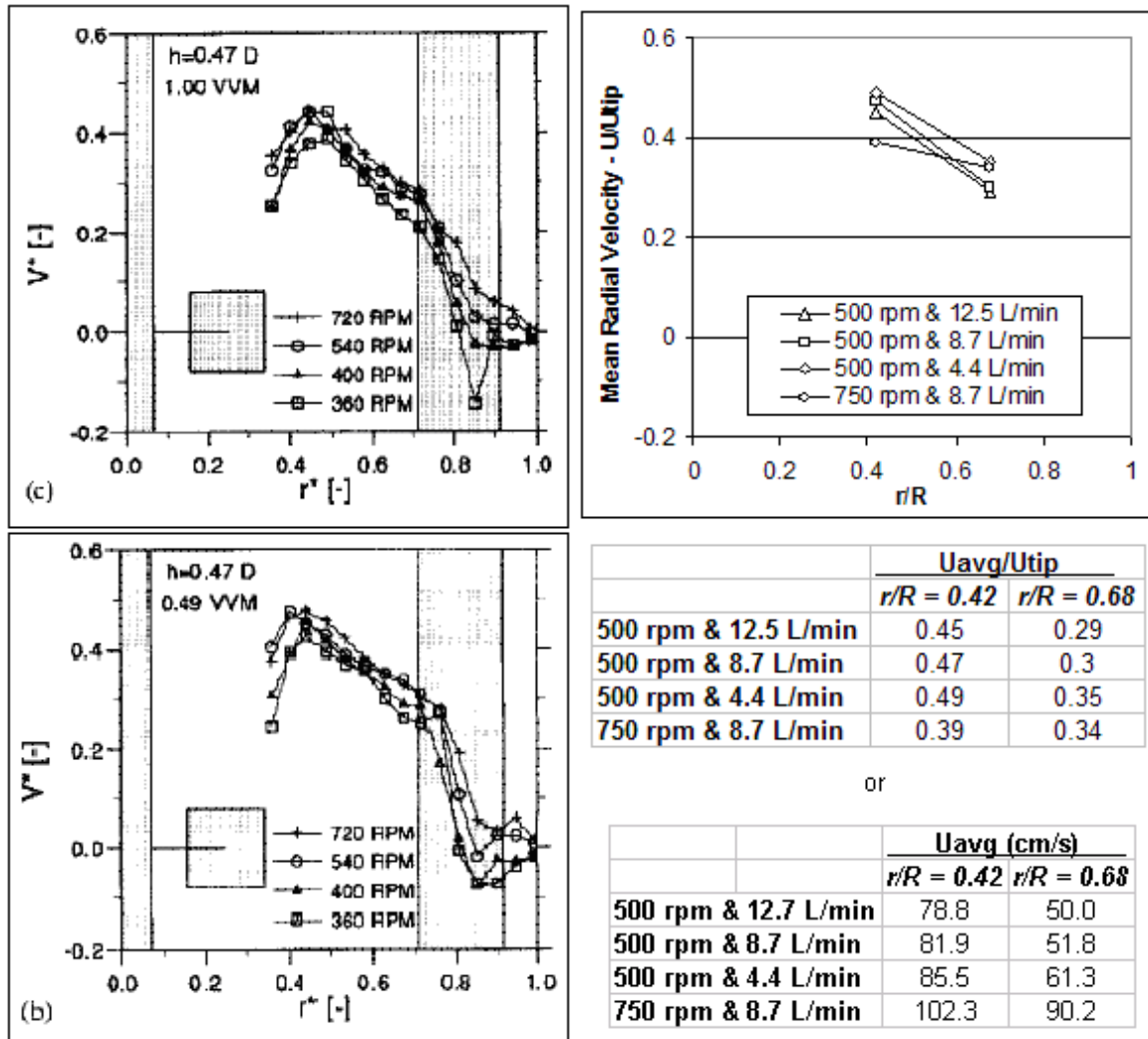
Figure 4.47: Qualitative comparison of mean radial velocity in the impeller discharge stream (results of Morud and Hjertager, 1996 on left & results of this study on the right)

The right side of the figure contains the following tables:

	Uavg/Utip	
	r/R = 0.42	r/R = 0.68
500 rpm & 12.5 L/min	0.45	0.29
500 rpm & 8.7 L/min	0.47	0.3
500 rpm & 4.4 L/min	0.49	0.35
750 rpm & 8.7 L/min	0.39	0.34

or

	Uavg (cm/s)	
	r/R = 0.42	r/R = 0.68
500 rpm & 12.7 L/min	78.8	50.0
500 rpm & 8.7 L/min	81.9	51.8
500 rpm & 4.4 L/min	85.5	61.3
750 rpm & 8.7 L/min	102.3	90.2

In the impeller discharge stream, the mean radial bubble velocity drops with increasing distance from the impeller. Increasing the gas flow rate decreases the mean bubble velocity. And, increasing impeller speed increases the mean velocity (although not when normalized with the impeller tip speed). Yet, as with the mean bubble size, the mean velocity does not tell the entire story. The velocity distributions in the impeller discharge stream (shown in Figure 4.48) mostly follow a normal distribution that ranges

85

from close to zero up to near the impeller tip speed. As the impeller speed increases the velocity distribution begins to shift away from the impeller tip speed and more low velocities are observed.
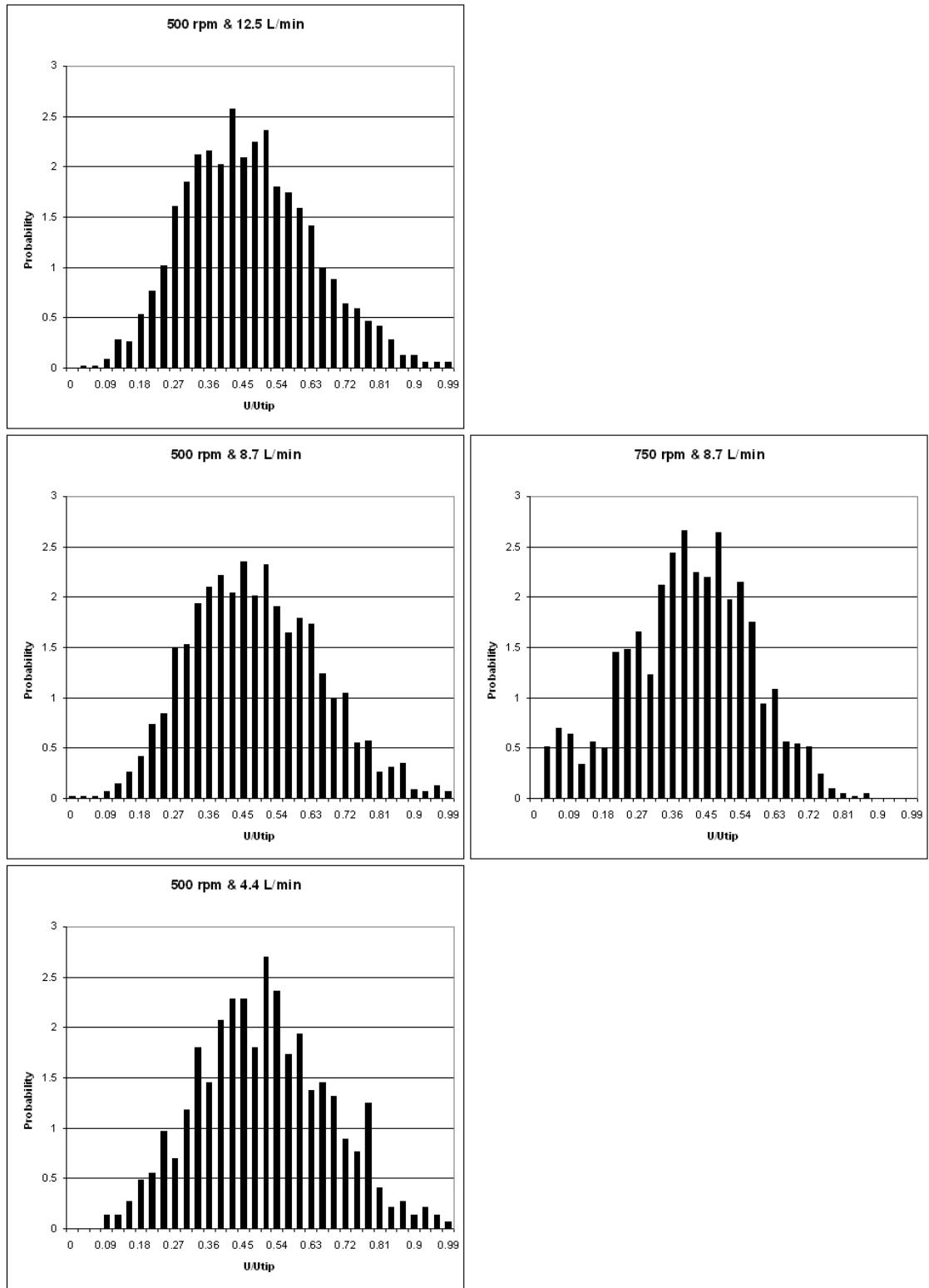
Figure 4.48: Bubble velocity distributions in the impeller discharge stream at r/R = 0.42

The change in the mean radial velocity distribution in the impeller stream becomes more evident as the distance from the impeller tip increases (see Figure 4.49 below). The range of the velocity distribution narrows and shifts to lower velocities.
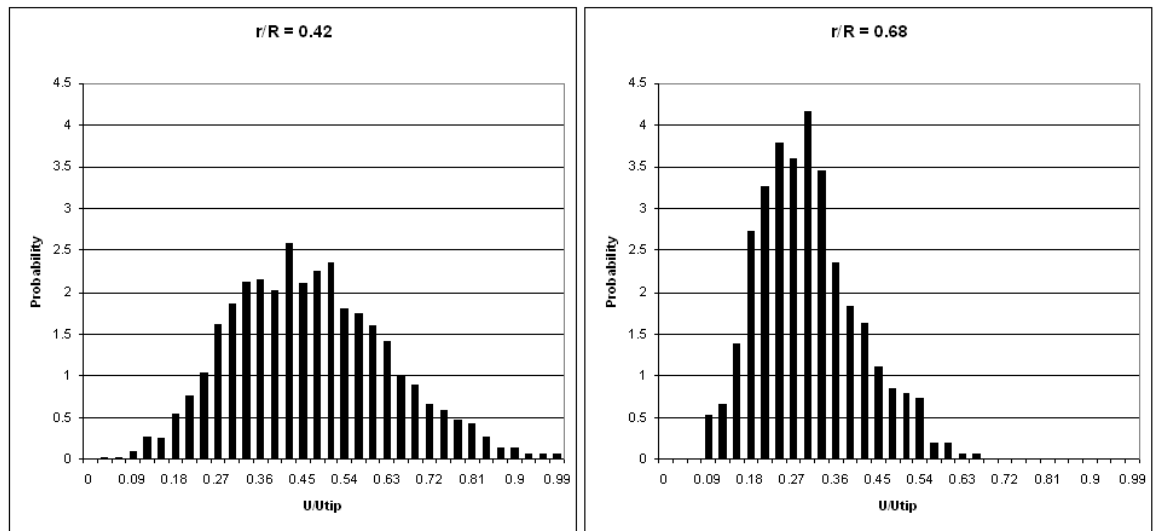
Figure 4.49: Change in mean radial velocity distribution with distance at 500 rpm and 12.5 L/min

Shown below in Figure 4.50 are the normalized mean axial velocities in the $z/H = 0.75$ plane.

		U/Utip				
		r/R				
		0.14	0.3	0.5	0.7	0.88
500 rpm & 12.5 L/min		0.14	0.14	0.14	0.14	0.17
500 rpm & 8.7 L/min		0.12	0.13	0.13	0.15	0.19
500 rpm & 4.4 L/min		0.10	0.11	0.12	0.15	0.21
750 rpm & 8.7 L/min		0.07	0.08	0.09	0.11	0.15
500 rpm & 8.7 L/min		r/R				
	Angle	0.14	0.3	0.5	0.7	0.88
	77.3	na	0.14	0.16	0.14	0.17
	64.1	na	na	0.15	0.15	0.18
	45.0	0.12	0.13	0.13	0.15	0.19
	25.9	na	na	0.14	0.16	0.19
	12.7	na	0.13	0.15	0.18	0.22

Figure 4.50: Mean axial velocities in the $z/H = 0.75$ plane

Note that in each instance the mean axial bubble velocity decreases moving away from the wall, that for $r/R > 0.6$ the velocity decreases with increasing gas flow rate, and for $r/R < 0.6$ the velocity increases with increasing gas flow rate. This agrees with the expected flow field from a radially discharging impeller and with visual observation. High velocity bubbles generated at the impeller move radially outward toward the wall and then flow upward as they rise toward the free liquid surface. As the bubbles flow upward, they also curl away from the wall. At the $z/H = 0.75$ elevation, lower axial velocities (the vertical component of the velocity vector) would be expected further from the wall since bubbles in this region are not moving mostly upward (as they are near the wall). Thus, while the magnitude of the velocity of a bubble near the impeller shaft may be the same as that of a bubble near the wall, the direction of the velocity of a bubble near the impeller shaft is very different than that of a bubble near the wall.

While increasing the impeller speed generates higher velocities in the vessel, the normalized axial velocities are actually lower in the dispersed regime with recirculation. This is direct result of the pumping efficiency of the radial impeller. For $r/R > 0.6$, the mean axial bubble velocity significantly depends on angular location and increases moving away from the windward baffle toward the leeward baffle – a result of the gas accumulation near the leeward baffle. In the $z/H = 0.5$ plane, the trend of decreasing axial velocities moving away from the wall continues, but tangential effects on axial velocity are negligible (Figure 4.51).

500 rpm & 8.7 L/min		U/Utip	
z/H = 0.75		r/R	
	Angle	0.7	0.88
	77.3	0.14	0.17
	64.1	0.15	0.18
	45.0	0.15	0.19
	25.9	0.16	0.19
	12.7	0.18	0.22
z/H = 0.5			
	Angle	0.7	0.88
	77.3	0.13	0.18
	64.1	0.13	0.20
	45.0	0.13	0.20
	25.9	0.13	0.21
	12.7	0.13	0.20

Figure 4.51: Change in axial velocities near the wall above the impeller discharge plane

Note that the velocity decreases with height at $r/R = 0.88$ and increases with height at $r/R = 0.7$ – this flip can be attributed to the flow pattern of bubbles curling away from the wall as they rise. The flip occurs in all the dispersed regimes and occurs at smaller r/R values as the gas flow rate increases (between $0.5 < r/R < 0.7$ at the highest gas flow rate).

It must also be noted that the flow is not necessarily in one direction as periodic flow changes can occur within a ST. In regions outside the impeller discharge stream, it is possible that bubbles can move upward in one instance and then downward in another instance at a certain point in space. Take, for instance, the axial velocity distribution at r/R and $z/H = 0.5$ in the dispersed regime with recirculation (Figure 4.52).

90
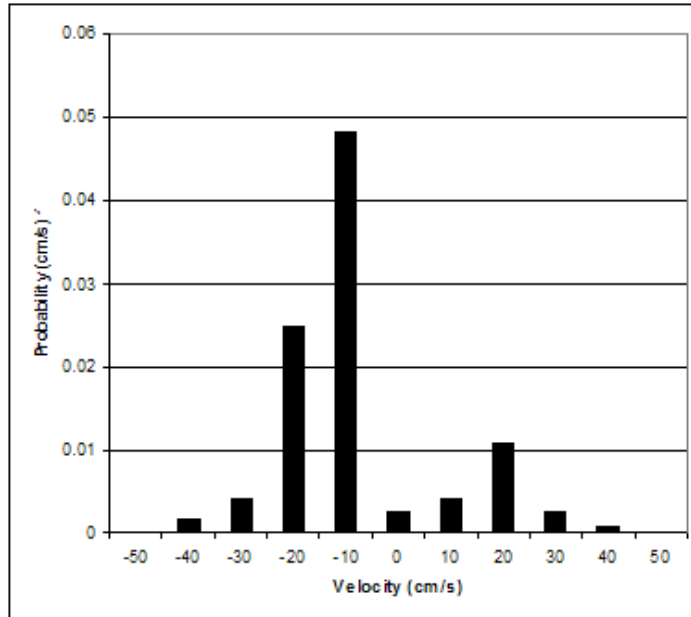
Figure 4.52: Complex axial velocity distribution at 750 rpm and 8.7 L/min

As described in Chapter 3.1.1, the 4-point mini-probe yields the magnitude and direction of the velocity of each bubble it detects; however, it is the scalar velocities in STs (axial, radial, and tangential) that are reported in the literature and used for comparison in CFD modeling. To properly capture all three components of velocity, six probe orientations (imagine one for each of the 6 faces of an infinitesimally small cube – shown below in Figure 4.53) can be used to characterize the scalar velocity field at a point.
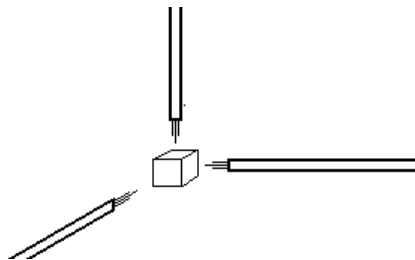
Figure 4.53: Sampling a local point in an unknown flow field

If however, the flow field is generally known – for example bubbles move outward in from the impeller to the wall in the impeller discharge stream – then the number of probe orientations required can be reduced.

4.6   Conclusions

The new 4-point mini-probe has been demonstrated to accurately describe complex, 3-D bubble dynamics (gas holdup, chord lengths, interfacial area, and velocity) in a ST. The probe can measure the spectrum of bubble dynamics of a bubble 0.85 mm and larger – an implementation of borescopy confirms this. Single point probes can be used to capture gas holdup of an even smaller bubble size, but two point probes cannot be used in a multiphase ST due to the complex 3-D nature of the flow. Probe orientation for the single point and 4-point probe (in light of a simple picture of the flow field) must be taken into account in order to quantitatively describe bubble dynamics.

In a ST equipped with a radially discharging impeller, multiple probe orientations are required to describe all regions of the vessel. Two opposing probe orientations (commonly upward and downward) will properly quantify gas holdup in any region of the reactor. The determination of bubble chord lengths and interfacial area require enough statistical sampling (a large enough interaction with bubbles) – it was found that three orientations (upward and downward outside of the impeller discharge stream and pointing toward the impeller inside the discharge stream) properly quantify bubble chord lengths and interfacial areas. Depending on the location in the ST, up to 6

orientations can be used to quantify the scalar bubble velocity fields in the radial, axial, and tangential directions.

In this work and in Mueller et al. (2007), demonstration of the single-point probe at high pressures has laid the foundation for the creation of a 4-point mini-probe using aluminum-coated fibers that can withstand high pressure and high temperature conditions (175 barg and 400°C). (Note that a 7-fiber reflectance probe using aluminum-coated fibers is presented later in Chapter 6).

The bubble chord length and velocity distributions from the 4-point mini-probe provide a much better description of the complex flow in a ST than solely mean velocities or Sauter mean diameters.

Thus, a tool and a methodology have been developed for the quantification of bubble dynamics in G-L STs that can be applied to any type of G-L reactor. This tool can now be used to 1) describe flow fields in opaque reactors that were previously unable or difficult to visualize – especially at higher temperatures and pressures, 2) improve and verify CFD for the modeling, design and scale-up of in G-L reactors, 3) can be used as on online, in-situ process control method to ensure the proper operating conditions are achieved in a vessel.

Chapter 5

Liquid Level Detection and Volumetric Expansion of CXLs

A fiber-optic probe is developed for the fast, in-situ measurement of volumetric expansion of multiphase and multicomponent systems. An experiment with the binary mixtures of CO_2-toluene and CO_2-ethanol was conducted to demonstrate the usefulness of the fiber-optic probe in accurately tracking the isothermal volumetric expansion as a function of pressure. In the 1-L autoclave that has been used, the probe was shown to detect the liquid level height within a precision of 0.35% of the total height of the vessel. The results for the volumetric expansion of toluene and ethanol with CO_2 correlate well with those found in the literature. The probe itself can be used up to pressures of 120 barg and temperatures of 120 °C.

5.1 Introduction to CXLs

Supercritical fluids have been the focus of many studies in green engineering. Dense-phase carbon dioxide has received much attention because of its environmental and economic benefits, such as replacement of harsh solvents, enhanced product selectivities, ease of product separation, and pressure tunability (Gordon et al., 2004; Subramaniam et al., 2002; and Wei et al., 2002). To utilize these benefits efficiently in

dense-phase reactors, a detailed knowledge of the phase behavior of multicomponent and multiphase systems is needed. The magnitude of the volumetric expansion of solvents with CO_2 is important to many industrial applications, such as catalytic reactions and the gas-antisolvent process (Musie et al., 2001; Jin et al., 2004; Gallagher et al., 1989; and de la Fuente et al., 2000) While many equations of state, such as the Peng-Robinson equation (Peng & Robinson, 1976), are able to estimate fluid properties at high pressure, they require empirical mixing rules that must be optimized using experimental data. On the experimental front, the most commonly applied methods for the measurement of volumetric expansion are densitometry (coupled with sampling – Kordikowski et al., 1995; and Chang & Randolph, 1990) or the use of some type of view cell (Wei et al., 2002; Jin et al., 2004; Chang & Randolph, 1990; Lazzaroni et al., 2005; and Houndonougbgo et al., 2006) such as a Jerguson cell, that is separate from the reactor. These measurements can be expensive and time-intensive.

A simple, fiber-optic probe is presented for the fast, in-situ and direct measurement of volumetric expansion within a high-pressure vessel.

5.2 Experimental

5.2.1   Materials

High-performance liquid chromatography (HPLC)-grade toluene and ethanol (Fischer Scientific) and liquid CO_2 (CeeKay) were used for the expansion experiments.

5.2.2 Apparatus

The experimental setup is shown below in Figure 5.1.
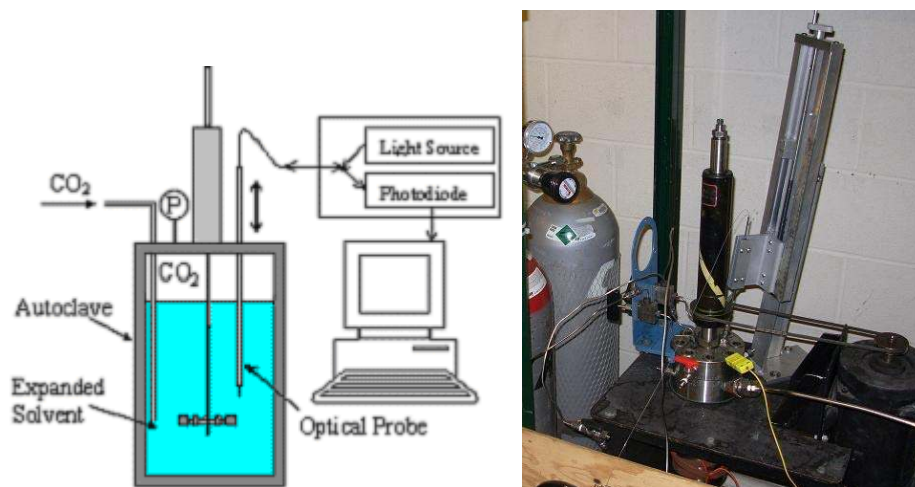
Figure 5.1: Experimental setup, fiber-optic probe and actuating arm

An HPLC pump (Waters 515) delivers CO_2 to the 1-liter autoclave (Autoclave Engineers). Pressure was controlled via a Tescom 4000 back-pressure regulator and Validyne pressure transducers. Temperature control was achieved using Omegalux heating tape wrapped around the autoclave, an Omega thermocouple inserted into the vessel's thermowell, and an Omega CN132 temperature controller.

5.2.3 The Single-Point, Fiber-Optic Probe

The refractive indices of gases are vastly different from liquids; therefore, gas/liquid boundaries can be readily determined. As an example, the probe response to a bubble striking the probe tip is shown schematically in Figure 5.2.
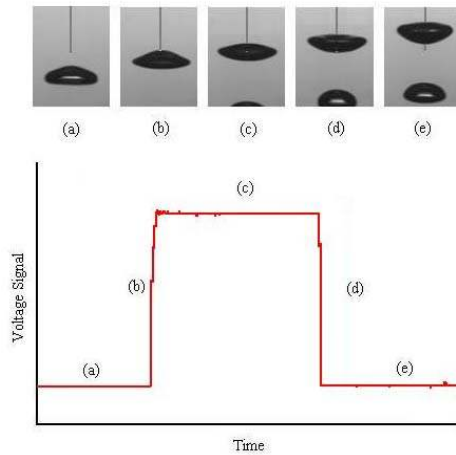
Figure 5.2: Characteristic step response of a bubble striking the probe tip. (a) and (e) show the probe response in the liquid, (c) the response in the gas, and (b) and (d) the response of the tip entering and leaving gas/liquid interface

Figure 5.3 below shows a light source that sends a single wavelength of light (670 nm) to the probe. Depending upon the environment surrounding the probe tip, a percentage of the emitted light is reflected back through the fiber. The fiber-optic coupler sends the reflected light to a photodiode, which converts the quanta of light into a voltage signal for processing.
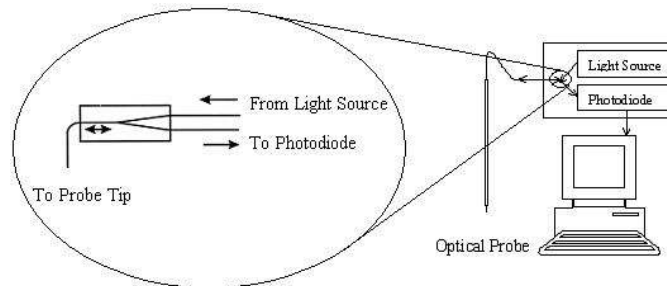
Figure 5.3: Fiber-optic coupling (Source: Xue, 2004)

Depending upon the environment the surrounding the probe tip, a percentage of the emitted light is reflected back through the fiber. The fiber optic coupler sends the

reflected light to a photodiode, which converts the quanta of light into a voltage signal for processing.

Figure 5.4 shows that the fiber-optic probe consists of a 200 micron multimode fiber (Thorlabs), which is glued inside of 1/8-in. stainless steel tubing using a high-pressure/temperature epoxy.
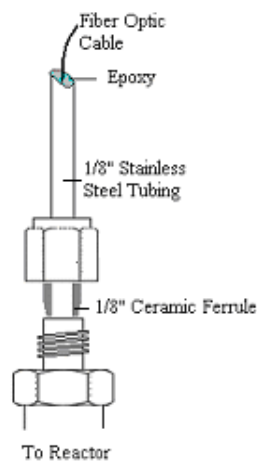
Figure 5.4: Probe insertion into autoclave

The probe is sealed into the autoclave using a ceramic ferrule; because the ferrule does not swage onto the metal tubing, the probe can be moved vertically through the autoclave under high pressure without any leaks. To prevent the probe from blowing out of the autoclave, the probe is clamped into an actuating arm that controls the vertical movement.

5.2.4 Experimental Method for the Determination of Volumetric Expansion

To measure volumetric expansion, a known quantity of solvent is placed in the autoclave at atmospheric pressure. Any air in the system is then purged by flushing the reactor with CO_2, and the system is brought to a constant temperature for the entire experiment. After the system reaches the desired temperature and the pressure in the reactor is 1 bar, a reading of the initial liquid level height in the vessel is recorded. (Note: The liquid in the autoclave is not stirred during the expansion measurements but is stirred during the time between measurements.) Next, the CO_2 pressure is increased, which causes the liquid phase to expand as a result of further dissolution of CO_2 into the liquid phase. As the liquid level in the autoclave begins to rise with increasing pressure, the probe is moved vertically through the autoclave to determine the location of the liquid level. The probe-detected position of the gas-liquid interface (hence, the liquid volume), as a function of pressure, is then recorded to determine the percent isothermal volumetric expansion (VE) as:

$$VE = \frac{V_{exp,T_0} - V_{0,T_0}}{V_{0,T_0}} * 100 \qquad (11)$$

where the initial condition (V_0, T_0) is the volume of the liquid in the vessel at a 1 bar of CO_2 and temperature T_0.

5.2.5 Experimental Uncertainty in Volume, Pressure, and Temperature (V,P,T) Measurements

The probe was shown to detect the liquid level height within a precision of 0.35% of the total height of the vessel. This introduces an error no greater than +/-3.56 mL in any volume reading. Volume measurements in the vessel were calibrated in 50 mL increments, as shown in Figure 5.5.

Calibration of Volume Measurements Using the Probe

$$y = 114.01x - 150.94$$
$$R^2 = 1.00$$
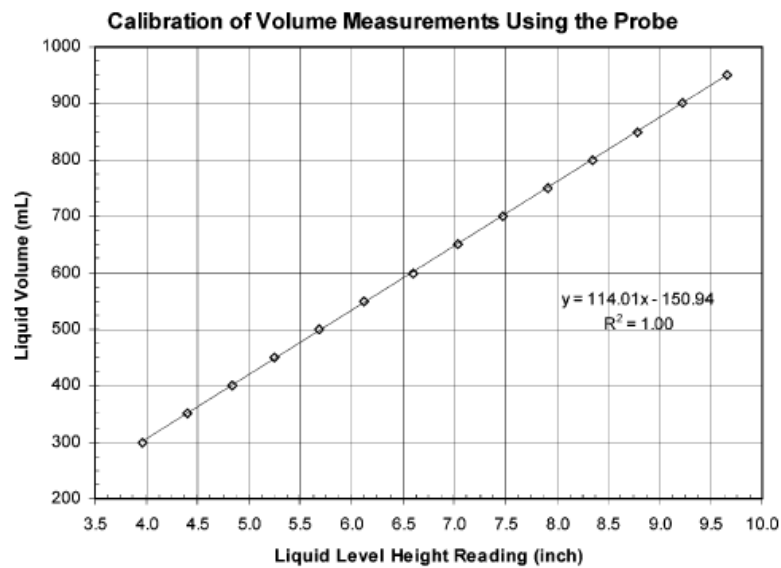
Figure 5.5: Height-to-volume calibration

Knowing this uncertainty in the volume determination, the error in the volumetric expansion readings, as defined in section 5.2.4, is shown in Figure 5.6.
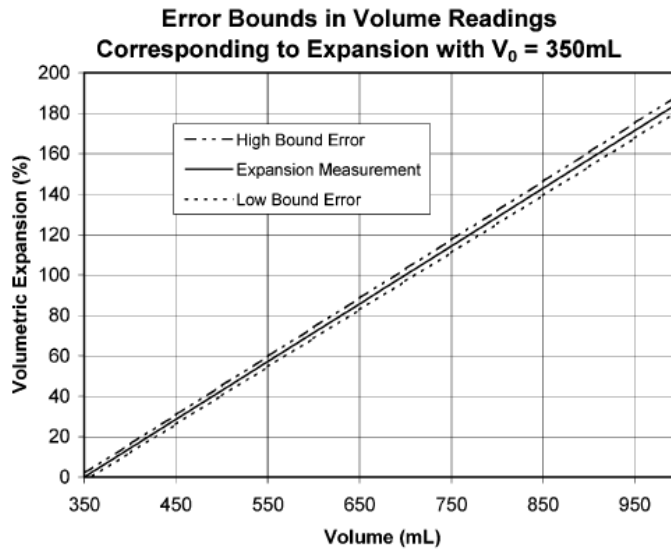
Figure 5.6: Error in expansion measurements due to volume

With V_0, T_0 typically being near 350 mL, the error in the expansion measurements (in units of %) increases from +/-2.2% at smaller volumes to +/-3.8% at full volume (1000 mL). Thus, at larger pressures (larger V, compared to V_0), the uncertainty in the measurement would be greater than that at lower pressures.

Pressure measurements were taken with a transducer with a range of 0-220.63 barg at a span of 0-10 V. Therefore, we ideally expect an increase of 0.3125 V for every 6.89 barg. It was determined that the actual voltage reading is within +/-0.03 V of the ideal reading, which is a difference of ~0.69 barg. Therefore, one can assume that the pressure measurements could deviate by as much as +/-0.7 barg.

Temperature was monitored in the vessel using a thermocouple that was calibrated against two different mercury thermometers at temperatures in the range of 20-50 °C. It

was determined that the thermocouple never deviated from the mercury thermometers more than +/-0.4 °C. Because the autoclave was insulated and well-mixed between readings, it is assumed that the temperature throughout the vessel is constant.

5.3 Results and Discussion

To demonstrate the usefulness of the optical probe, toluene was isothermally expanded with CO_2 at multiple temperatures; the results are shown in Figure 5.7.
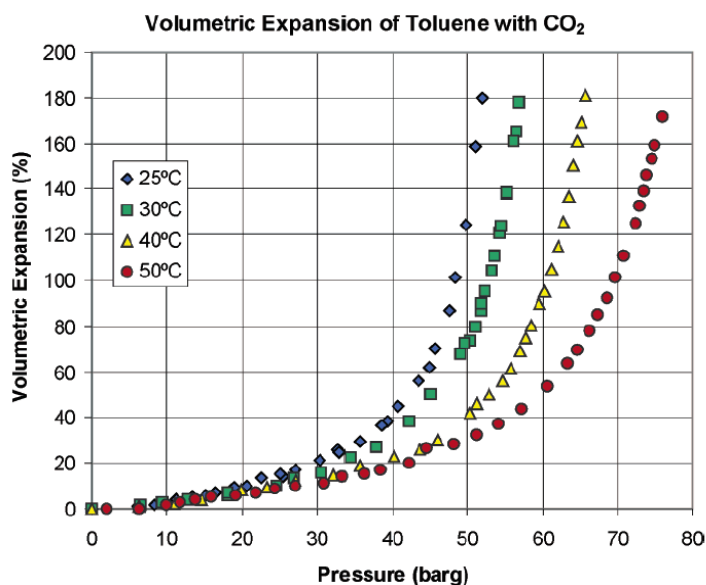
Figure 5.7: Volumetric expansion of toluene with CO_2 as a function of pressure

A sharp increase in isothermal expansion is observed as the pressure increases and more and more CO_2 diffuses into the liquid phase. Also, note that isobaric volumetric expansion decreases as the temperature increases. The data for toluene at 25 and 40 °C are compared with the literature values in Figure 5.8.
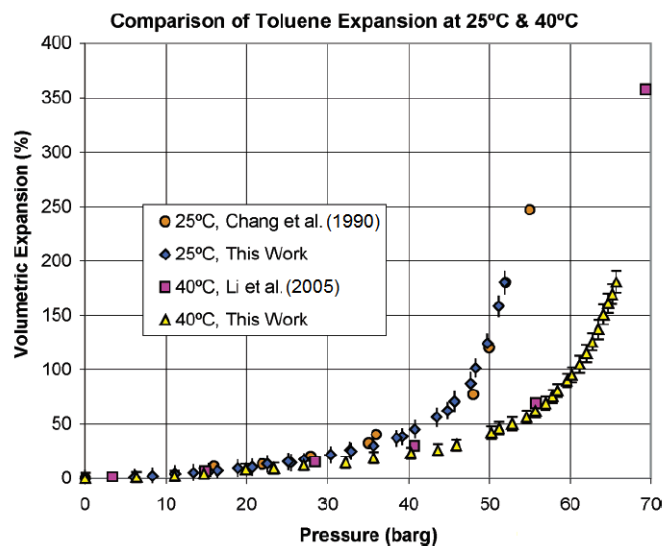
Figure 5.8: Comparison of toluene expansion with CO_2 from different studies

For toluene, it is evident that the data obtained using the fiber-optic probe agrees well with the results reported in the literature (Chang & Randolph, 1990; and Li et al., 2005) Our results for ethanol expansion with CO_2 are compared to other literature results in Figure 5.9.
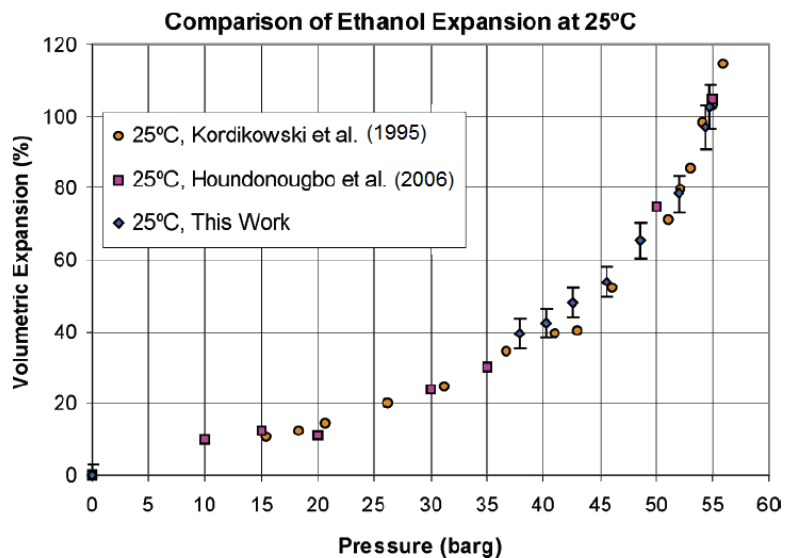
Figure 5.9: Comparison of ethanol expansion with CO_2 from different studies

Note that three different methods for determining volumetric expansion are compared: densitometry coupled with sampling (Kordikowski et al., 1995), visual measurement by the use of a view cell (Houndonougbo et al., 2006), and our fiber-optic probe technique. Results of all three techniques agree well with each other.

5.4 Conclusions

The experiments with CO_2-toluene and CO_2-ethanol illustrate that the dynamic fiber-optic probe is a simple, fast tool for quantifying the volumetric expansion of solvents in a high-pressure vessel that requires no view window or sampling. Because the probe simply designates whether it is in the presence of a liquid or gas, no complex calibration is required. The probe is relatively inexpensive and can be used to quickly determine the in situ volumetric expansion in complex systems with multiple components and multiple phases with reasonable accuracy. This technique may also be used to simply determine the liquid level in a reactor.

Note that many other organic solvents were also investigated: methanol, ethyl acetate, acetone, acetonitrile, 1-octene, nonanal and cyclohexane. These expansions are available in Appendix B.1.

Chapter 6

Critical Phase Changes in CXLs

Two types of fiber-optic probes, a densitometer and a critical opalescence probe, are developed for the in-situ measurement of the phase change of single and multicomponent systems from the subcritical to the supercritical states. Experiments with pure CO_2 and binary CO_2-decane and CO_2-methanol were conducted to demonstrate the ability of the fiber-optic probes in accurately monitoring the critical phase change. The probes were used up to pressures of 200 barg and temperatures of 250 °C.

6.1 Introduction to Critical Phase Changes

The benefits of CXLs and their limitations have been outlined in Chapter 5.1. The determination of the phase transition of a CXL from a heterogeneous, gas-liquid system to a homogeneous supercritical state is of the utmost importance when it comes to in-situ catalyst separation. Most critical phase boundaries for fluids and fluid mixtures can only be predicted for single and binary mixtures. When it comes to multicomponent mixtures, critical phase boundaries are only determined empirically. Depending on the fluids, these phase boundaries can become quite complex (shown in Figure 6.1).
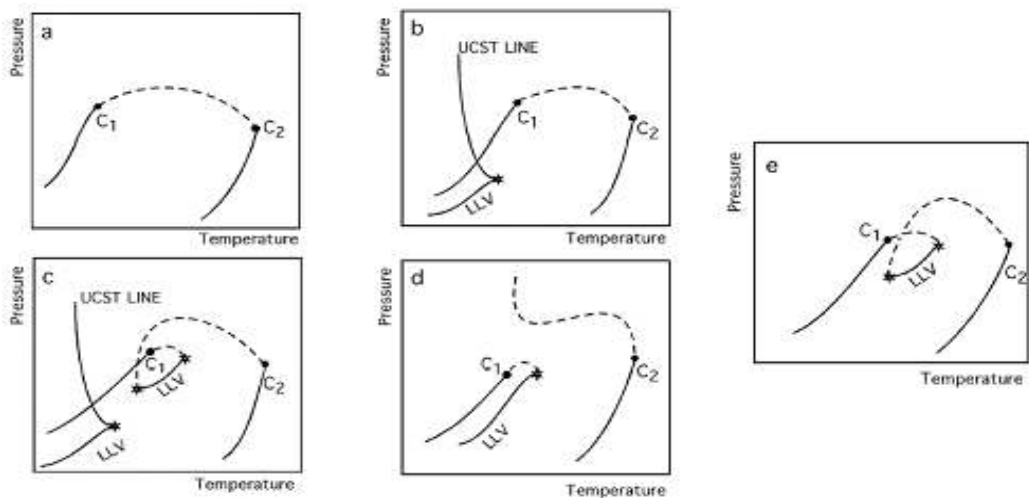
Figure 6.1: Various types of critical phase boundaries

Experimentally, the most commonly applied methods for the determination of phase transition are either view cells or gas chromatography, such as in Brunner et al. (1987). However, the current methods are not in-situ techniques.

A multi-fiber, fiber-optic reflectance probe is presented for the in-situ determination of critical phase boundaries of fluids within a high-pressure vessel.

6.2   Experimental

6.2.1   Materials

High-performance liquid chromatography (HPLC)-grade methanol and decane (Fischer Scientific) and liquid CO_2 (CeeKay) were used for the phase transition experiments.

6.2.2   Apparatus

The experimental setup is exactly the same as in Chapter 5.2.2 with the exception of the critical opalescence probe outlined in the following section, 6.2.3.

6.2.3   The Phase Transition Fiber-Optic Probes

The same densitometry probe used in Chapter 5.2.3 is used to detect the critical phase transition. However, a critical opalescence probe (COP), depicted on the right-hand side of Figure 6.2, is also used to detect critical phase transitions due to the inefficacy of the densitometry probe. The COP has one centralized light emitting fiber surrounded by six, hexagonally-packed receiving fibers. The COP operates on the basis that it can not only sense bubble strikes (similar to the densitometer) but also can sense the light scattering events that occur during phase transition as shown on the left-hand side in Figure 6.2. As the fluid in the reactor begins to scatter light (opalesce) at the critical boundary of the fluid, the intensity of light detected by the six surrounding fibers should begin to increase.
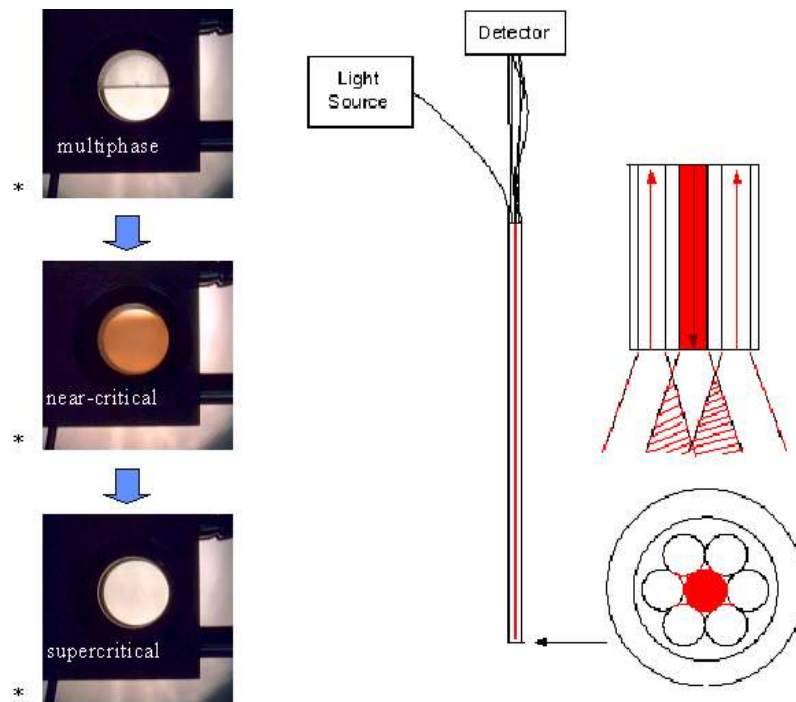
Figure 6.2: The critical opalescence probe/reflectometer (*Source: University of Leeds)

6.2.4 Experimental Methods for the Determination of Phase Change

For the densitometry probe, proposed by Xue (2004), the detection of phase transition depends solely on the ability of a stationary probe to detect the presence or absence of bubbles in the system (shown in Figure 6.3).
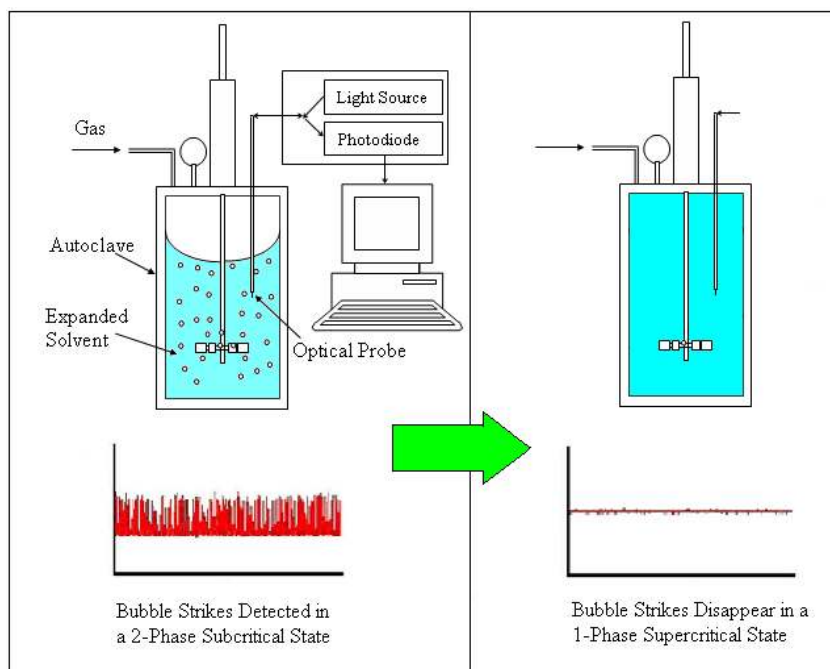
Figure 6.3: Phase change to the supercritical state as detected by densitometry

As will be seen shortly in Chapter 6.3, the densitometry approach has two limitations that prohibit it from being a precise method, such as gas chromatography or the use of a view cell.

The stationary COP can work on the same principle as the densitometry probe, but has the benefit of being able to capture the onset of critical opalescence even if there are no bubbles generated in the system, shown previously in Figure 6.2. At the critical boundary of a fluid, fluctuations between the vapor and liquid states are on the order of the wavelength of visible light causing light to scatter.

6.3 Results and Discussion

The densitometry probe was able to capture phase transition (the disappearance of bubbles) in a system of n-decane/CO_2 (shown below in Figure 6.4), but, from the beginning, two limitations prohibited the precision of the method.
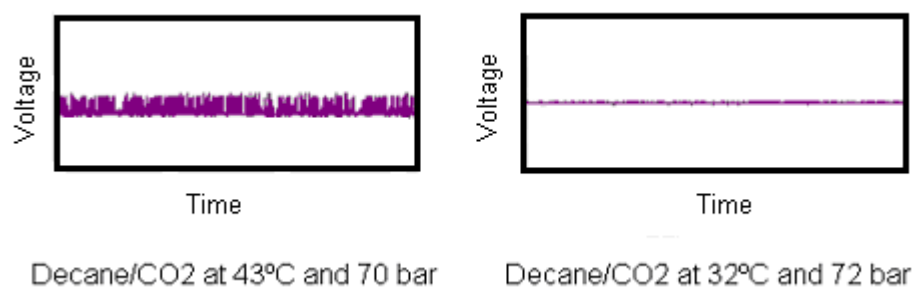
Figure 6.4: Phase transition of n-decane with CO_2 (critical pressure of n-decane = 21.0 bar, critical pressure of CO_2 = 73.8 bar, critical temperature of n-decane = 344.4ºC, and critical temperature of CO_2 = 31.1ºC)

First, as the gas and liquid near the critical boundary of the fluid mixture, their indices of refraction become more and more similar. Thus, the ability of the probe to distinguish between gas and liquid becomes more and more difficult, and even though bubbles may be present in the system, the probe may not be able to sense them. Second, the gas-inducing impeller used in the autoclave generates the bubbles in the system by drawing in gas from the headspace of the reactor and dispersing it through the liquid. If the probe is placed in a position that sees no bubble trajectories or if the gas-inducing impeller is unable to generate bubbles (although there still may be both gas and liquid present in the system), the probe will give a false-positive response. But, this

110

type of detection system can still be used to give a qualitative description of phase transition in high-pressure and high-temperature systems.

Thus, a new approach was taken to at least remove the possibility of a false-positive: the COP. Before beginning with a binary fluid mixture, the first system to be studied was pure CO_2. Two sojourn paths across the critical temperature of CO_2 (2, 4 and 6 in Figure 6.5 below) and across the critical pressure (1, 3, 5 and 6 in Figure 6.5 below) were carried out and the COP response monitored. The system was well mixed before each reading but not aerated with the gas-inducing impeller.

Carbon Dioxide: Temperature - Pressure Diagram
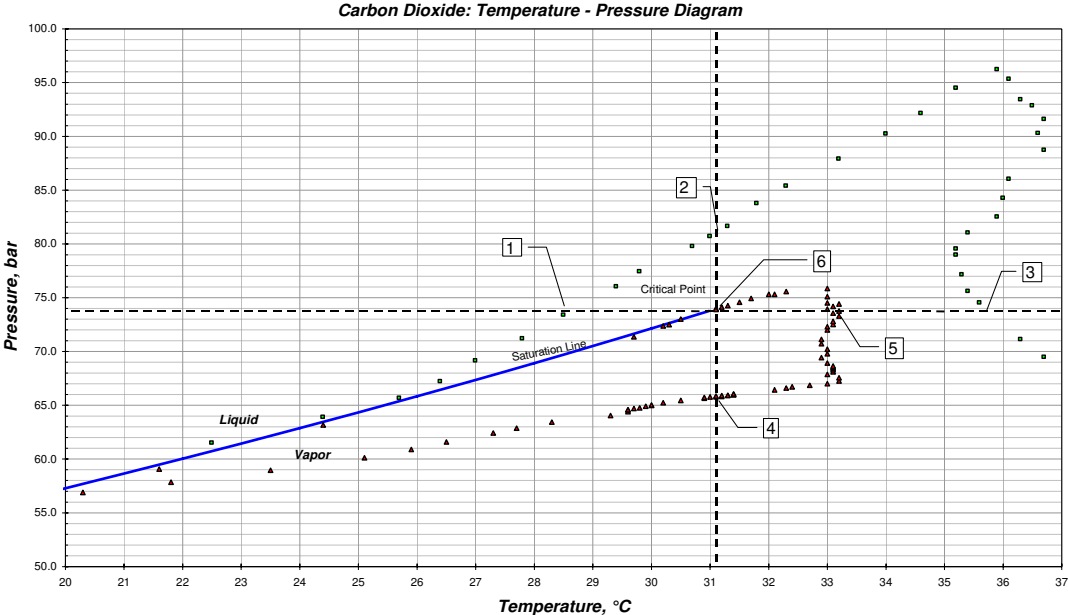
Figure 6.5: Two sojourns in temperature and pressure diagram of pure CO_2

Shown below in Figure 6.6 are the COP responses at positions 1 and 3 in the temperature-pressure diagram for CO_2.
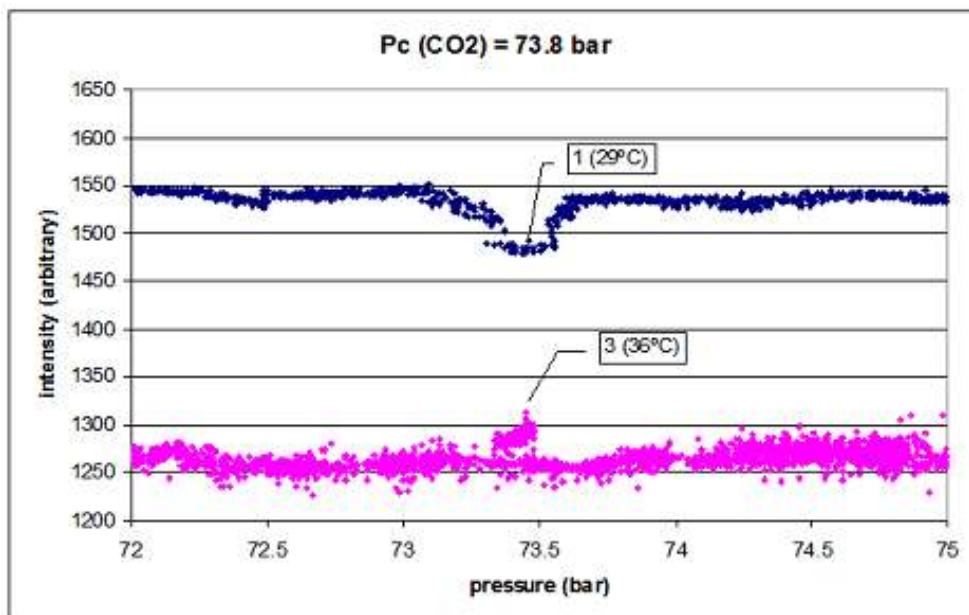
Figure 6.6: COP responses at the critical pressure boundary of CO_2

Note that the COP detects a maximum/minimum in intensity at approximately 73.4 bar when the critical pressure of CO_2 is truly 73.8 bar. Here, the precision of the critical pressure measurement seems to be limited to the temperature/pressure control within the system. Yet, there is no concrete explanation as to why the two intensities for positions 1 and 3 differ.

Shown in Figure 6.7 is the COP response at position 2.
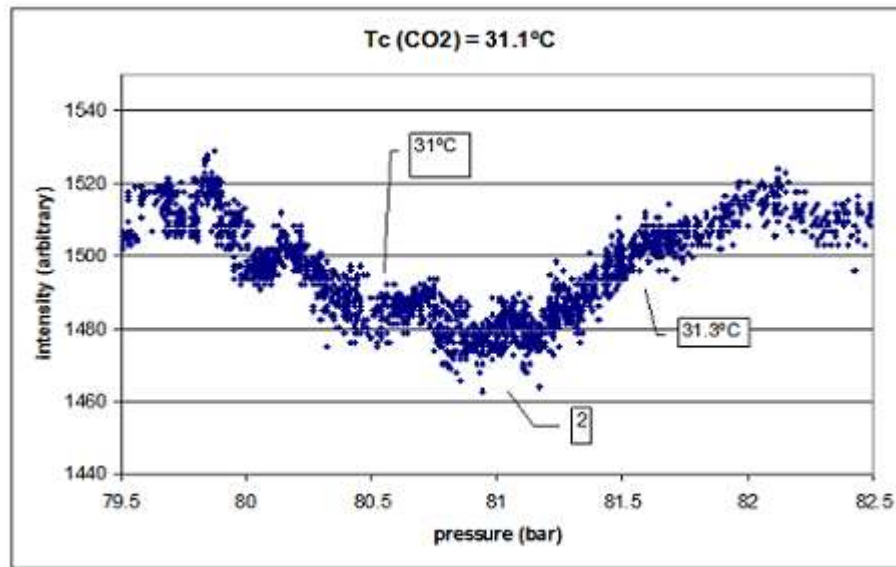
Figure 6.7: COP response at the critical pressure boundary of CO_2

Here the COP detects a minimum in intensity between the temperature of 31 °C and 31.3 °C when the true critical temperature of CO_2 is 31.1 °C. Note that in both Figures 6.6 and 6.7 the signals are actually inverted because the polarity of the light detector was reversed (thus, minimums are actually maximums and vice-a-versa).

At position 4, the superheated vapor state, the COP showed no response. At positions 5 and 6 the critical pressure was found to be approximately 74.5 bar when the true critical pressure of CO_2 is 73.8 bar. Thus, it was determined that the COP could sense the critical temperature and pressure well but that the temperature and pressure measurements in the system limited its precision.

Even with this understanding of the limitations of the precision of the COP, a qualitative experiment with CO_2-methanol was conducted to see how the COP

113

responds in a binary system.   Shown below in Figure 6.8 are the isothermal phase

equilibria for this binary system obtained by Brunner et al. (1987).
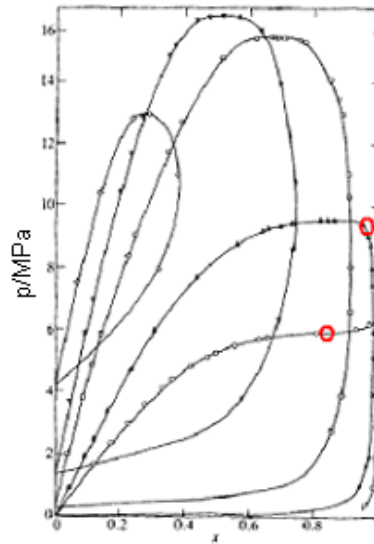
Isothermal phase equilibrium of {xCO2 + (1-x)CH3OH} ○ 298.15 K
323.15 K □ 373.15 K ▽ 423.15 K ◁ 473.15 K

Figure 6.8: Brunner et al.'s (1987) isothermal phase equilibria for CO_2-methanol

Note that at a CO_2 mole fraction of approximately 0.9 in Figure 6.8 the critical pressure

is approximately 60 bar at 25 ºC and 95 bar at 50 ºC.   Below is shown the COP

response at 34 ºC at a CO_2 mole fraction of approximately 0.9.
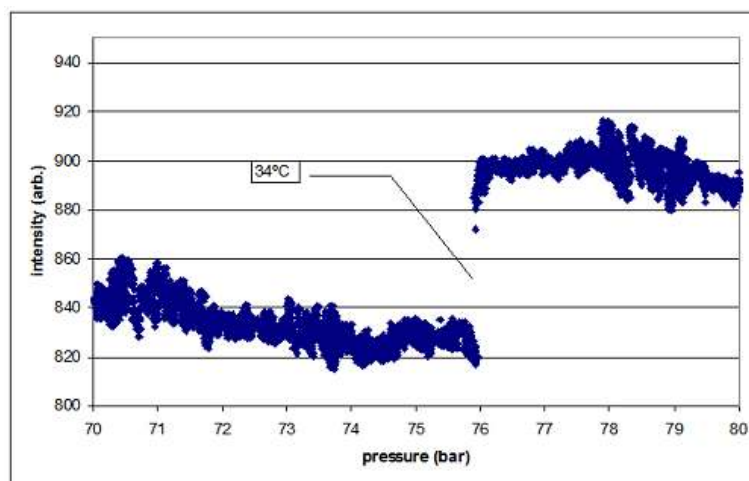
Figure 6.9: COP response for CO_2-methanol at 34 ºC

114

Here the COP detects the critical temperature at 76 bar – within the expected range. The COP also detected the critical pressure of the binary mixture at 96 bar at a temperature of 50 ºC – very close to the expected critical pressure of Brunner et al. (1987). Yet, here again the temperature and pressure measurements (as well as calculating mole fractions instead of measuring them) limits the precision of the technique.

6.4 Conclusions

The experiments with pure CO_2, CO_2-decane, and CO_2-methane illustrate that the densitometry probe has significant limitations that the COP can overcome. Yet, the COP was hindered by the imprecision of the pressure and temperature measurements. Before this technique can compare well with other measurement techniques (where accuracies are to tenths of a degree and pressures within a tenth of a bar), the temperature and pressure control instrumentation need to be upgraded to investigate exactly how precise the COP method for the determination of phase boundaries is. But, in spite of this imprecision the COP technique can be used to simply determine if a phase transition has occurred or not.

Chapter 7

Future Research Ideas

7.1   Effect of Bubbles in Multiphase Electrolytic Reactors

7.1.1   Motivation

Electrolytic reactors, such as fuel cells, are composed of anode and cathode electrodes and an electrolyte solution. By applying a voltage to the electrodes, ions in the electrolyte solution flow from the cathode to the anode. This electrochemical energy then drives the chemical reactions in the solution. Many of the common electrolytic reactions produce gaseous products, such as hydrogen gas in fuel cells. The presence of these bubbles can cause concentration gradients from the bulk electrolyte solution to the surface of the electrode, which in turn affects the rate of reaction and can harm the electrodes. However, since these bubbles are quite small (on the order of tens of microns), many of the research techniques used to investigate bubble sizes are inadequate. If the bubble formation and hydrodynamic flow fields (i.e. bubble dynamics - velocity, size, etc.) of the bubbles from the electrode surface can be quantified, the reactor itself can be properly modeled and better designed.

7.1.2   Proposed Research

Since the bubble size is so small, the number of investigative tools available to a researcher is limited to visual measurement techniques. Thus, if an opaque reactor is to be investigated, the only realistic option is borescopy. Borescopes can be as small as 1/8-in. in diameter and can be inserted into a reactor to capture in-situ images at the micron scale (example shown below in Figure 7.1).
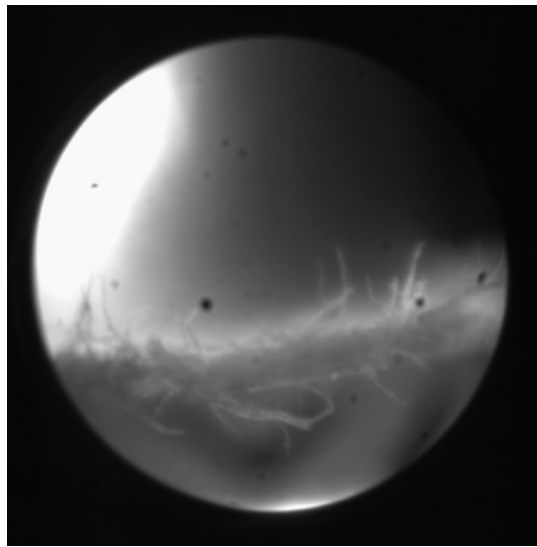
Figure 7.1: The edge of a torn piece of paper (75 μm in width) captured by the borescope (Image obtained using high-speed photography at CREL)

Note that the borescope not only captures the edge of the piece of paper but also the fibrous strands (on the order of 10 μm in diameter) of the torn edge.

When it comes to quantifying the bubble size in these types of multiphase flows, the small size of the bubbles allows for the safe assumption that the bubbles are perfect spheres. This will ease the processing of the acquired high-speed images since bubble geometry is constant. An example of this type of flow can be seen in Figure 7.2.

117
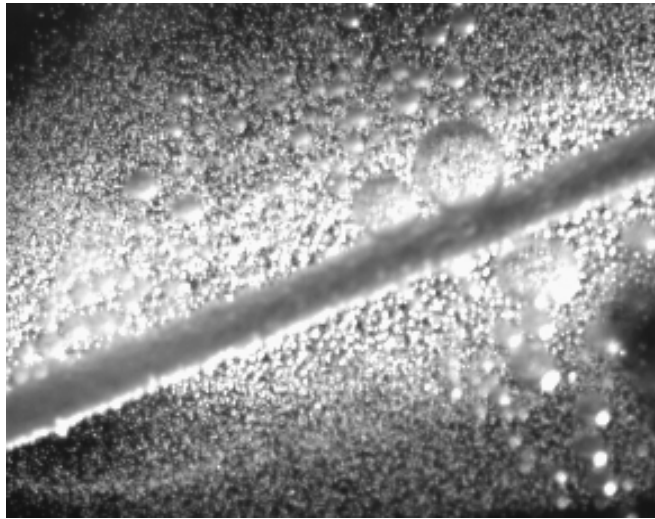
Figure 7.2: H$_2$ bubbles flowing from a 300 μm aluminum fiber in 1 M NaOH solution (Image obtained using high-speed photography at CREL)

The magnification of the borescope can be controlled to view an image area from the order of millimeters (to capture bulk flow – i.e. bubble number, velocity) all the way down to ~ 500 microns (to capture bubble size).

CREL already owns the necessary equipment to capture the imaging (two borescopes and the associated high-speed camera imaging systems); thus, a system of interest needs to be chosen for investigation. There will be need to be a modification to the borescope if the system under investigation is highly alkaline or acidic since these can attack the lens on the end of the borescope. A simple solution to this problem for atmospheric conditions is to use Saran wrap to sheath the borescope from the liquid. By stretching the plastic wrap over the end of the borescope, there is no image distortion by the thin layer of transparent plastic. However, a more rugged and adjustable, windowed sheath could be made that would enhance image capturing by

118

providing a frame of reference for size/velocity measurements (shown below in Figure 7.3).
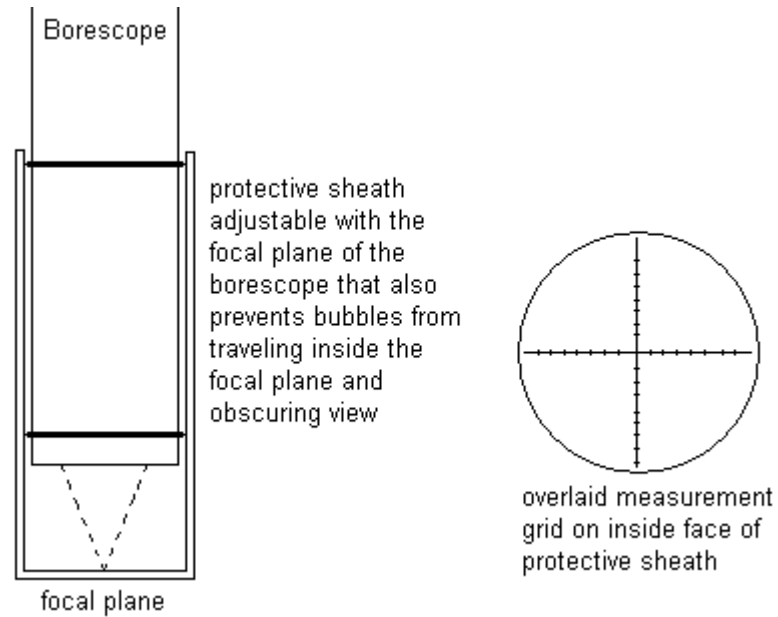
Figure 7.3: Adjustable protective sheath for enhanced image capture with borescopy

Since the borescope already has its own lighting bundled around the lens, this tool would need no other accessories. The gap between the borescope and the sheath can also be filled with index matching gel if reflections (glare) from the sheath become an issue.

7.2 Modeling Flow Regime Changes and Hysteresis in Multiphase STs as Function of Temperature and Pressure

7.2.1 Motivation

The flow pattern of the gas in a ST depends on the relation between the gas flow rate and the impeller rotational speed. Nienow et al. (1977), Bombac et al. (1997) and others have developed correlations for the flooding-loading and loaded-recirculation regime transitions dependant upon the flow number, *Fl*, and the Froude number, *Fr*. However, no one has investigated the effect that pressure and temperature have on these transitions. With the development of high-pressure and high-temperature optical probes outlined in this dissertation, it is now possible to develop a stationary device that can be installed in an opaque reactor that can monitor the flow regime occurring within the reactor. The creation of such a tool would not only allow for the development of correlations to describe how flow regime transitions occur as a function of temperature and pressure but also would provide a means of process control for industrial scale reactors.

There is also an opportunity to investigate the effects of hysteresis on flow regime changes since it is known that there is a time-lag between when the impeller speed and gas flow rate are set and when steady-state operation is achieved.

7.2.2   Proposed Research

By placing a two-channel, single-point, optical probe in a stationary position near the wall of the reactor – for a Rushton impeller, one above the impeller discharge plane and one below the impeller discharge plane – it is possible to quantify the flow regime transitions as depicted in Figure 7.4.
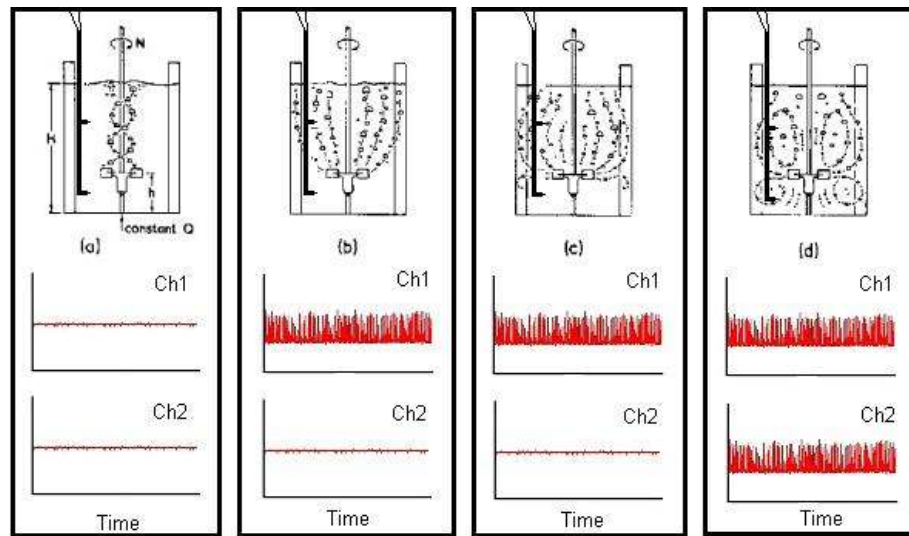
**Figure 7.4: Flow regimes and voltage responses of a 2-channel probe for a radial disk impeller –
a) flooded, b) just dispersed, c) transition, and d) fully developed**

Since the probe is only used to detect the presence of bubbles at the two positions, the two single-point densitometers (the needle-shaped fiber ends) can even be replaced with simple reflection-type detectors (flat-cut fiber ends) that need not project out into the flow. This tool would allow for:

- Quantitative description of flow regime changes as a function of not only gas flow rate and impeller speed but also of temperature and pressure (using the 1-liter autoclave).

- Real-time process control to ensure proper phase dispersion within an opaque industrial reactor.

- Quantitative description of the effects of hysteresis on flow regime transitions (including time lag).

CREL currently has all the material, tools and equipment necessary to produce such a tool and perform the studies.

7.3 Continuation of the Development of the Critical Opalescence Probe

7.3.1 Motivation

There were two limitations that held back further development of the critical opalescence probe during my tenure (both related to cost): 1) the need for a small reactor equipped with precise temperature/pressure control and a view window to allow for visual comparison with the probe results and 2) the need for a highly sensitive light detector to improve the signal to noise ratio. The former would allow for more precise measurements (temperature and pressure-wise) that would allow for better comparison to other measurement techniques. The latter would for a faster determination of the onset of critical opalescence.

7.3.2   Proposed Research

To advance the current state of the critical opalescence probe a small-volume, high-pressure reactor (perhaps 100 mL) equipped with a stirrer (magnetic or mechanical) and high-pressure window would need to be constructed. The smaller scale volume would allow for more precise temperature control, and the view window would allow for comparison between the probe and high-speed photography. The photomultiplier (light detector) used in the previous experiments was rather inexpensive and had a large amount of noise in the signal. A more precise detector would improve the detection of the onset of critical opalescence.

As a side note: the FTIR probe (equipped with a highly sensitive spectrometer that CREL acquired a few years ago) might possibly be able to detect the light scattering event that occurs during critical opalescence. If this is the case, then the Parr reactor that was modified to accommodate the FTIR probe could be used (although it doesn't have a view-window).

7.4   Capture of Bubble Dynamics of Extremely Small Bubbles

7.4.1   Motivation

Densitometry-type probes have limitations on the bubble sizes with which they are able to interact. However, reflectance probes have been used successfully in bubble columns

(Xu et al., 2005) and fluidized beds (Yang et al., 2001, Tayebi et al., 1999 & Werther et al., 1996) to capture holdup or velocities bubbles all the way down to very fine micron level particles. The same principle can be applied in G-L reactors where very small bubbles are expected – for instance, the bubbles from an electrolytic reaction as shown in Figure 7.2.

7.4.2   Proposed Research

With successful completion of the COP outlined in Chapter 7.3. A reflectance-based probe would be in hand that could be used to capture phase holdup and dynamics of very fine bubbles just as fine particles are detected in a fluidized bed. This would require the development of a new processing algorithm.

7.5   Stationary Fiber-Optic Probe for the Determination of Liquid Level and Volumetric Expansion

7.5.1   Motivation

The measurement technique described in Chapter 5 has three requirements:

- An actuating arm must be mounted and aligned on the reactor setup for the movement of the optical probe

- The probe must have a free path of movement within its actuated track in the reactor (no interference from internals)

- Special ceramic ferrules must be used to create a high-pressure seal but still allow probe movement without leaks.

These requirements thus make the implementation of the current technology more difficult on a variety of reactors – the biggest hurdle being the requirement of probe movement. If a probe could be sealed into a reactor and left in place, it would make the technology more accessible for wider use.

7.5.2   Proposed Research

There are two approaches one can take to create a stationary probe. One approach is to bundle 2 to 7 densitometers of different lengths and stagger them within the probe vertically in the reactor. But, the trade-off for this approach is that it can only provide a coarse measurement of the liquid height in vessel since each fiber can only say whether it is in liquid or gas at a specific position. The second approach was stumbled upon while investigating the phase change of a CXL with the critical opalescence probe.

During an experiment with binary CXL (methanol-CO_2) the signal response with the probe in the gas phase and the probe in the liquid phase were being compared to determine which showed a better light scattering event during a phase change. After the experiment was carried out in the liquid phase, the probe was positioned further up in the reactor so that it would be in the gas phase. As the pressure was increased at a constant temperature of 50ºC (in the same manner as with the probe in the liquid phase) the following signal response was captured.

125
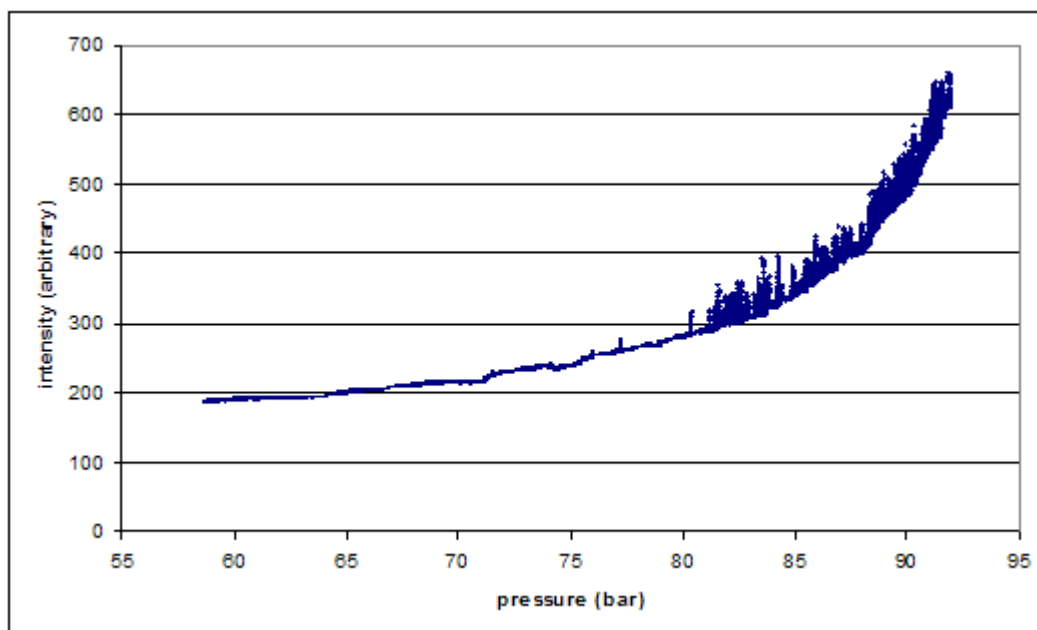
Figure 7.5: Unusual signal response from the critical opalescence probe

This response in Figure 7.5 is perplexing since it would imply light scattering gradually increases as the critical boundary is approached by increasing the pressure (at 50°C the critical pressure was expected to be near 96 bar). However, a gradual process is not expected over such a large pressure span. Even though the response was repeatable, there was no good explanation as why it was occurring. Later inspection of the known amount of methanol originally added in the reactor and probe position finally revealed the story.

As the pressure increased in the reactor, the liquid level began to rise closer and closer toward the probe. The surface of the liquid essentially acted as a mirror. As the level rose, the intensity of the reflected light increased giving the response in Figure 7.5. By knowing the initial amount of methanol placed in the system and the height of the

126

probe in the reactor, the intensity response can be converted into the volumetric expansion.

However, since this was not intended to be a volumetric expansion experiment, the precise height of the probe in the reactor was not known. But, by assuming a "ballpark" estimate of the height of the probe in the reactor, the response can be plotted in light of other expansion measurements using the moveable single-point probe (shown below in Figure 7.6). This qualitative depiction lends credence that this stationary technique can indeed be used to track changes in liquid level.
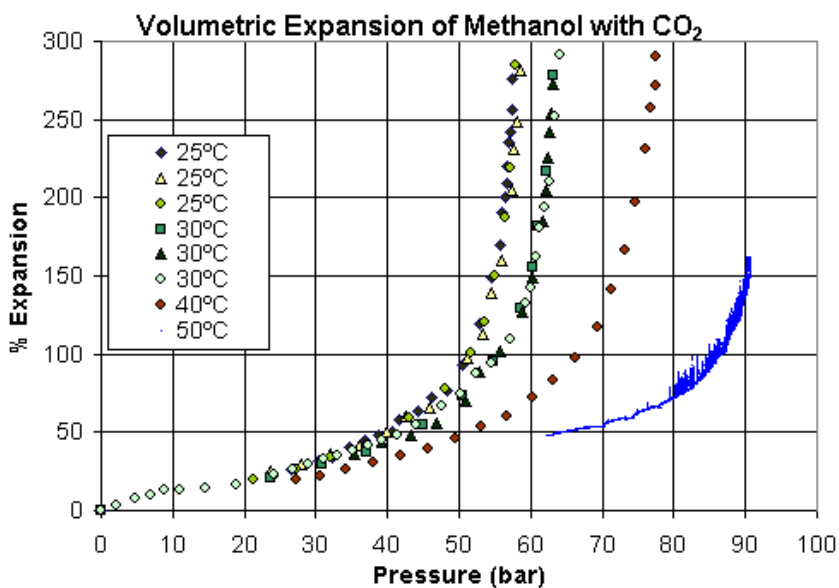
Figure 7.6: Isothermal volumetric expansion of methanol with carbon dioxide

However, this technique will have some limitations – most notably that the current opalescence probe may only be able to discern a difference in light intensity a few centimeters away from its face (limited to short ranges). Also, if the liquid level strays

far from being flat (wavy or bubbled), the response would be expected to fluctuate wildly – thus, the calibration process could become very complex.

7.6 Radio-Transmitter Tracers for Multiphase Flows

7.6.1 Motivation

The ideal multiphase flow inspection technique would be non-invasive, precise, easy to learn and implement, work in a vast array of operating conditions – especially industrial conditions, yield real-time information and, most importantly, be fairly inexpensive. Currently, there is no non-invasive technique that meets these criteria.

Radio-transmitters can meet all those criteria except for one: its precision ranges from tens of centimeters to a meter. van Barneveld et al. (1987) were the last ones to use this as a tracer technology in a chemical reactor. The technology then required a bulky tracer (3 cm sphere) and still had poor precision. Yet, since that time, thermometer pills and endoscopic pills have been used in the medical field, RFID technology has greatly improved, and ultra-wide band (UWB) transmission, radar imaging, and Bluetooth technologies have developed. It may now be possible to greatly improve the precision of a radio-transmitting tracer.

7.6.2   Proposed Research

Since CREL currently does not employ CARPT, it would be worthwhile to begin a preliminary investigation into radio-transmitting tracers. The first step would be to build up expertise in the area by consulting with an expert in radio frequency (RF) transmission to see what the theoretical limitations are for the newly developing RF technologies.

7.7   Hot-Film Anemometry Particle Mimicking in Fixed Beds

7.7.1   Motivation

The local liquid-coating of the packing, liquid velocity and liquid holdup throughout the reactor are necessary to properly describe multiphase flow in a fixed-bed reactor, such as a trickle bed. Invasive techniques are rarely employed in fixed-bed reactors because the packing obstructs and can even damage an invasive probe. However, in a fixed bed it is possible to use the packing to one's advantage so that a probe is no longer invasive but rather part of the packing structure. Hot-film anemometry has been developed for almost a century and has been successfully used to capture liquid velocity and gas holdup in multiphase flows. Boelhouwer et al. (2002) used a hot-film anemometry probe in the interstitial spaces of a packed bed to gain information on the liquid holdup, but they did not describe the particle wetting or the liquid velocities. No one has used a hot-film anemometer to mimic a packing particle.

7.7.2 Proposed Research

Thus, the creation of a hot-film anemometer that mimics the size and shape of the packing particles or catalyst used in a fixed bed would allow one to place multiple mimicking probes throughout various regions of the bed to gain not only the local liquid velocity and holdup but also the local wetting efficiency. Multiple mimicking probes could be strategically placed in the bed during the packing process or could be imbedded into structured packing.

Calibrations would need to be conducted since the manner in which the surrounding packing particles touch the mimicking probe would effect how the heat is conducted away from the probe. This project would require intensive effort and development.

Appendix A

Handbook of Fiber-Optic Probes

A.1 A Brief Tutorial on Fiber-Optic Probes

Every medium has a refractive index, which is always greater than one since the refractive index is defined as:

$$n_i = \frac{velocity\ of\ light\ in\ vacuum}{velocity\ of\ light\ in\ medium\ i}$$

Snell's law simply states that that at the boundary between two media, light bends away from the normal (a line perpendicular to the surface) when it enters the optically less dense medium, and bends toward the normal as it enters the optically denser medium. Snell's Law, shown in Figure A.1, describes optical transmission.
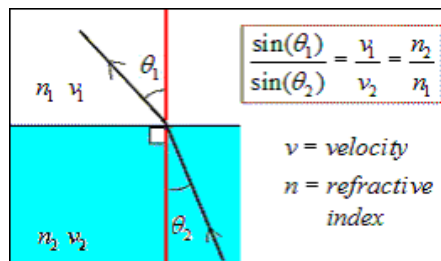
Figure A.1: Snell's Law

Now consider the situation where $n_1 > n_2$ and light is traveling in medium 1 toward the interface. The following possibilities are depicted in Figure A.2.
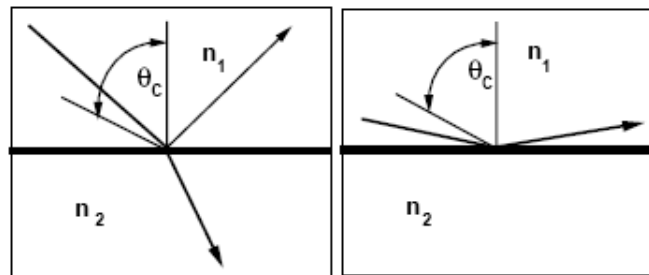
Figure A.2: Partial reflection (left) and total internal reflection (right)

Depending on whether the incident angle is less than or greater than the critical angle, θ_c, the ray of light in medium 1 can either partially transmit to medium 2 or totally reflect back into medium 1. A fiber optic cable employs the scenario shown on the right in Figure A.2. (Note: If $n_2 > n_1$ in the above scenario, the light would completely transmit from medium 1 to medium 2.)
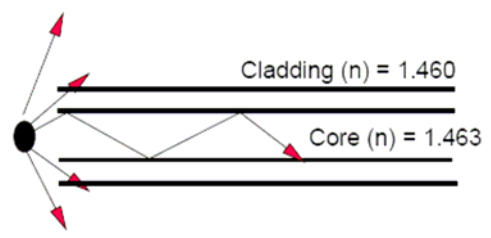
Figure A.3: Light propagation due to total internal reflection

In Figure A.3, light in the core that strikes the cladding wall at an angle greater than the critical angle will totally reflect and then strike the opposite wall and repeat this process all the way down the length of the fiber.

A.2 The Principle of the Fiber-Optic Probe in G-L Systems

As an example, the probe response to a bubble striking a single probe tip is shown schematically in Figure A.4.
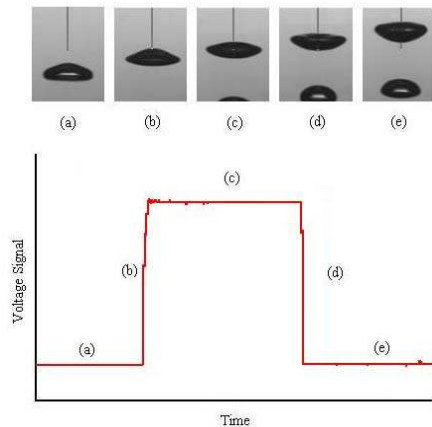
Figure A.4: Characteristic step response of a bubble striking the probe tip: (a) and (e) show the probe response in the liquid, (c) the response in the gas, and (b) and (d) the response of the tip entering and leaving gas/liquid interface

The reason that the response in Figure A.4 is possible is due to the tip of the fiber-optic cable being tapered into the shape of a cone (Figure A.5).
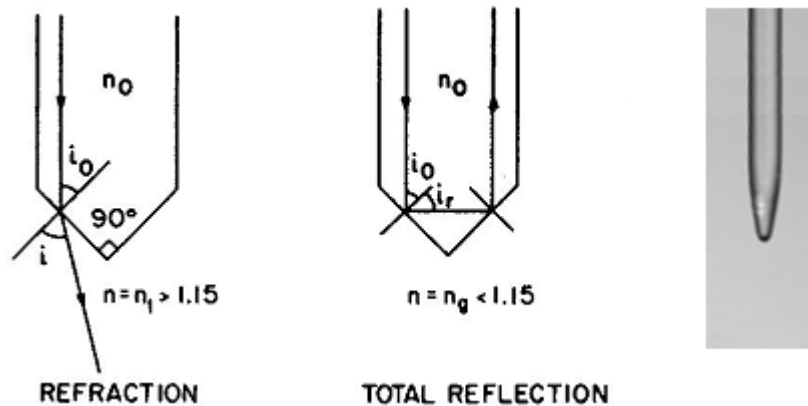
Figure A.5: Refraction, total reflection, and image of an actual probe tip

Since the refractive index of the glass core is approximately 1.5, the light refracts or reflects based on its angle of incidence with the conic end and based on the refractive index of the medium surrounding the probe tip. Thus, the probe is able to sense

133

changes between gases ($n \approx 1$) and liquids ($n \approx 1.3$-1.5), and G-L boundaries can be readily determined.

The opto/electrical components (termed "fiberbox") needed to generate and acquire the signal are shown in Figure A.6.
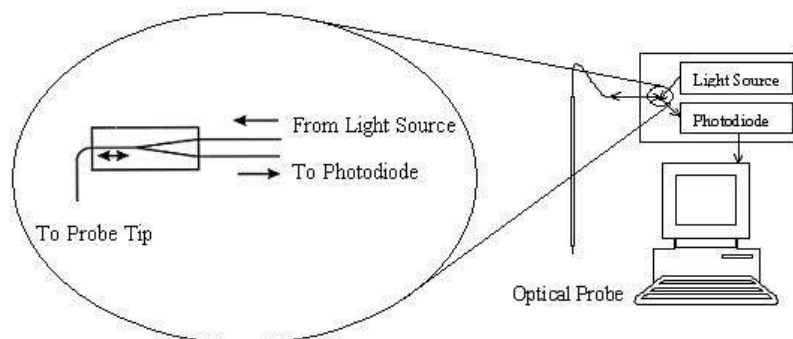
Figure A.6: Fiber-optic coupling and probe tip

The light source focuses light into one leg of a fiber optic coupler, which relays the light to the probe tip. When the tip is in the presence of gas, most of the light internally reflects and travels back up the fiber. When the tip is in the presence of a liquid, most of the light refracts out into the liquid, and very little light travels back up the fiber. The light traveling back up the fiber re-enters the coupler, which sends a percentage – usually 50% – of this reflected light down the other leg of the coupler to a photodiode. The photodiode then converts the quanta of light into a voltage signal for much like that in Figure A.4.

A.3 Tools of the Trade

A.3.1 What You'll Need to Manufacture Your Own Fiber-Optic Probes

- An open workspace equipped with a table and chair.

- A hydrogen cylinder and oxygen cylinder equipped with regulators and a flame torch (shown below in Figure A.7).

Figure A.7: $H_2/0_2$ cylinders and torch

- Glass, multimode fiber optic cable, 200 micron core, 230 micron clad, 500 micron coat (about 100 meters to start). Part #: BFL37-200 from Thorlabs.com, $US 0.90 per meter.

135

- Scissors for coarsely cutting the fiber optic cable.

- A fiber stripper for stripping the jacket off of the fiber. Part #: T12S21 from Thorlabs.com $US 65.00

- A stand with a clamp arm for suspending the cable in order to cut the fiber with the torch. Shown below in Figure A.8, the clamp arm holds a short section of stainless steel (SS) tubing with a ½" section of soft, flexible tubing fitted at the top of the SS tubing. Once the fiber is threaded through the tubing, a clip is used to pinch the soft tubing in order to hold the fiber in place and prevent the weight from pulling the fiber down

Figure A.8: Stand for suspending the fiber optic cable for flame cutting

- A weight to hang from the bottom of the fiber in order to make the proper cut (shown in Figure A.9). The weight is simply a large clip with some soft tape on it to prevent the clip from pinching too hard on the fiber (and thus damage to the fiber).

136

Figure A.9: Weight used to pull the fiber optic cable taut

- A diamond-tipped fiber scribe in order to trim the fiber tip after it has been cut.

  Part #: S90W from Thorlabs.com

- A microscope equipped with a light in order to trim the fiber with the diamond-

  tipped cutter (shown below in Figure A.10).

Figure A.10: Microscope used for inspecting the fiber tip

- A jig for positioning the 4 tips into the 3-D array shown below in Figure A.11. (see Xue (2004) – this will have to be made in a machine shop)
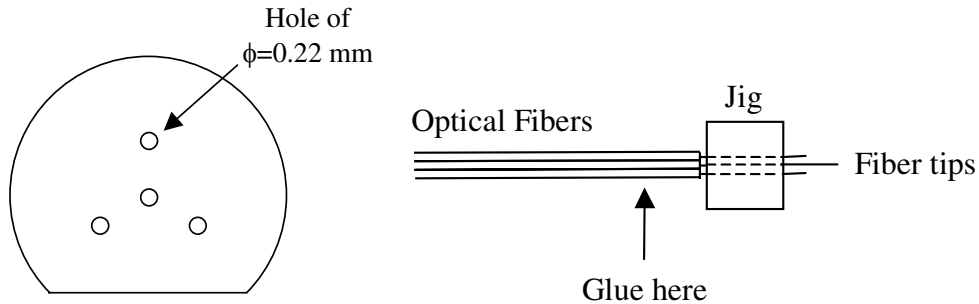
Figure A.11: Plastic jig for the 3-D array

- Devcon 5-minute epoxy for gluing the fibers in place. $US 5.00

- Stainless steel tubing (1/8" OD, 0.105" ID) for mounting the 3-D array with epoxy (on average 12-18" needed per probe). $US 13.87 per 28".

- A tube bender for bending the SS tubing (if desired). Part #: 2492A12 from McMaster-Carr, $US 28.52

- A fiber cleaver for making flat, clean cuts on the back ends of the probe. Part #: XL410 from Thorlabs.com, $US 1360.00

- An SMA Connectorization Toolkit for making SMA connections. Part #: CK01 from Thorlabs.com (this includes the diamond-tipped fiber scribe), $US 542.00

- A Sharpie pen, lockable tweezers, a pointed pair of tweezers, toothpicks, and masking tape.

- An imaging system to snap pictures (as in Figure 2.8) to determine the precise location of each probe tip in x,y,z coordinates

- DALSA cameras, EPIX imaging and software, lenses and computer ~$US 10,000

- **TOTAL** ~ $US 2200.00 (not including the microscope, imaging system, and cylinder/torch)

A.3.2 Opto-Electronics for Data Acquisition

- A computer workstation equipped with a good processor, storage capacity and RAM – you'll need to have Fortran installed to run the data processing algorithm.

- A data acquisition board for high-speed measurements. Part #: PD2-MFS-8-1M/12 from PowerDaq. ~$US 3500.00

- Four BNC cables. Part#: 2249-C-36 from Pomona, ~$US 15.00 per cable.

- Four multimode fiber splitters (couplers). Part #: 15-32200-50-11301 from Gould Fiber Optics, $US 150-200 per splitter

- A bright light source (or 4 laser diodes of ~700 nm wavelength such as CPS198 from Thorlabs.com with power supplies) to shine into one leg of the couplers.

- Four photodiodes for generating the voltage signals from the light responses. Part #: PDA10A from Thorlabs.com, $US 278.00 per photodiode.

- Four SM1SMA connectors for connecting the fiber to the photodiode. Part #: SM1SMA from Thorlabs.com $US 26.00 per connector.

- Four SMA connectors to route one leg of the coupler to the photodiode. Part #: 10230A from Thorlabs.com, $US 9.45 per connector.

- Four grey, 1/8" OD PVC tubes (about ¾" long) with 525 micron bore through the center (along the axis of the tubing) to align the fiber of the coupler with the fiber from the probe. (This connector will have to be made in the machine shop) The schematic of the connector is shown below in Figure A.12.
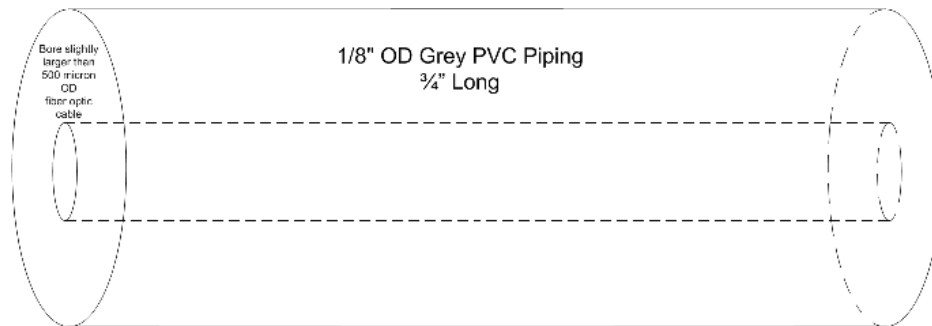
Figure A.12: Schematic for PVC connector (for connection between the probe and the fiberbox)

- Index matching gel for making clean connections between the probe and the couplers. Part#: G608N from Thorlabs.com
    - TOTAL ~ $US 5700.00 (not including computer or light source)

A.4 Step by Step Procedures

A.4.1 Making the Fiberbox (Opto-Electronics)

1. Strip about 1" of the jacket off one leg of each coupler and attach the SMA connector to that leg. Follow the instruction included in the Connectrorization Toolkit Manual to attach the SMA connector and polish the ends.

2. Install the SM1SMA connector on each of the photodiodes and then screw in each of the SMA connectorized legs of the coupler.

3. Connect each photodiode to the data acquisition board with the BNC cables.

4. Mount the other legs of the coupler in the light source.

5. Insert the remaining end of the coupler into each of the grey PVC connectors to be ready for connection with the probe.

6. The opto/electronics setup (Fiberbox) is now complete. The general schematic is shown below in Figure A.13.
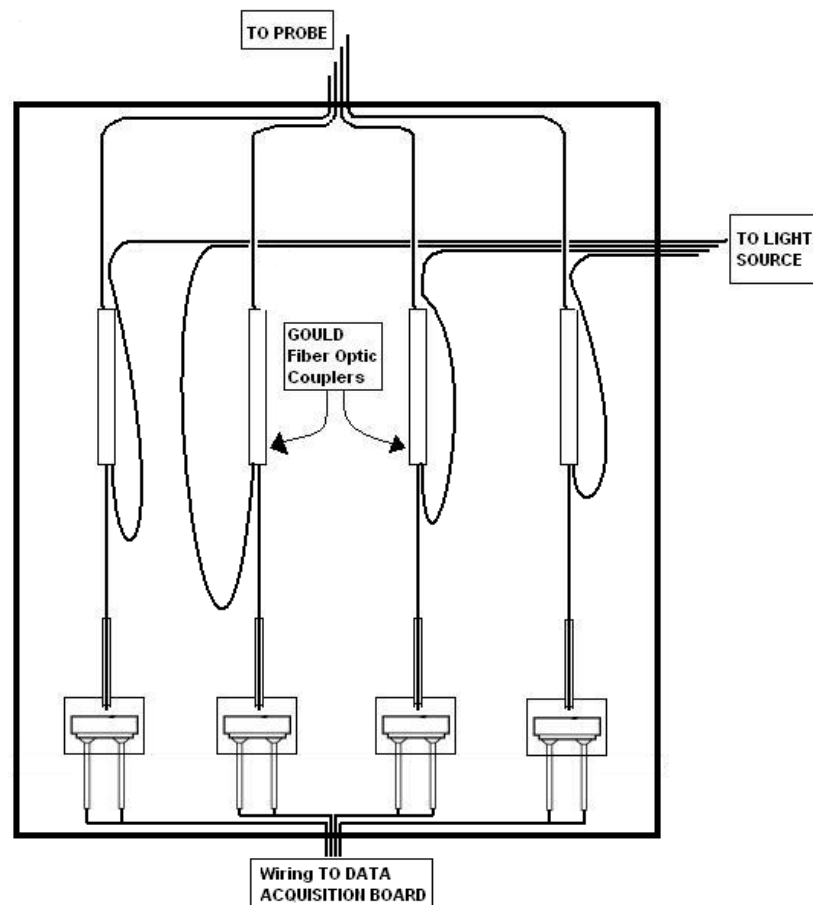
Figure A.13: General concept of the fiberbox

141

A.4.2 Making the 4-Point Probe

1. Using scissors, cut four lengths of fiber – each approximately 2 meters in length.

2. Repeat the following sequence for each of the four fibers:

   a. Strip about 1" of the jacket off one end the fiber.

   b. Hang the fiber from the stand and attach the weight to the stripped end leaving about ½" of the stripped fiber exposed.

   c. Use the hydrogen/oxygen torch to create a small, intense flame and cut the fiber just above the weight. As the glass melts, the weight pulls the on the fiber which eventually snaps creating the tapered end. The size of the flame is shown below in Figure A.14.

Figure A.14: Size and shape of intense H_2/O_2 flame

d. Under the microscope, use the diamond-tipped scribe to trim the tapered end to the desired geometry. (see Figure A.15 below)
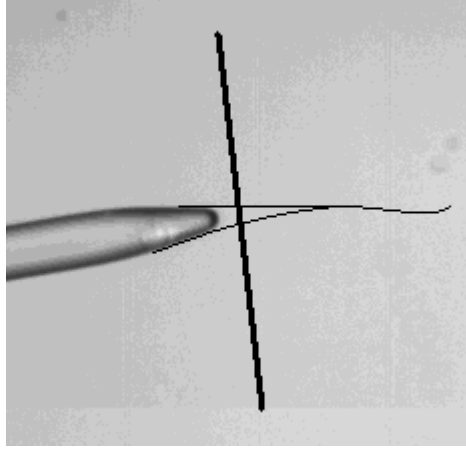
Figure A.15: Typical tip after the flame cut; typical trim point and resulting rip after flame polishing

e. Using the torch – only a gentle hydrogen flame (shown in Figure A.16) – polish the very tip of the fiber. This melts the flat end left by the scribe into a more rounded point. If a very intense flame is used, it will melt the glass too quickly and actually blow the tip over.
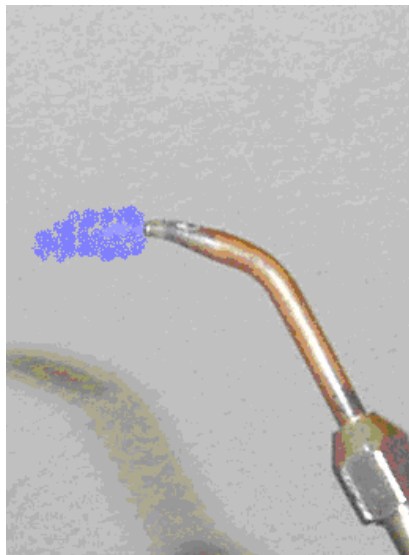
Figure A.16: Flame size and shape for flame polishing

143

f. Ensure that about 10 mm of the glass (including the tip) is exposed beyond the jacket. If not, use the stripper to strip off any excess of the jacket.

g. Test the fiber.

    i. On the back end of the probe, strip off about 7 mm of the jacket and use the fiber cleaver to make a flush cut of the fiber (almost at the point where the jacket is just removed).

    ii. Apply a small amount of index matching gel to the back end of the fiber and mate it with a coupler using the grey PVC connector. It will help to tape the coupler (and fibers) in place to make sure they don't move during testing. A reliable connection is made when the tip is the brightest.

    iii. With one channel of the probe now connected to the Fiberbox, check to make sure that the voltage drops are acceptable by dipping the probe tip repeatedly in a glass of water.

    iv. If the voltage drops are not acceptable, first try repeating step e. (The most common problem is under-polishing the tip.) If that does not work, remake the tip again.

3. With all four of the fiber tips now made and functioning well. Insert the four fibers, back-ends first, into the section of stainless steel tubing (bend the tubing if required). Leave about 1 ½" of fiber exposed from the tip to the tubing. This

will help to keep the fibers together so that they can be more readily aligned in the jig.

4. Place the jig in the lockable tweezers so that the triangle is pointing downwards toward the table and align the tubing/fibers with the face of the jig. (see Figure A.17 below)
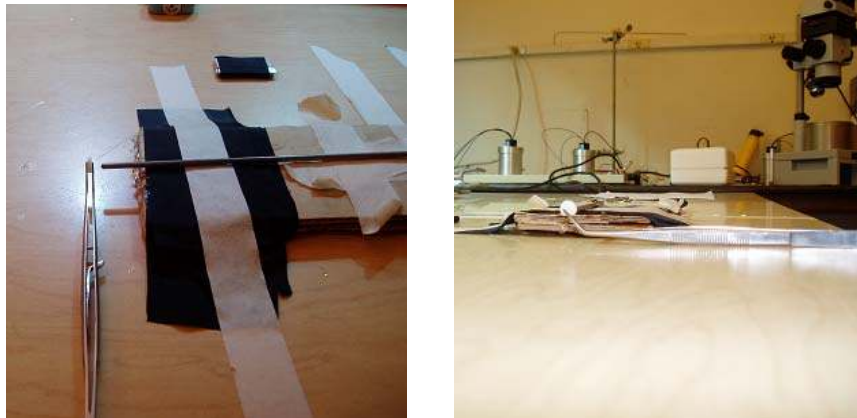
Figure A.17: Positioning of the jig

5. Take one fiber and thread it into the bottom-most hole in the jig.

6. Thread the next fiber into the center hole and then thread the remaining two fibers into the two upper-most holes.

7. Identify which fiber is threaded into each hole of the jig by gently tugging on the end of each fiber to see which moves. Mark the ends with the Sharpie so that they can be readily identified.

8. The next four steps will have to be done quickly (within the 5 minute cure time of the epoxy).

    a. Mix the epoxy thoroughly with a toothpick and apply the epoxy only along the jacket of the fibers (do not place epoxy on the glass of the

145

fiber). Start about 3 inches from the exposed glass and apply the epoxy to the upper and undersides of the fiber bundle being careful not to pull the fiber ends out of the jig. Continue to cover the fiber bundle with epoxy until you are about 1 inch away from the exposed glass.

b. Holding the fibers in place, pull the stainless steel tubing up toward the tips. As the tubing moves it will pull the epoxy along with it, so be sure to clean off any excess with a toothpick. Pull the tubing to about ¼" away from the exposed glass.

c. Having identified which fiber is threaded into each hole, adjust the lengths of the fibers in the jig by pulling on the end of the appropriate fiber. The 3 outer fibers should all be set at the same length with the central fiber approximately 2 mm longer.

d. With the fiber lengths now set in the jig, hold the back end firmly and gently push the tubing so that the glue/tubing is almost near the exposed glass. Be sure to remove any excess glue from the SS tubing.

9. Allow the glue to dry. Wait at least 30 minutes to allow the glue to cure more.

10. Once the glue has dried, carefully pull the probe from the jig and place the probe securely so that the probe tips are safe from hard impacts.

11. Secure any appropriate fittings on the probe (for insertion into a reactor) by running them up the back of the probe.

12. Plug in the fibers to the fiberbox.

13. The 4-point probe is now ready for use.

14. Note: The use of the jig has been eliminated for creating the mini 4-point probe (see Appendix A.4.3 below). Instead, a much simpler "annealing" process is used to array the 4 fibers in a more compact manner and could also be used in the creation of the normal 4-point probe.

A.4.3 Making the Mini-probe

By employing smaller fibers, packing the fibers closer together, and sheathing them in 1/16" OD SS tubing, flow disruption in a reactor is reduced and smaller bubbles can be detected by the mini-probe. The preparation of the tips (Appendix A.3.2.1-A.3.2.2) is exactly the same; however the 105 μm core fiber (125 μm clad) is used. The next steps are then used to create the mini-probe.

1. Take two of the fibers and recess one fiber so that it is 0.75 – 1 mm shorter than the other and lay the two fibers on a piece of tape.

2. Take a 2"inch long piece of scrap fiber and lay it on the other side of the longer tipped fiber as in Figure A.18.

To be the central fiber

Dummy fiber

Tape
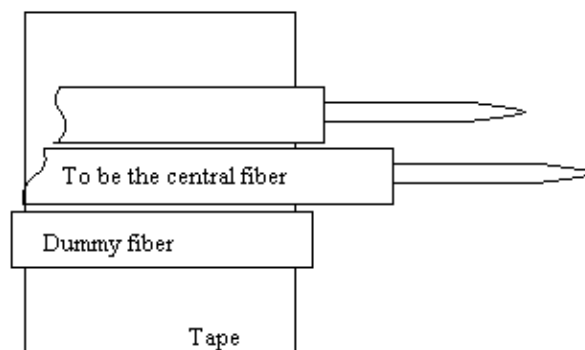
Figure A.18: Annealing two fiber-tips together (side view)

147

3. With these 3 fibers laid flat and pushed as closely together as possible, lightly glue the fibers together on the exposed face – being sure to remove any excess glue by gently brushing the exposed surface with a cotton swab.

4. Allow to dry for 10 minutes

5. Place a small amount of glue along the axis of the central/dummy fiber joint and affix the 3rd fiber along that joint (Figure A.19 below)– being sure to recess this 3rd fiber 0.75 – 1 mm from the central tip.
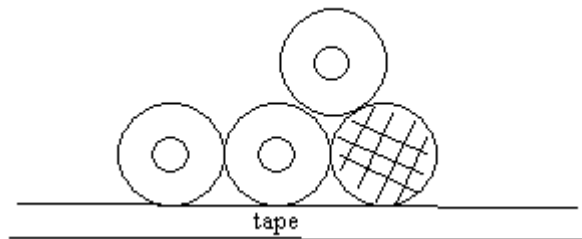
Figure A.19: Annealing the 3rd fiber-tip ("head-on" view)

6. Allow to dry for 10 minutes

7. Remove the tape from the bottom face of the fiber bundle.

8. Apply a small amount of glue along the now exposed bottom axis of the central/dummy fiber joint and affix the 4th fiber along that joint (Figure A.20) – being sure to recess this 4th fiber the same distance as the 2nd and 3rd fibers.
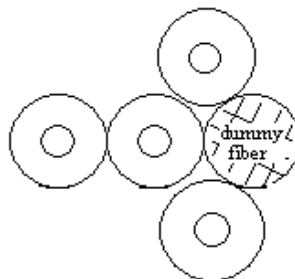
Figure A.20: Annealing the 4th fiber-tip ("head-on" view)

148

9. Allow to dry 10 minutes

10. Pull a section of 1/16" OD (0.115" ID) SS tubing up the back of the fibers and glue the 4 annealed tips into the tubing

11. The mini-4-point probe is now ready to be imaged and used.

12. Note that a special connector is needed to connect the mini-probe to the fiberbox. The connector is the same as in Figure A.17 except that one half of the connector is bored a smaller size to just accommodate the jacketed diameter of the smaller fiber (see Figure A.21 below).
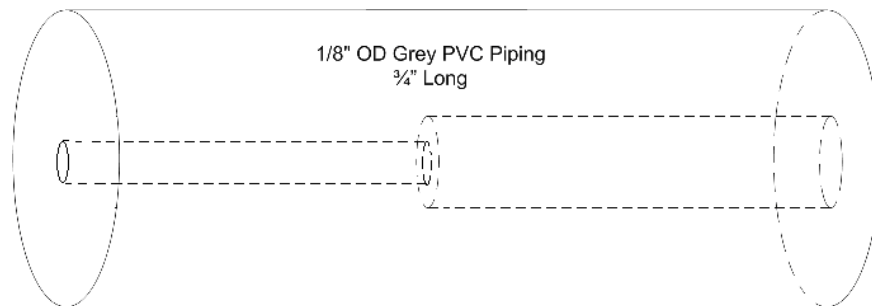
Figure A.21: Special connector for the mini-probe

A.5 The History of High-Temperature, High-Pressure, Single-Point Probe Development

Certain probes were created for use, but were then surpassed by improved designs. The goal of this section is to record the older designs so that the reader can see what worked and what did not work.

A.5.1 High-Pressure, Chemically Resistant Single-Point Probe

The first probe developed to measure volumetric expansion had three major design flaws. The first flaw was that the epoxy used to glue the fiber in place would soften and begin to disintegrate under reactor conditions (this ultimately led to probe failure, the fiber being blown out of the probe, and pressure loss in the reactor). The second flaw was the type of fiber used. The first probes had a glass core and a soft cladding sheathed in a protective jacket. This soft cladding would swell under reactor conditions – so much that the cladding could even cover the probe tip and render the probe useless. The third flaw was that the fiber could only withstand temperatures up to 100ºC. The probe design in Figure A.22 successfully addressed the first two problems.
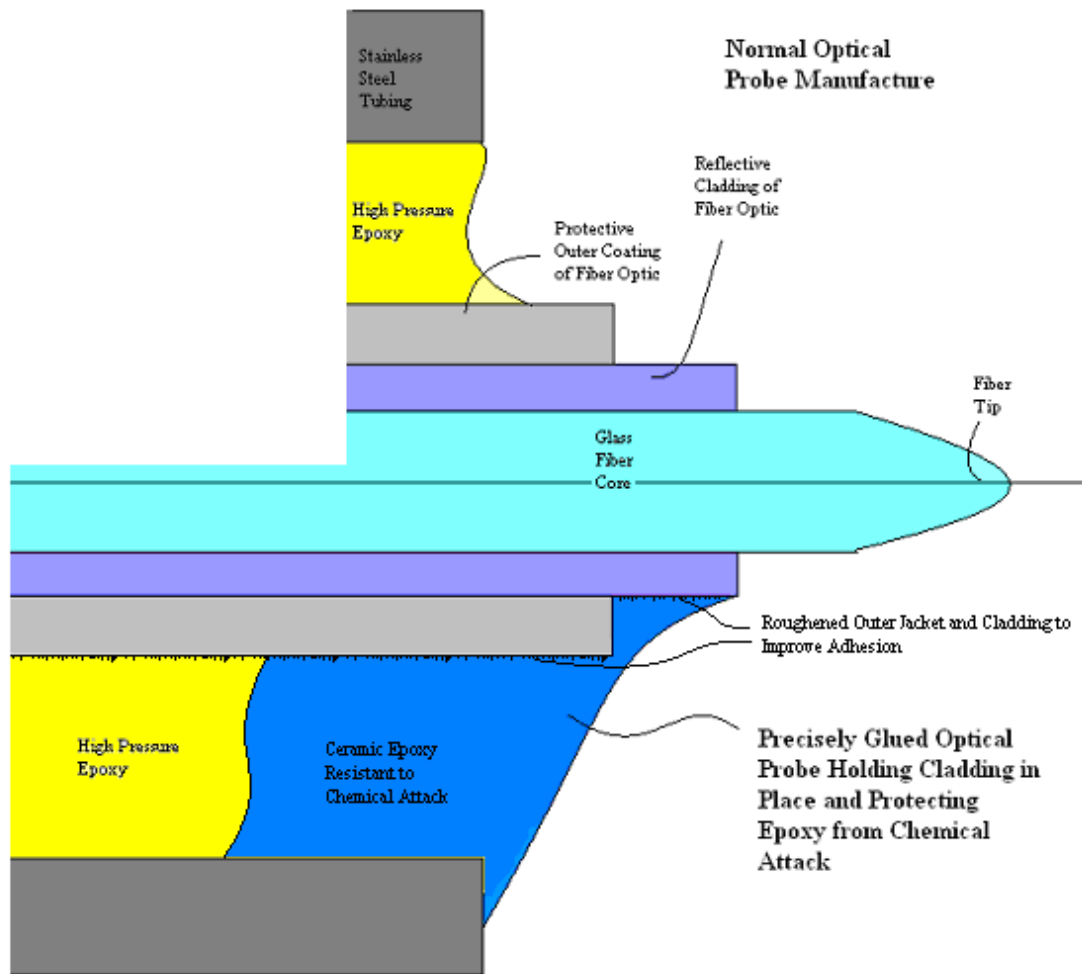
Figure A.22: Improving the single-point probe construction

By using a ceramic epoxy to shield the high pressure epoxy, jacket and cladding, the chemical degradation of the epoxy was eliminated and the swelling of the cladding minimized. (Switching to glass-clad fibers later completely eliminated the cladding swelling problem.) Roughening the jacket and cladding of the fiber (light sanding) improved the adhesion of the epoxy to the fiber so the probe could work at higher pressures.

Aluminum-jacketed fibers then altogether replaced the normal optical fibers for use in high pressure, high temperature, and chemically aggressive systems. Aluminum fibers can be used up to 400ºC, adhere to the epoxy best (working pressure of 2200 psig), and resist chemical attack. The next section was an attempt to improve the reusability of the probe and reduce the time needed for construction.

A.5.2 Glue-less, High-Temperature/Pressure Single-Point Probe

By enclosing a ferrule inside regular 1/8" tubing and using a nut that is flush with the walls of the tubing a single aluminum fiber can be mechanically sealed into the probe with the use of no glue (shown in Figure A.23).
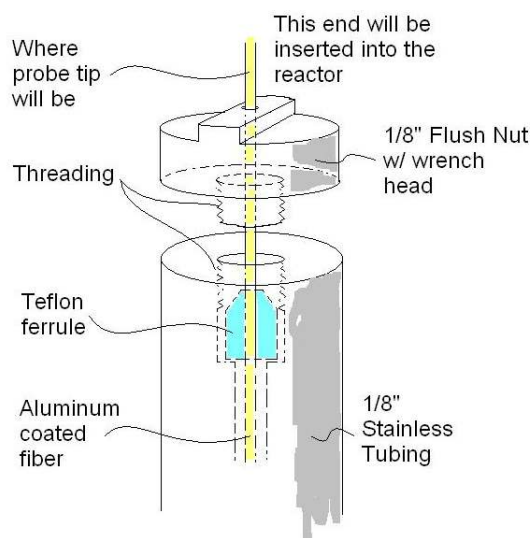
Figure A.23: The glue-less, high temperature/pressure, single-point probe

The benefits of this probe design are 4-fold: 1- the aluminum fiber is chemically resistant to organic solvents; 2- the aluminum fiber can withstand temperatures of 400ºC (we were limited to 100ºC with the old fiber); 3- the use of a ferrule eliminates

152

the need for glue and therefore makes the probe tubing and nut, as well as the fiber itself, reusable; and 4 – the elimination of the gluing procedure and reusability of the probe greatly decreases the time it takes to make the probe. If a fiber tip breaks, the probe can be disassembled, the fiber-tip remade, and the probe reassembled again – this also reduces waste since every time a tip broke in the past the entire probe (stainless tubing and length of fiber in the tubing) had to be thrown away. However, many ferrules must be made since they are not be reusable – but this cost is very small.

After testing, the probe was found to withstand pressures up to 500 psig before a tiny leak developed where the ferrule sealed with the aluminum fiber. This pressure limitation is due to the fact that the nut can only be tightened so much due to its small size. Therefore, the design was abandoned for the glued probe with the aluminum jacketed fiber that withstands pressures of 2200 psig. However, for systems below 500 psig, this type of probe may be successfully used.

A.6 Single-Point Probe Manufacture (for Gas Holdup and/or Volumetric Expansion)

Depending on the application – simply measuring gas holdup or needing a probe to withstand high pressure, high temperature or chemically aggressive systems – a variety of probe designs can be employed. But, it is the reactor/reactor conditions that will ultimately determine how the probe is constructed. In all instances, the preparation of the tip (Appendix A.3.2.1 - A.3.2.2) is exactly the same using either the 105 μm core

fiber or the 200 µm core fiber. This section will address single point probes for use in

1) high pressure, high temperature, chemically aggressive systems 2) small reactor

volumes 3) impeded reactor volumes (monoliths, packed beds, etc.)

A.6.1   Current High-Temperature, High-Pressure, Single-Point Probe Design

1. Remove about 1" of the aluminum jacket by dipping the end of the fiber in a stirred 1M solution of NaOH at 40ºC and allowing the jacket to dissolve away

2. Finish the tip as in Appendix A.3.2.1 –A.3.2.2.

3. Obtain at least 16" of 1/8" OD (with an ID no larger than 1/16") SS tubing as the sheath.

4. Mix the Devcon white ceramic epoxy and set aside for later use in step 8.

5. Mix and apply the Devcon 5-minute epoxy about an inch below the tip of the fiber and along the axis of the fiber for an additional 14".

6. Pull the SS tubing up the back of the fiber being sure to clean off excess glue as the fiber is pulled up (move the fiber slightly in and out as the sheath is pulled up to get as much glue into the sheath and on the inner walls of the sheath as possible).

7. Pull the SS tubing all the way up to the exposed glass being sure to leave about 2 mm of the aluminum jacket exposed.

8. Apply the ceramic epoxy to the 2 mm of the exposed aluminum jacket being sure to completely cover the epoxy underneath (refer to Figure A.22).

154

9. Set aside and allow to dry overnight.

10. The probe is now ready for use.

A.6.2 Small Reactor Volumes

When faced with a small reactor volume where flow disruption must be minimized or clearances are such that only small openings allow access inside the reactor or smaller bubbles need to be detected, it is important to make the single point probe as small as possible. Use 105 μm core fiber for improved bubble detection and use smaller tubing (1/16" or smaller) to reduce flow disruption. If the probe isn't used in a high pressure system, only place glue just below the exposed glass and along the axis of the fiber for about ½" – if the tip is damaged, the last 1" of the probe can be simply cut off and the tubing and fiber reused.

A.6.3 Impeded Reactor Volumes

Optical probes have been used in packed beds, but there is increased risk of damage to the probe tip as it must be laid into the packing without any SS sheath – if the fibers are glued into a sheath, the tips will snap off. Thus, once the tip is made the fiber simply needs to be laid into the reactor, the packing gently poured on top of the fiber, and the fiber somehow sealed into the reactor. However, this does not guarantee the probe will be able to give meaningful measurements for holdup since the placement of the tip in the bed may be in a dry spot or in a perpetual wet spot in the reactor.

Bare fiber tips have also been implemented in monolith reactors by simply placing the fiber down one of the channels in the monolith grid. However, measurements of holdup are suspect due to the fact that even a small fiber significantly reduces the cross sectional area for flow in that given channel and may cause bypassing in that particular channel.

A.7 Steps of 4-point Probe Data Acquisition

1. Image the 4-Point Probe to Obtain Coordinates of Each Fiber Tip

    a. The central tip acts as a frame of reference for the other three tips; thus the position of these 3 tips (x,y,z coordinates) relative to the central tip are needed.

    b. Install the "micro" lens on the DALSA camera and use the EPIX imaging software to snap close-up images of the probe tips axially and "head-on" (such as in Figure 7).

        i. Use the "pixel-peek" tool in the EPIX program to locate the precise location (in pixels) of each tip in the x, y, and z coordinates.

        ii. Normalize the coordinates of the 3 outer tips by using the central tip as the origin (0,0,0)

        iii. Divide the x,y,z pixel coordinates of the 3 outer tips by 10 and again by 61 (inputs to the Fortran program are required in cm)

156

1. (# of pixels)*(1 mm / 61 pixels)*(1 cm /10 mm) =

   coordinate in cm

Note: This procedure is for using the PowerDAQ data acquisition software in conjunction with Excel and Fortran for data processing.

2. Simple Test (PowerDAQ software)

   a. This program is used to analyze the response of each channel once the probe is plugged in to the fiberbox to ensure that voltage drops are acceptable for data analysis later

   b. Settings ("Analog In" tab)

      i. Sample rate: can be varied to user preference to determine signal

      ii. Type: bipolar (both + and – voltages)

   c. Startup

      i. Set "Total Channels" to 4

      ii. Click the "Start" button to view the response

      iii. Select the "Active Channel"

         1. select from 0, 1, 2, 3 to view each of the 4 channels

3. Stream to Disk (PowerDAQ software)

   a. This program is used to collect the data. There are many possibilities to change the type of data acquisition performed by this

program; however, the only changes that need be made will be defined below. If not specified below, simply hit enter in the program to accept the default.

b. Inputs

 i. Clock rate: 40 (this number is in kHz)

 ii. Number of frames: user defined (typically 500-800)

  1. 1 frame = 8192 samples, so (# of frames)*(8192 samples/frame)/(sampling frequency) = measurement time

 iii. File name: filename.**da1** (.D A one file extension)

c. After the filename has been entered and the triggering default accepted, the program will begin the data acquisition

4. PD-SR (PowerDAQ software)

a. This program is used to convert the .da1 file to a .txt file which is then processed by the Fortran program. Note the difference in size (MB) compared to the .da1 file and the finished .txt file.

b. Inputs

 i. Binary file: filename.**da1**

 ii. Output file: filename.**txt**

c. Options

 i. Click on the "Options" tab to ensure the following are set (these will typically be the default setting):

1. Channels: check channels: 0, 1, 2, 3

2. Board: check the PowerDAQ II (DAQ-11 for the older model boards)

3. Resolution: check 14 bit (12 bit for the older model boards)

4. Input range: +/- 5 volt

5. Sample/read: 0

5. Excel

   a. Open filename.txt in Excel as a comma delimited worksheet to view the 4 columns of data (1 column for each of the 4 signals).

   b. Insert a column at the far left (as column A) and create a sequence step as: A1 = 1, A2 = 2, A3 = 3 …

   c. Plot the data against the sequence step to view a sample of bubble strikes interacting with the 4 tips

   d. Read the liquid and gas baselines for each signal from the graph using the general rule of thumb (shown in Figure A.24):
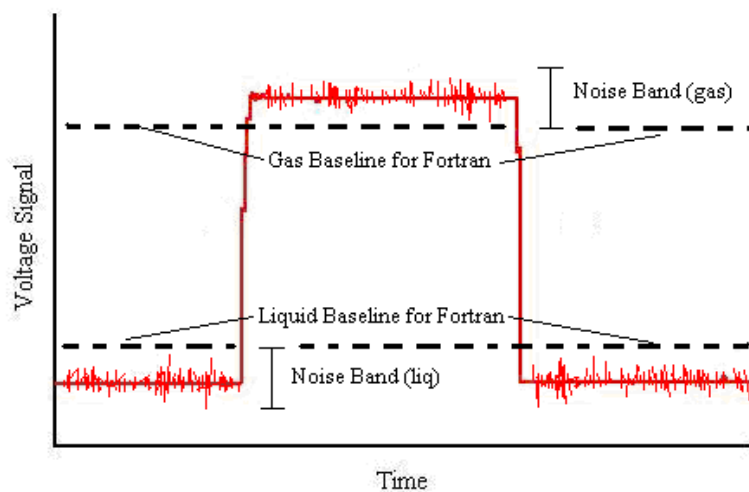
Figure A.24: Determination of gas and liquid baselines for processing

    e.   These 8 baselines, along with the geometric coordinates obtained from imaging the probe tips (Section 4.1.1) are then input into the Fortran program bubblestandard.f.

6.   Fortran

    a.   Open bubblestandard.f

          i.   Inputs (the required inputs are underlined from now on)

               1.   Filenames of input .txt file and output files

                    a.   character*<u>#</u> name (the # must correspond to the letter length of the input file in b. below (8 for filename)

                    b.   parameter (name=<u>**'filename'**</u>)

                    c.   character*<u>#</u> nbme (the # must correspond to the letter length of the result file in d. below (7 for nresult)

160

  d. parameter (nbme='**<u>nresult</u>**')

2. Baselines (the numbers are examples)

  a. parameter(water1=**<u>2.96</u>**)

  b. parameter(gas1=**<u>3.28</u>**)

  c. parameter(water2=**<u>3.17</u>**)

  d. parameter(gas2=**<u>3.30</u>**)

  e. parameter(water3=**<u>2.99</u>**)

  f. parameter(gas3=**<u>3.16</u>**)

  g. parameter(water4=**<u>2.83</u>**)

  h. parameter(gas4=**<u>3.06</u>**)

3. Tip geometry (division by 61 done here instead of as explained in 4.1.b.iii) Note that x2 refers to the x coordinate of the tip plugged into channel 2 of the fiberbox.

  a. x2=**<u>3.25</u>**/61.0

  b. y2=**<u>1.9</u>**/61.0

  c. z2=**<u>13.3</u>**/61.0

  d. x3=**<u>-3.05</u>**/61.0

  e. y3=**<u>1.85</u>**/61.0

  f. z3=**<u>12.6</u>**/61.0

  g. x4=**<u>1.45</u>**/61.0

  h. y4=**<u>-4.25</u>**/61.0

i. z4=**15.0**/61.0

b. Build, compile and run the program with all the inputs entered

c. The program will run and create a filename.dat result file along with a nresult.dat result file.

    i. Outputs for the filename.dat result file (for each counted bubble strike):

        1. number

        2. beginning bit #

        3. bubble velocity (cm/s)

        4. φ

        5. θ

        6. chord length (t1*v1)

        7. chord length (t2*v2)

        8. chord length (t3*v3)

        9. chord length (t4*v4)

        10. Δt1

        11. Δt2

        12. Δt3

        13. velocity 1 (2-point) [usually not used]

        14. velocity 2 (2-point) [usually not used]

        15. velocity 3 (2-point) [usually not used]

    ii. for the last 3 lines of the filename.dat result file

162

1. Line 1

    a. Total # of bubbles hitting the center tip

    b. Accepted number of bubbles

    c. Ratio of accepted bubbles to total bubbles

    d. Nmax [not used]

    e. Collection Frequency [usually 40000 Hz]

    f. Collection Time [never used]

    g. Averaged Velocity [in cm/s]

    h. Counter3-1 [not used]

    i. Counter7 [not used]

2. Line 2

    a. Specific area (cm^2/cm^3)

3. Line 3

    a. Gas holdup (%)

d. Xue (2004) created Matlab programs to plot velocity and chord length distributions. However, it is easier to generate a simple Excel template so that one can simply copy and paste the data from filename.dat directly into the template and then use the FREQUENCY statistical tool in excel to generate the probability distributions.

Appendix B

Additional Results Not Presented in the Dissertation

B.1   Volumetric Expansions of Organic Solvents

Volumetric expansion data of ethanol, methanol, acetone, acetonitrile, 1-octene, nonanal, ethyl acetate, and cyclohexane with carbon dioxide are presented – note that the complete toluene expansions were presented in Chapter 5.3. When comparison with literature results is available, the graphs are shown (ethanol, methanol, acetone and acetonitrile).
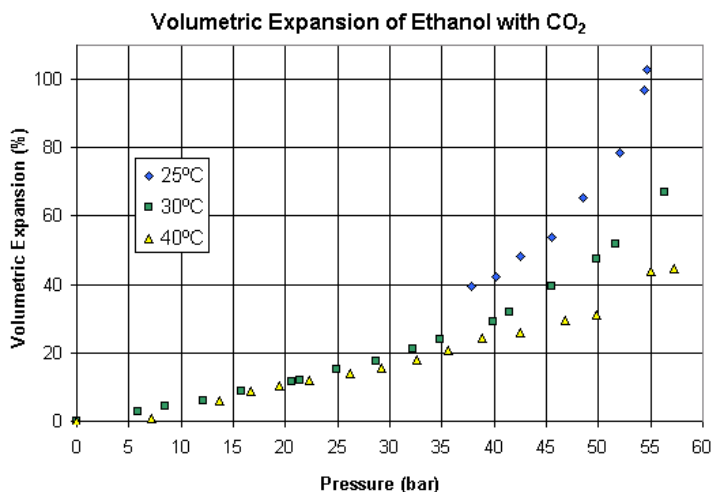
Figure B.1: Isothermal volumetric expansions of ethanol with CO_2
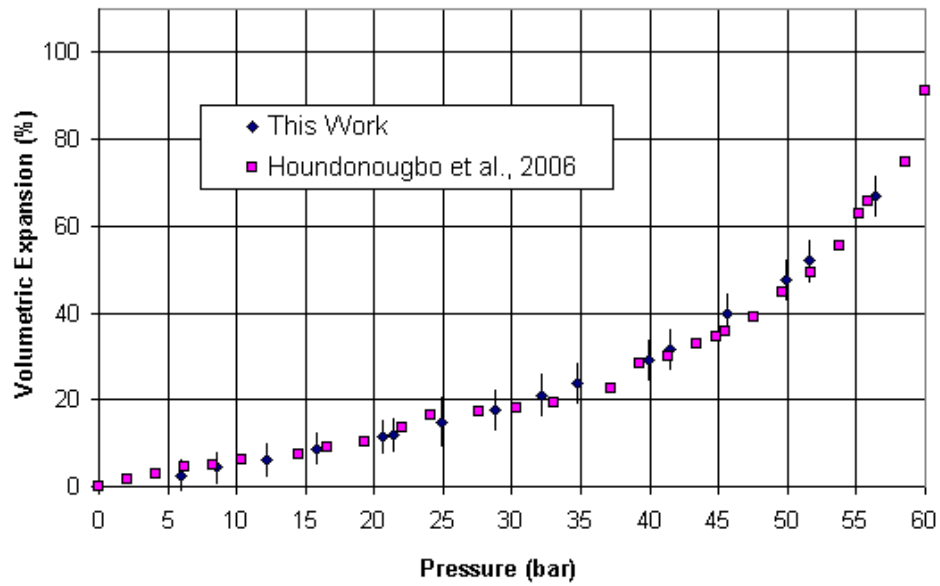
Figure B.2: Volumetric expansion of ethanol with CO_2 at 30 ºC
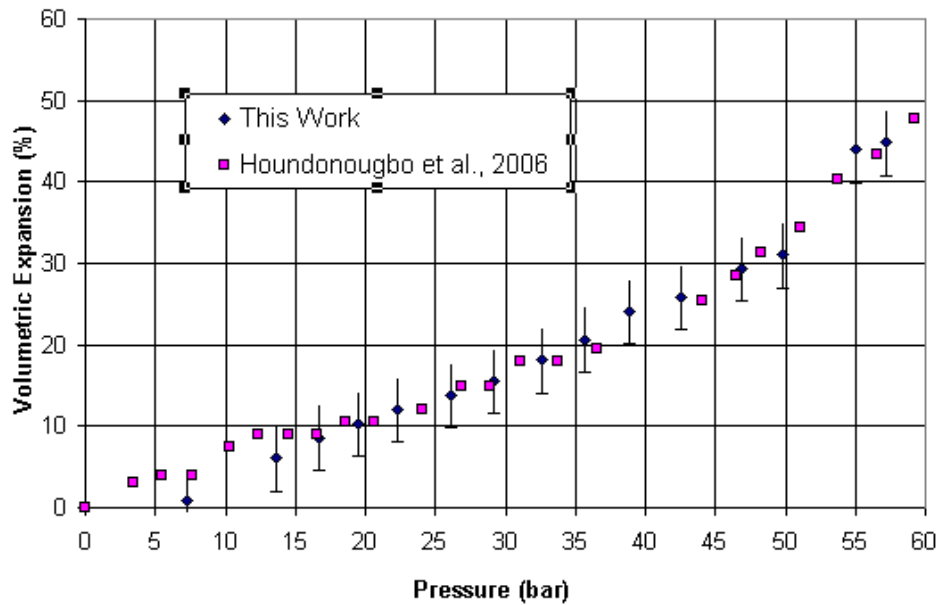
Figure B.3: Volumetric expansion of ethanol with CO_2 at 40ºC

165
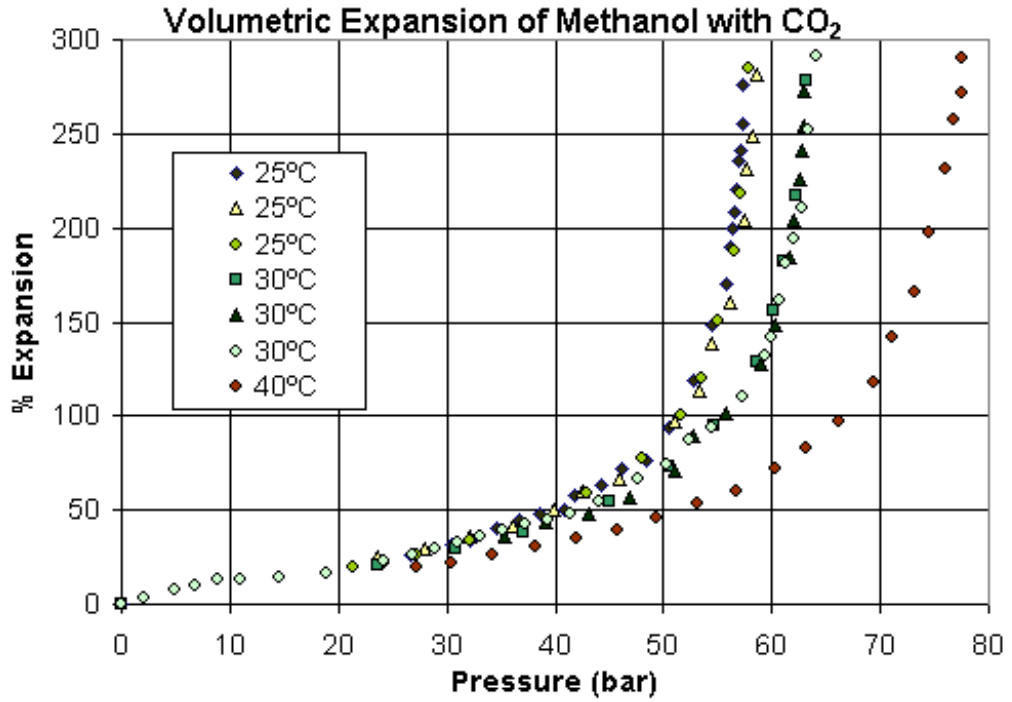
Figure B.4: Isothermal volumetric expansions of methanol with CO_2
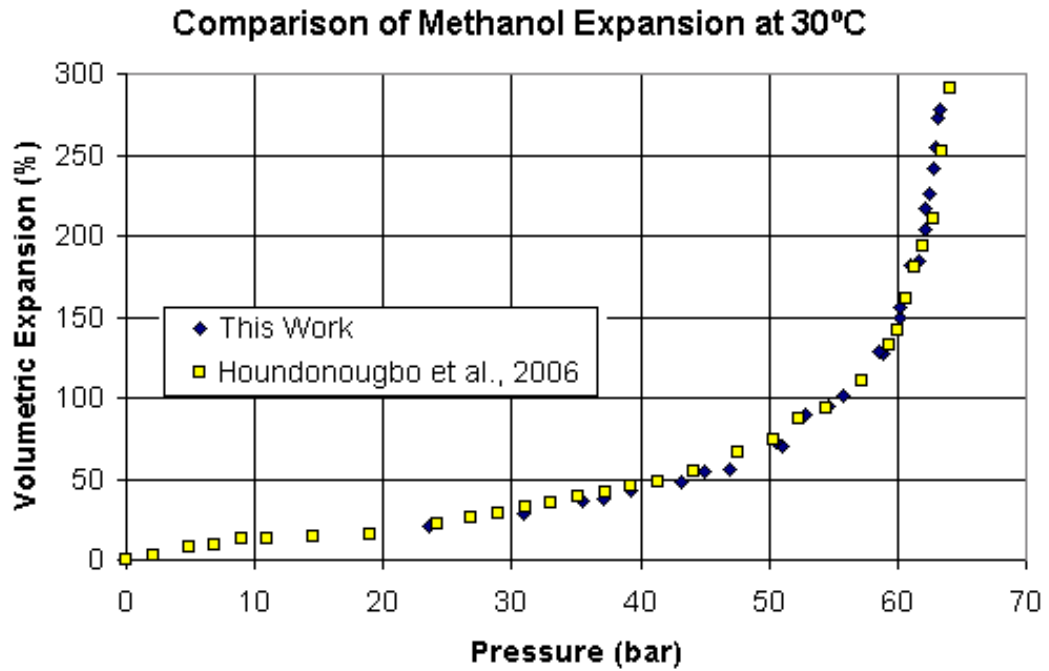
Figure B.5: Volumetric expansion of methanol with CO_2 at 30 ºC

166
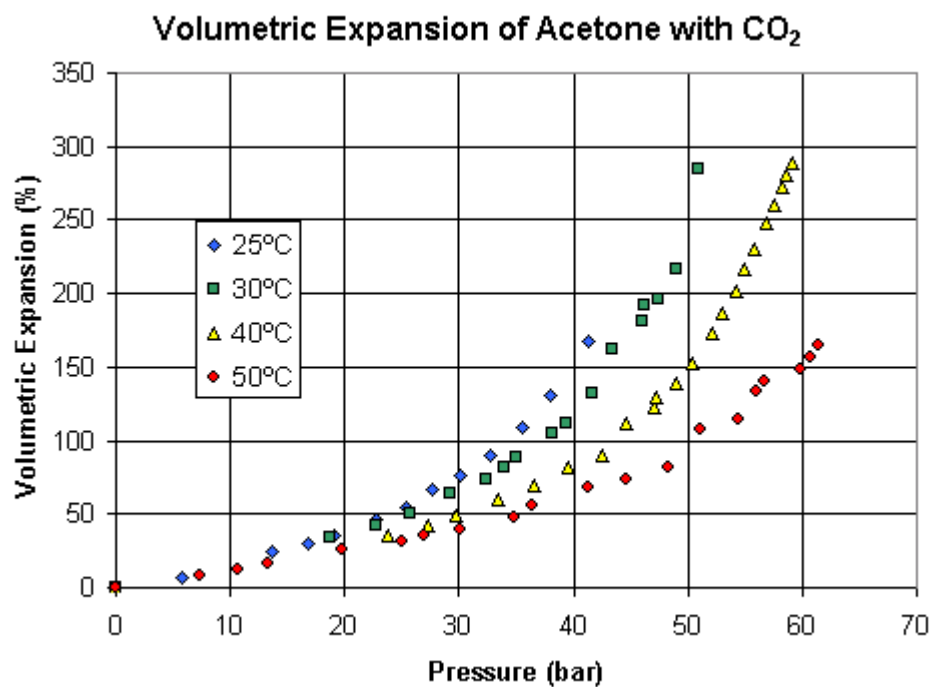
Figure B.6: Isothermal volumetric expansions of acetone with CO_2
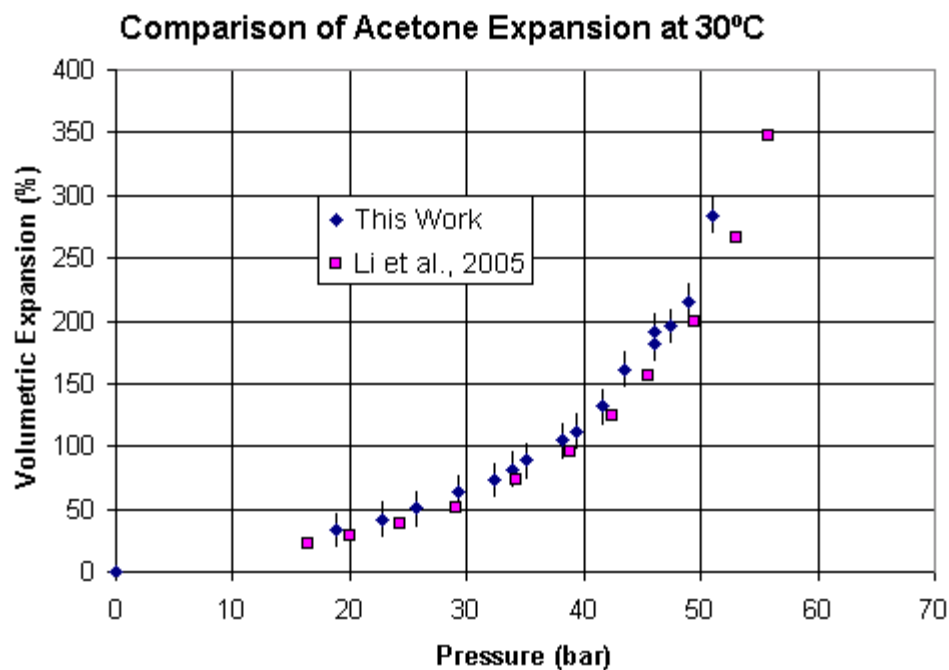
Figure B.7: Volumetric expansion of acetone with CO_2 at 30 °C

167
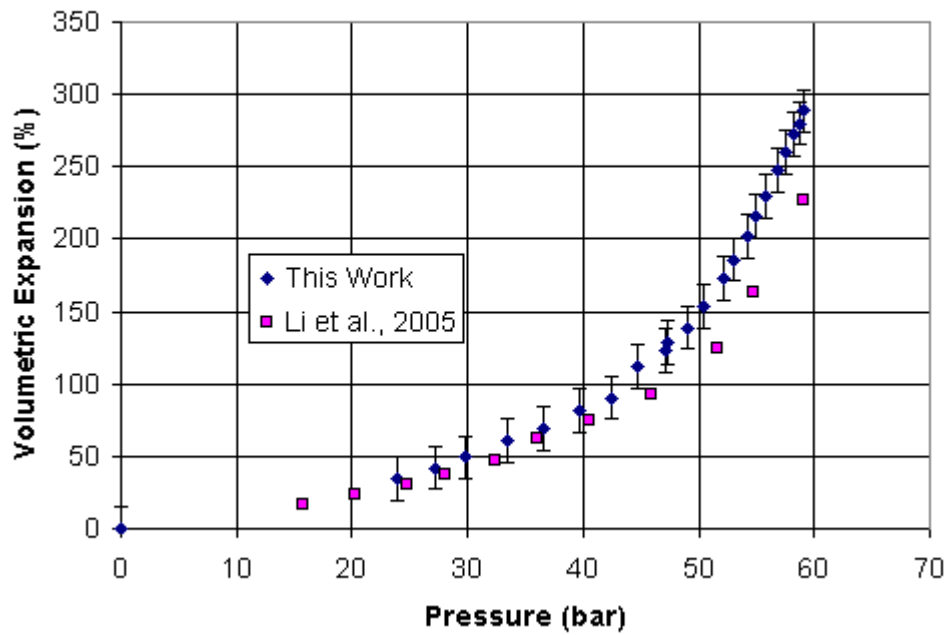
Figure B.8: Volumetric expansion of acetone with CO_2 at 40 ºC
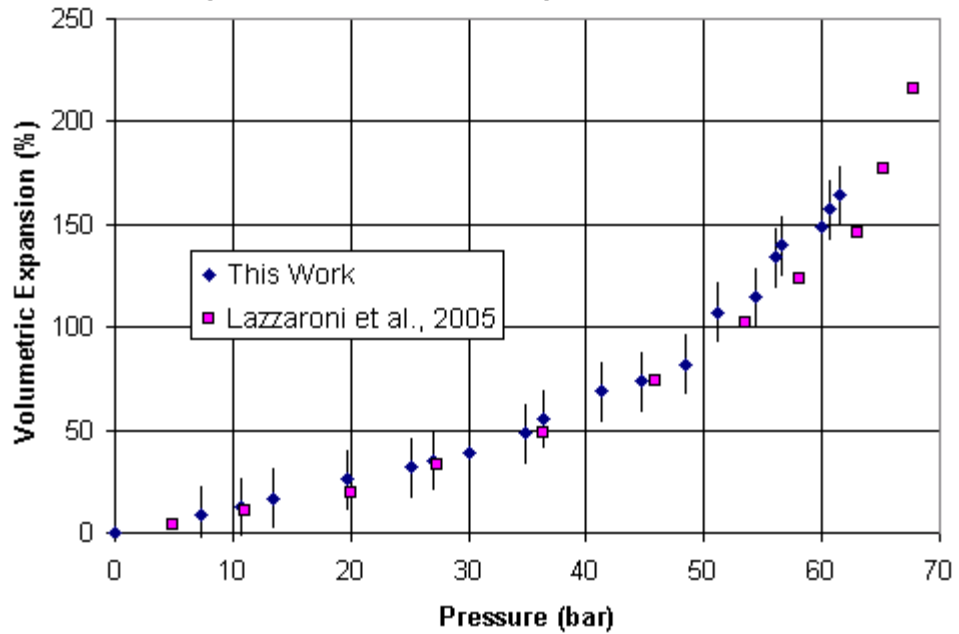
Figure B.9: Volumetric expansion of acetone with CO_2 at 50 ºC

168
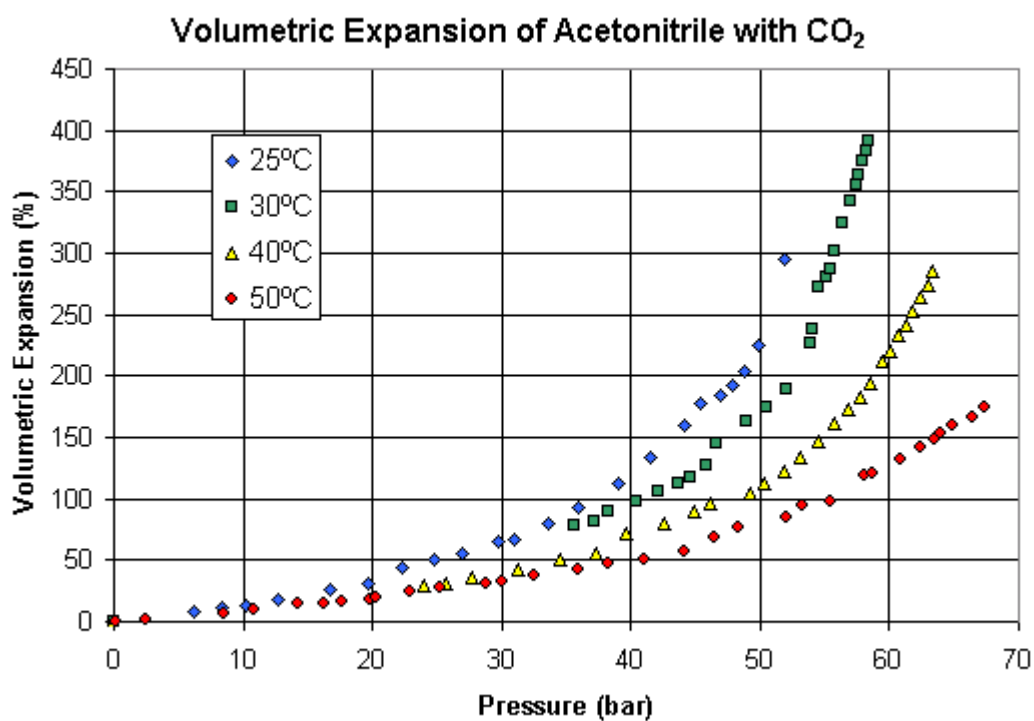
Figure B.10: Isothermal volumetric expansions of acetonitrile with CO_2
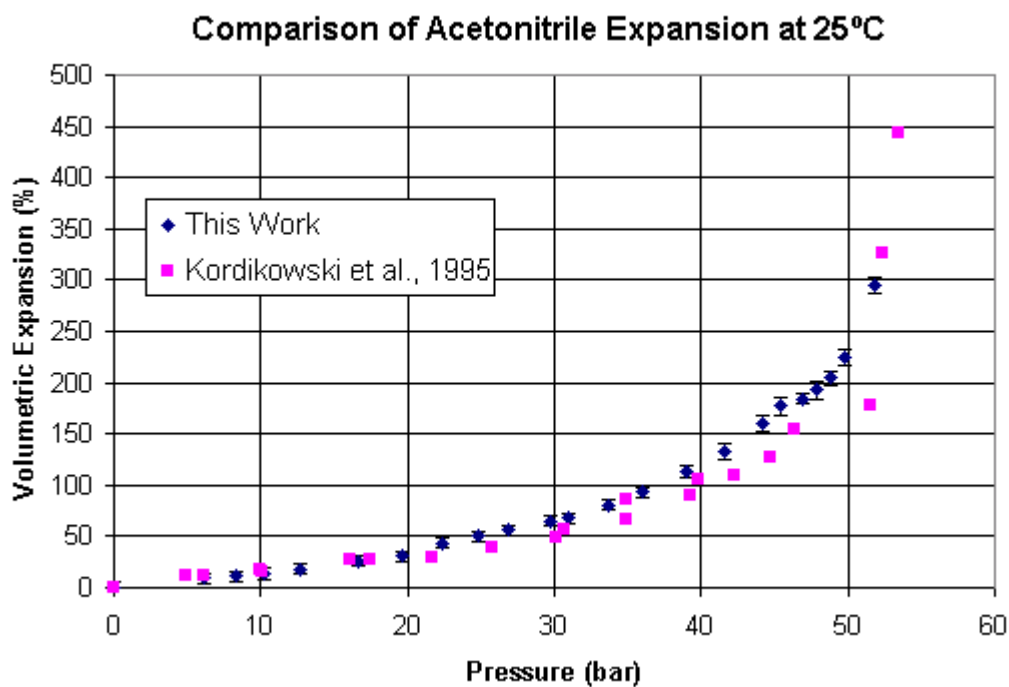
Figure B.11: Volumetric expansion of acetonitrile with CO_2 at 25 ºC

169
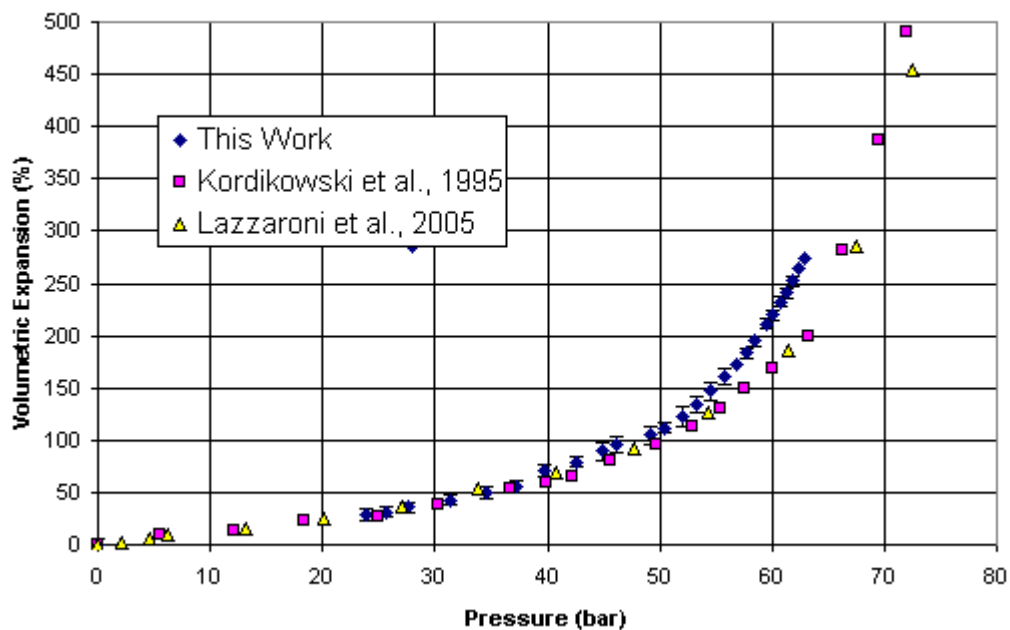
Figure B.12: Volumetric expansion of acetonitrile with CO_2 at 40 ºC

Figure B.13: Isothermal volumetric expansions of 1-octene with CO_2
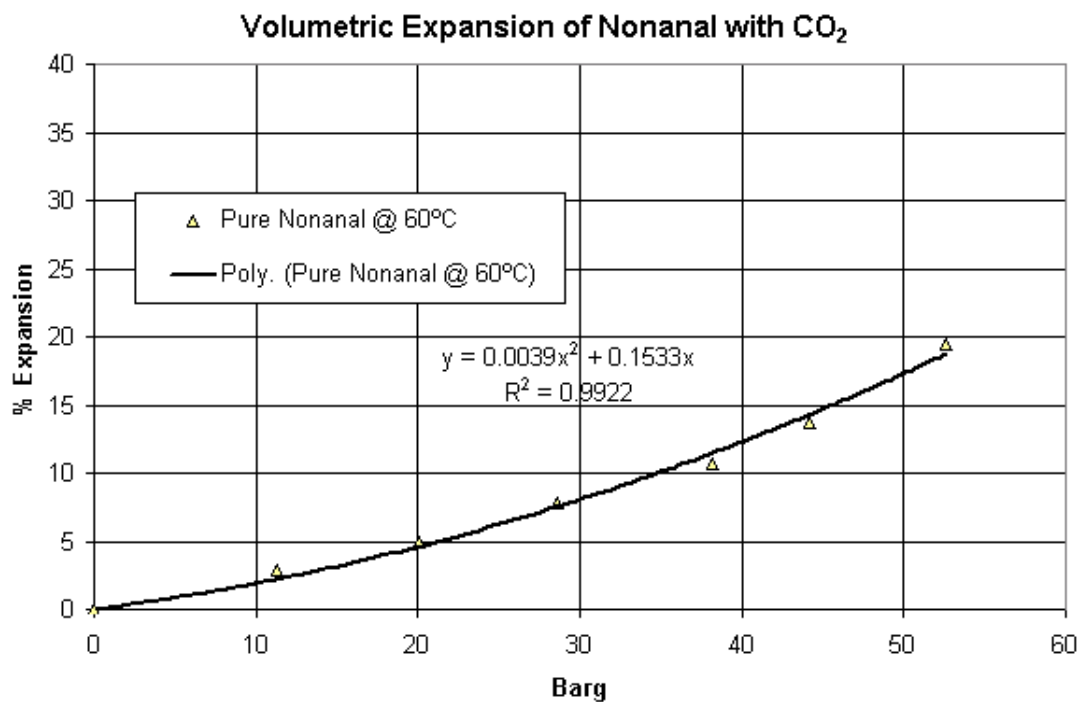
Figure B.14: Volumetric expansion of nonanal with CO_2 at 60 ºC
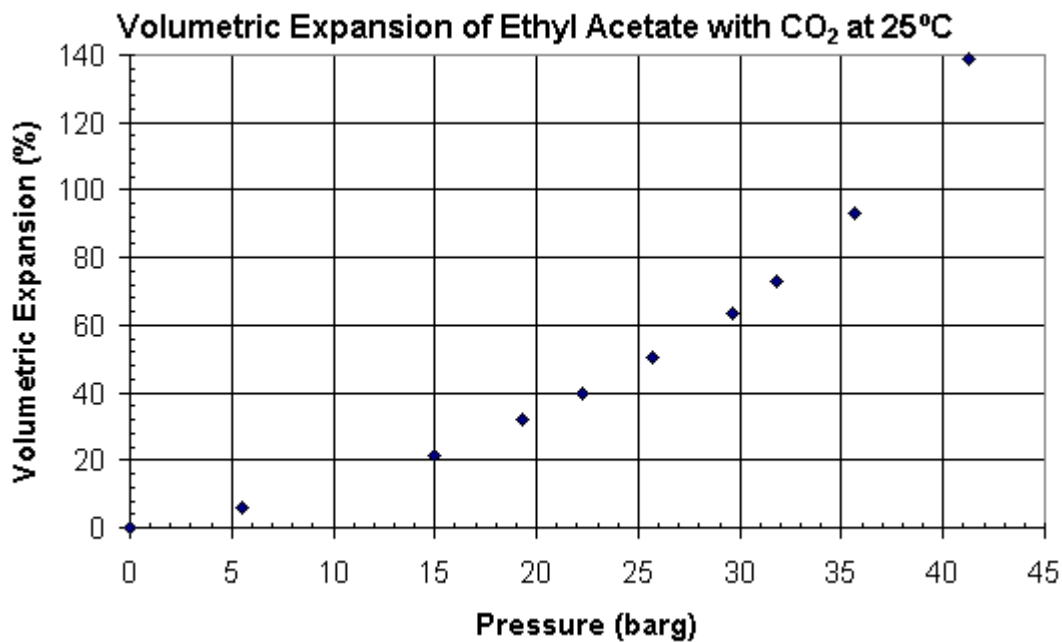
Figure B.15: Volumetric expansion of ethyl acetate with CO_2 at 25 ºC
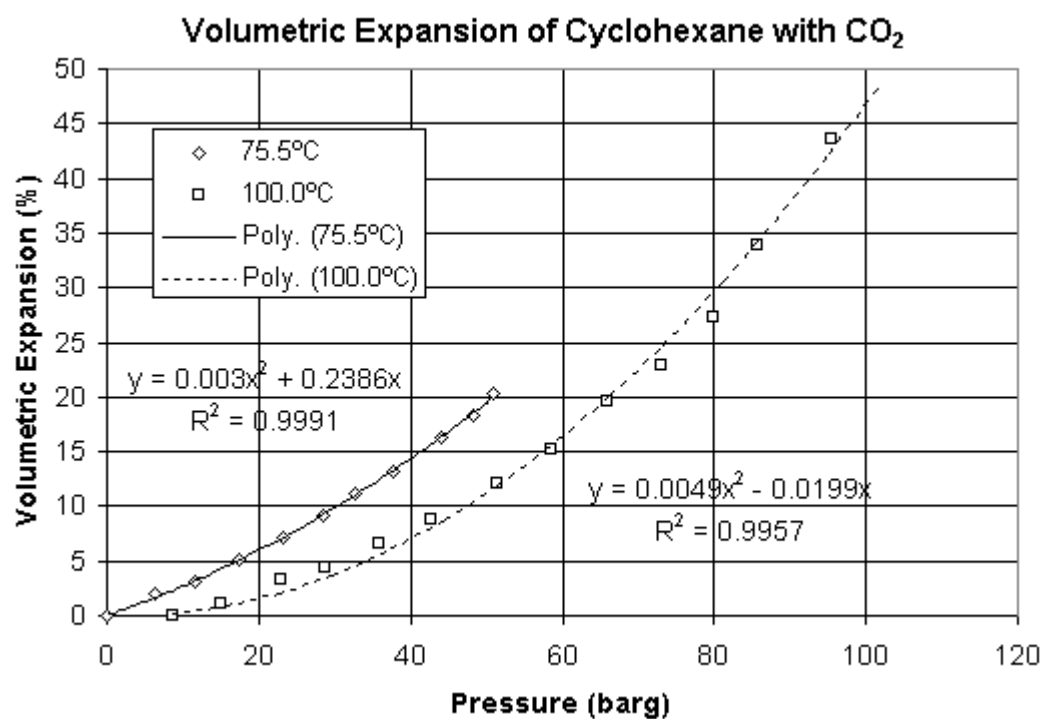
Figure B.16: Isothermal volumetric expansions of cyclohexane with CO_2

References

1. Abellon, R.D.; Kolar, Z.I.; den Hollander W.; de Goeij J.J.M.; Schouten, J.C.; van den Bleek, C.M. 1997. A single radiotracer particle method for the determination of solids circulation rate in interconnected fluidized beds. Powder Technol., 92, 53-60.

2. Al-Masry, W.; Ali, E.; Aqeel, Y. 2005. Determination of bubble characteristics in bubble columns using statistical analysis of acoustic sound measurement. Chem. Eng. Res. Des., 83, 1196-1207.

3. Alves, S.S.; Maia, C.I.; Vasconcelos, J.M.T.; Serralheiro, A.J. 2002. Bubble size in aerated stirred tanks. Chem. Eng. J., 84, 109-117.

4. Angst, R.; Kraume, M. 2006a. Particle distribution in stirred tanks: experimental and numerical investigations in different scales. 12th European Conference on Mixing. 8 p. Bologna, June 27-30.

5. Angst, R. Kraume, M. 2006b. Experimental investigations of stirred solid/liquid systems in three different scales: particle distribution and power consumption. Chem. Eng. Sci., 61, 2864-2870.

6. Barigou, M.; Greaves, M. 1992. Bubble size distributions in a mechanically agitated gas–liquid contactor, Chem. Eng. Sci., 47, 2009–2025.

7. Barrau, E.; Riviere, N.; Poupot, C.; Cartellier, A. 1999. Single and double optical probes in air-water two-phase flows: real time signal processing and sensor performance. Int. J. Multiphase Flow, 25, 229-256.

8. Bauckhage, K. 1996. Gleichzeitige Erfassung von Partikelmerkmalen und Eigenschaften mehrphasiger Stromungen mit Hilfe der Phasen-Doppler-Anemometrie. Chemie Ingenieur-Technik, 68, 253-266.

9. Bhaga, D.; Weber, M. E. 1981. Bubbles in viscous liquids: shapes, wakes, and velocities. J. Fluid Mech., 105, 61.

10. Blet, V.; Berne, P.; Chaussy, C.; Perrin, S.; Schweich, D. 1999. Characterization of a packed column using radioactive tracers. Chem. Eng. Sci., 54, 91-101.

11. Boelhouwer, J.G.; Piepers, H.W.; Drinkenburg, A.A.H. 2002. Nature and characteristics of pulsed flow in trickle bed reactors. Chem. Eng. Sci., 57, 4865-4876.

12. Bouaifi, M.; Hebrard, G.; Bastoul, D.; Rousten, M. 2001. A comparative study of gas hold-up, bubble size, interfacial area and mass transfer coefficients in stirred gas-liquid reactors and bubble columns. Chem. Eng. Proc., 40, 97-111

13. Boden, S.; Bieberle, M.; Hampel, U. Quantitative measurement of gas hold-up distribution in a stirred chemical reactor using X-ray cone-beam computed tomography. Chem. Eng. J., 139, 351-362.

14. Bolton, G.T.; Primrose, K.M. 2005. An overview of electrical tomographic measurements in pharmaceutical and related application areas. AAPS PharmSciTech. 6(2), Article 21, E-137-E143.

15. Bombac, A.; Zun, I.; Filipic, B.; Zumer, M. 1997. Gas-filled cavity structure and local void fraction distribution in aerated stirred vessel. AIChE J., 43(11), 2921-2931.

16. Boyer, C.; Duquenne, A.M.; Wild, G. 2002. Measuring techniques in gas-liquid and gas-liquid-solid reactors. Chem. Eng. Sci., 57, 3185-3215.

17. Brenn, G.; Braeske, H.; Durst, F. 2002. Investigation of the unsteady two phaseflow with small bubbles in a model bubble column using phase-Doppler anemometry. Chem. Eng. Sci., 57, 5143-5159.

18. Broering, S.; Fischer, J.; Korte, T.; Sollinger, S.; Luebbert, A. 1991. Flow structure of the dispersed gas phase in real multiphase chemical reactors investigated by a new ultrasound-Doppler technique. Can. J. Chem. Eng., 69, 1247–1256.

19. Brunner, E.; Hultenschmidt, W.; Schlichtharle, G. 1987. Fluid mixtures at high pressures IV. Isothermal phase equilibria in binary mixtures consisting of (methanol + hydrogen or nitrogen or methane or carbon monoxide or carbon dioxide). J. Chem. Thermodynamics, 19, 273-291.

20. Burgess J.M.; Calderbank P.H. 1975. The measurement of bubble parameters in two-phase dispersions I: the development of an improved probe technique. Chem. Eng. Sci., 30, 743-750.

21. Camarasa, E.; Vial, C.; Poncin, S.; Wild, G.; Midoux, N.; Bouillard, J. 1999. Influence of coalescence behaviour of the liquid and of gas sparging on hydrodynamics and bubble characteristics in a bubble column. Chem. Eng. Proc., 38, 329-344.

22. Cassanello, M.; Larachi, F.; Marie, M. N.; Guy, C.; Chaouki, J. 1995. Experimental characterization of the solid phase chaotic dynamics in three-phase fluidization. Ind. Eng. Chem. Res., 34, 2971-2980.

23. Cents, A.H.G.; Brilman, D.W.F.; Versteeg, G.F. 2005. Ultrasonic investigation of hydrodynamics and mas transfer in a gas-liquid(-liquid) stirred vessel. International Journal of Chemical Reactor Engineering. 3(A19), 1-32.

24. Chabot J.; Lee S.L.P.; Soria A.; De Lasa H.I. 1992. Interaction between bubbles and fiber optic probes in a bubble column", Can. J. Chem. Eng., 70, 61-68.

25. Chabot, J.; de Lasa, H.I. 1993. Gas holdups and bubble characteristics in a bubble column operated at high temperature. Ind. Eng. Chem. Res., 32, 2595-2601.

26. Chabot, J.; Farag, H.; De Lasa, H. 1998. Fluid dynamics of bubble columns at elevated temperature modelling and investigation with refractive fiber optic sensor. Chem. Eng. J., 70, 105-113.

27. Chang, C.J.; Randolph, A.D. 1990. Solvent Expansion and Solute Solubility Predictions in Gas-Expanded Liquids. *AIChE J.*, 36(6), 939.

28. Chanson, H. 2002. Air-water flow measurements with intrusive, phase-detection probes: can we improve their interpretation? J. Hydraulic Eng., March, 252-255.

29. Chaouki, J.; Larachi, F.; Dudukovic, M.P. 1997. Noninvasive tomographic and velocimetric monitoring of multiphase flows. Ind. Eng. Chem. Res., 36, 4476-4503.

30. Chen, Y.M.; Fan, L.S. 1989. Bubble breakage mechanisms due to collision with a particle in a liquid medium. Chem. Eng. Sci., 44, 117-132.

31. Chen, Z.; Zheng, C.; Feng, Y.; Hoffmann, H. 1998. Local bubble behavior in three-phase fluidized beds. Can. J. Chem. Eng., 76, 315-318.

32. Chen, J.; Kemoun, A.; Al-Dahhan, M. H.; Dudukovic, M. P.; Lee, D. J.; Fan, L.S. 1999. Comparative hydrodynamics study in bubble columns using computer-automated radioactive particle tracking (CARPT)/computed tomography (CT) and particle image velocimetry (PIV). Chem. Eng. Sci., 54, 2199-2207.

33. Choi K.H.; Lee W.K. 1990. Comparison of probe methods for measurement of bubble properties, Chem. Eng. Comm., 91, 35-47.

34. Couper, J.R.; Peavey, W.R.; Fair, J.R. 2004. Chemical Process Equipment: Selection and Design. Gulf Professional Publishing: 2nd Edition.

35. de la Fuente Badilla, J.C.; Peters, C.J.; de Swaan Arons, J. 2000. Volume Expansion in Relation to the Gas-Antisolvent Process. J. Supercrit. Fluids, 17, 13.

36. Deen, N.G. 2001. An Experimental and Computational Study of Fluid Dynamics in Gas-Liquid Chemical Reactors. Ph.D Thesis, Aalborg University, Denmark.

37. Deen, N.G; Hjertager, B.H. 2002. Particle image velocimetry measurements in an aerated stirred tank. Chem. Eng. Comm., 189, 1208-1221.

38. Delnoij, E.; Kuipers, J.A.M.; Van Swaaij, W.P.M. 1997. Computational fluid dynamics applied to gas–liquid contactors. Chem. Eng. Sci., 52, 3623–3638.

39. Dudukovic, M. P.; Devanathan, N.; Holub, R. 1991. Multiphase reactors: Models and experimental verification. Revue de l'Institut Francais du Petrole, 46, 439-465.

40. Ellingsen, K.; Risso, F. 2001. On the rise of an ellipsoidal bubble in water: oscillatory paths and liquid-induced velocity. J. Fluid Mech., 440, 235-268.

41. Euzen, J.P.; Fortin, Y. 1987. Partikelbewegung in einem Dreiphasenflie bett. Chemie-Ingenieur-Technik, 59, 416-419.

42. Fan L.S.; Yang G.Q.; Lee D.J.; Tsuchiya K.; Luo X. 1999. Some aspects of high-pressure phenomena of bubbles in liquids and liquid-solid suspensions. Chem. Eng. Sci., 54, 4681-4709.

43. Fangary, Y.S.; Barigou, M.; Seville, J.P.K.; Parker, D.J. 2000. Fluid trajectories in a stirred vessel of non-newtonian liquid using positron emission particle tracking. Chem. Eng. Sci., 55, 5969-5979.

44. Farag H.I.; Hjarbo K.; Mejdell T.; Hjarbo K.; Ege P.; Lysberg M.; Grislingaas A.; De Lasa H.I. 1997. Fiber optic and capacitance probes in turbulent fluidized beds. Chem. Eng. Comm., 157, 73-107.

45. Flaschel, E., Metzdorf, C., & Renken, A. (1987). Methode zur Messung der axialen Vermischung des Feststoffs in Flussigkeit/Feststoff-Wirbelschichten. Chemie-Ingenieur-Technik, 59, 494–496.

46. Ford, J.J; Heindel, T.J.; Jensen, T.C.; Drake, J.B. 2008. X-ray computed tomography of a gas-sparged stirred-tank reactor. Chem. Eng. Sci., 63, 2075-2085.

47. Fortin, Y. 1984. Reacteurs a lit fluidise triphasique: caracteristiques hydrodynamiques et melange des particules solides. These dedocteur-ingenieur, Universite de Paris VI, ENSPM, Solaize, France.

48. Frijlink, J. 1987. Physical aspects of gassed suspension reactors. Ph.D. Thesis, Delft University of Technology.

49. Frohlich, S.; Lotz, M.; Larson, B.; Lubbert, A.; Schugerl, K.; Seekamp, M. 1991. Characterization of a pilot plant airlift tower loop reactor: III. Evaluation of local properties of the dispersed gas phase during yeast cultivation and in model media. Biotechnology and Bioengineering, 38, 56-64.

50. Froystein, T. 1997. Flow imaging by gamma-ray Tomography: Data processing and reconstruction techniques. Frontiers in Industrial Process Tomography II, Delft, April 8-12.

51. Gallagher, P. M.; Coffey, M. P.; Krukonis, V. J.; Klasutis, N. 1989. Gas Antisolvent Recrstallization: New Process to Recrystallize Compounds Insoluble in Supercritical Fluids. In American Chemical Society Symposium Proceedings, No. 406; American Chemical Society: Washington, DC.

52. Garcia Ochoa, J., Khalfet, R., Poncin, S., & Wild, G. 1997. Hydrodynamics and mass transfer in a suspended solid bubble column with polydispersed high density particles. Chem.Eng. Sci., 52, 3827-3834.

53. Garcia-Salas, S.; Alfaro, M.E.R.P.; Porter, R.M.; Thalasso, F. 2008. Measurement of local specific interfacial area in bubble columns via a non-isokinetic withdrawal method coupled to electro-optical detector. Chem. Eng. Sci., 63, 1029-1038.

54. Gladden, L.F. 2003. Recent advances in MRI studies of chemical reactors: ultrafast imaging of multiphase flows. Topics in Catalysis 24, 19-28.

55. Gordon, C.; Leitner, W. 2004. Supercritical Fluids as Replacements for Conventional Organic Solvents. Chem. Oggi., 22 (9), 39.

56. Groen, J.S.; Mudde, R.F.; van den Akker, H.E.A. 1995. Time dependant behaviour of the flow in a bubble column. Trans. IChemE. A: Chem. Eng. Res. Des., 73, 615-620.

57. Guha, D.; Dudukovic, M.P.; Ramachandran, P.A.; Mehta, S.; Alvare, J. 2006. CFD-based compartmental modeling of single phase stirred-tank reactors. AIChE J., 52(5), 1836-1846.

58.   Guha, D.; Ramachandran, P.A.; Dudukovic, M.P. 2007. Flow field of suspended solids in a stirred-tank reactor by Lagrangian tracking. Chem. Eng. Sci., 62(22) 6143-6154.

59.   Guha, D. 2007. Hydrodynamics and mixing in single phase and liquid-solid stirred tank reactors. Ph.D Thesis, Washington University in St. Louis.

60.   Guha, D.; Ramachandran, P.A.; Dudukovic, M.P.; Derksen, J.J. 2008. Evaluation of large eddy simulation and Euler-Euler CFD models for solids flow dynamics in a stirred tank reactor. AIChE J., 54(3) 766-778.

61.   Gupta, P., Al-Dahhan, M. H., Dudukovic, M. P., & Mills, P. L. 2000.   A novel signal filtering methodology for obtaining liquid phase tracer responses from conductivity probes. Flow Measurement and Instrumentation, 11, 123–131.

62.   Han, L.; Al-Dahhan, M.H. 2007. Gas-liquid mass transfer in a high-pressure bubble column reactor with different sparger designs. Chem. Eng. Sci., 62, 131-139.

63.   Heindel, T.J. 2000. Gas flow regime changes in a bubble column filled with a fibre suspension. Can. J. Chem. Eng., 78, 1017-1022.

64.   Hills, J.H.; Darton, R.C. 1976. The rising velocity of a large bubble in a bubble swarm. Trans. IChemE. 54, 258-264.

65.   Hoffmann, A.C; Dechsiri, C.; van de Wiel, F, Dehling, H.G. 2005. PET investigation of a fluidized particle: spatial and temporal resolution and short term motion. Meas. Sci. Technol. 16, 851-858.

66.   Hogsett, S.; Ishii, M. 1997. Local two-phase flow measurements using sensor techniques. Nuclear Engineering and Design, 175, 15-24.

67.   Houndonougbo, Y.; Jin, H.; Rojogopalan, B.; Wong, K.; Kuczera, K.; Subramaniam., L.B. 2006. Phase Equilibria in Carbon Dioxide Expanded Solvents: Experiments and Molecular Simulations. J. Phys. Chem. B, 110, 13195.

68.   Hu, B.; Pacek, A.W.; Stitt, E.H.; Nienow, A.W. 2005. Bubble sizes in agitated air-alcohol systems with and without particles: turbulent and transitional flow. Chem. Eng. Sci., 60, 6371-6377.

69.   Hu, B.; Nienow, A.W.; Stitt, E.H.; Pacek, A.W. 2006. Bubble sizes in agitated solvent/reactant mixtures used in heterogeneous catalytic hydrogenation of 2-butene-1,4-diol. Chem. Eng. Sci., 61, 6765-6774.

70. Hu, B.; Nienow, A. W.; Stitt, E. H.; Pacek, A. W. 2007. Bubble sizes in agitated water-hydrophilic organic solvents for heterogeneous catalytic reactions. Ind. Eng. Chem. Res., 46, 4451-4458.

71. Hubers, J.L.; Striegel, A.C.; Heindel, T.J.; Gray, J.N., Jensen, T.C. 2005. X-ray computed tomography in large bubble columns. Chem. Eng. Sci. 60, 6124-6133.

72. Jiang, P.; Lin, T.J.; Luo, X.; Fan, L.S. 1995. Visualization of high pressure (21MPa) bubble column: bubble characteristics. Chem. Eng. Res. Des., 73, 269-274.

73. Jin, H.; Subramaniam, B. 2004. Homogeneous Catalytic Hydroformylation of 1-Octene in CO_2-Expanded Solvent Media. Chem. Eng. Sci., 59, 4887.

74. Jin, H.; Yang, S.; Guo, Z.; He, G.; Tong, Z. 2005. The axial distribution of holdups in an industrial-scale bubble column with evaluated pressure using γ-ray attenuation approach. Chem. Eng. J., 115, 45-50.

75. Joseph, S.; Shah, Y. T. 1986. Errors caused by tracer solubility in the measurement of gas phase axial dispersion. Can. J. Chem. Eng., 64, 380-386.

76. Joshi, J.B.; Patil, T.A.; Ranade, V.V.; Shah, Y.T. 1990. Measurement of hydrodynamic parameters in multiphase sparged reactors. Rev. Chem. Eng., 6(2-3), 73-227.

77. Joshi, J.B.; Ranade, V.V. 2003. Computational fluid dynamics for designing process equipment: expectations, current status, and path forward. Ind. Eng. Chem. Res., 42, 1115.

78. Julia, J.E.; Harteveld, W.K.; Mudde, R.F.; van den Akker, H.E.A. 2005. On the accuracy of the void fraction measurements using optical probes in bubbly flows. Rev. Sci. Instruments, 76, 13 p.

79. Kazenin, D.A.; Chepura, I.V.; Petrov, I.A.; Zhavoronkov, V.A. 2008. Hydrodynamics, mass transfer, and power consumption in air-core stirred tank reactors. Theoretical Foundations of Chem. Eng., 42(2), 118-124.

80. Kataoka, I.; Ishii, M.; Serizawa, A. 1986. Local formulation and measurements of interfacial area concentration in two-phase flow. Int. J. of Multiphase Flow, 12(4), 505.

81. Khopkar, A. R.; Rammohan, A. R.; Ranade, V. V.; Dudukovic, M. P. 2005. Gas-liquid flow generated by a Rushton turbine in a stirred vessel: CARPT/CT measurements and CFD simulations. Chem. Eng. Sci., 60, 2215-2229.

82. Kim, M.C.; Kim, K.Y.; Kim, S.; 2005. Improvement of impedance imaging for two-phase systems with boundary estimation approach in electrical impedance tomography. Can. J. Chem. Eng., 83, 55-63.

83. King, L.V. 1914. On the convection of heat from small cylinders in a stream of fluid, Philos. Trans. R. Soc. Lond. A 214 (14), 373-432.

84. Kordikowski, A.; Schenk, A. P.; Van Nielen, R. M.; Peters, C. J. 1995. Volume Expansions and Vapor-Liquid Equilibria of Binary Mixtures of a Variety of Polar Solvents and Certain Near-Critical Solvents. J. Supercrit. Fluids, 8, 205.

85. Kulkarni, A.; Joshi, J.; Ramkrishna, D. 2004. Determination of bubble size distribution in bubble columns using LDA. AIChE J., 50, 3068-3084.

86. Kumar, S.B.; Moslemian, D.; Dudukovic, M.P. 1995. A γ-ray tomographic scanner for imaging voidage distribution in two-phase flow systems. Flow Measurement and Instrumentation, 6, 61–73.

87. Laakonen, M.; Moilanen, P.; Aittamaa, J. 2005a. Local bubble size distributions in agitated vessels. Chem. Eng. J., 106, 133-143.

88. Laakonen, M.; Honkanen, M.; Saarenrinne P.; Aittamaa, J. 2005b. Local bubble size distributions, gas-liquid interfacial areas and gas holdups in a stirred vessel with particle image velocimetry. Chem. Eng. J., 109, 37-47.

89. Larachi, F.; Laurent, A.; Wild, G.; Midoux, N. 1991. Some experimental liquid saturation results in fixed-bed reactors operated under elevated pressure in cocurrent upflow and downflow of the gasand the liquid. Ind. Eng. Chem. Res., 30, 2404–2410.

90. Larachi, F.; Chaouki, J.; Kennedy, G. 1995. Three dimensional mapping of solids flow fields in multiphase reactors with RPT. AIChE J., 41, 439-443.

91. Lau, R.; Peng, R.; Velazquez-Vargas, L.G.; Yang, G.Q.; Fan, L.S. 2004. Gas-liquid mass transfer in high-pressure bubble columns. Ind. Eng. Chem. Res., 43, 1302-1311.

92. Lazzaroni, M. J.; Bush, D.; Brown, J. S.; Eckert, C. A. 2005. High-Pressure Vapor-Liquid Equilibria of Some Carbon Dioxide + Organic Binary Systems. J. Chem. Eng. Data, 50, 60.

93. Lee, S.L.P.; De Lasa, H.I. 1987. Phase holdups in three-phase fluidized beds. AIChE. J., 33, 1359-1370.

94. Lee, D.J.; Luo, X.; Fan, L.S. 1999. Gas disengagement technique in a slurry bubble column operated in the coalesced bubble regime. Chem. Eng. Sci., 54, 2227-2236.

95. Levenspiel, O. 2002. The Chemical Reactor Omnibook. OSU Book Stores, Inc. p. 42.1.

96. Li, Z.; Xia, Y.; Liu, X.; Deng, X.; Hu, D. 2005. Study of the Liquid Phase Volume Expansion for CO_2/Organic Solvent Systems. Chin. J. Chem. Eng., 13(4), 504.

97. Lim K. S.; Agarwal P. K. 1992. Bubble velocity in fluidized beds: the effect of non-vertical bubble rise on its measurement using submersible probes and its relationship with bubble size. Powder Technology, 69, 239-248.

98. Lim, M.H.M.; Sederman, A.J.; Gladden, L.F.; Stitt, E.H. 2004. New insights to trickle and pulse flow hydrodynamics in trickle-bed reactors using MRI. Chem. Eng. Sci., 59, 5403-5410.

99. Lin, T.J.; Lou, C.T. 2007. Reflection-based localized surface plasmon resonance fiber-optic probe for chemical and biochemical sensing at high-pressure conditions. J. of Supercritical Fluids, 41, 317-325.

100. Linek, V.; Kordac, M.; Fujasova, M.; Moucha, T. 2004. Gas-liquid mass transfer coefficient in stirred tanks interpreted through models of idealized eddy structure of turbulence in the bubble vicinity. Chem. Eng. Proc., 43, 1511-1517.

101. Liu, T.J. 1993. Bubble size and entrance length effects on void development in a vertical channel. Int. J. Multiphase Flow 19, 99-113.

102. Liu, Y.J.; Han, L.C.; Luo, H.A.; Al-Dahhan, M.; Dudukovic, M.P. 2006. Measurement of gas hold-up distribution and digital color image reconstruction for standard gas-liquid rushton stirred tank with Cs-137 γ-CT. J. Chem. Eng. of Chinese Universities, 4(20), 648-652.

103. Lu, W.M.; Ju, S.J. 1987. Local gas holdup, mean liquid velocity and turbulence in an aerated stirred tank using hot-film anemometry. Chem. Eng. J., 35, 9-17.

104. Luo, X.; Lee, D. J.; Lau, R.; Yang, G.; Fan, L. 1999. Maximum stable bubble size and gas holdup in high-pressure slurry bubble columns. AIChE J., 45 (4), 665.

105. Machon, V.; Pacek, A.W.; Nienow, A.W. 1997. Bubble sizes in electrolyte and alcohol solutions in a turbulent stirred vessel. Trans. IChemE., 75(A) 339-348.

106. Manikowski, M.; Wulff, H.; Bodemeier, S.; Lubbert A. 1993. Gas-phase flow distribution in a stirred tank bioreactor. 3rd International Conference on Bioreactor and Bioprocess Fluid Dynamics. 27-33.

107. Mann, R.; Dickin, F. J.; Wang, M.; Dyakowski, T.; Williams, R. A.; Edwards, R. B.; Forrest, A. E.; Holden, P. J. 1997. Application of electrical resistance tomography to interrogate mixing processes at plant scale. Chem. Eng. Sci., 52, 2087-2097.

108. Martin, M.; Montes, F.J.; Galan, M.A. 2008. Bubbling process in stirred tank reactors I: agitator effect on bubble size, formation and rising. Chem. Eng. Sci., 63, 3212-3222.

109. Matsuura, A.; Fan, L.S. 1984. Distribution of bubble properties in a gas–liquid–solid fluidized bed. AIChE J., 30, 894-903.

110. Middleton, J.C. 1985. Gas-liquid dispersion and mixing. Mixing in the Process Industries. Edited by Harnby, N.; Edwards, M.F.; Nienow, A.W. Butterworths & Co. Ltd.

111. Miyahara, T.; Hamaguchi, M.; Sukeda, Y.; Takahashi, T. 1986. Size of bubbles and liquid circulation in a bubble column with a draught tube and a sieve plate. Can. J. Chem. Eng., 64, 718-725.

112. Menzel, T.; In Der Weide, T.; Staudacher, O.; Wein, O.; Onken, U. 1990. Reynolds shear stress for modeling of bubble column reactors. Ind. Eng. Chem. Res., 29, 988-994.

113. Montante, G.; Paglianti, A.; Magelli, F. 2007. Experimental analysis and computational modeling of gas-liquid stirred vessels. Trans. IChemE., 85(A5), 647-653.

114. Morud, K.E; Hjertager, B.H. 1996. LDA measurement and CFD modeling of gas-liquid flow in a stirred vessel. Chem. Eng. Sci., 51(2), 233-250.

115. Mudde, R.F.; Groen, J.S.; van den Akker, H.E.A. 1998. Application of LDA to bubbly flows. Nuclear Engineering and Design, 184, 329-338.

116. Mueller, S.G.; Werber, J.R.; Al-Dahhan, M.H.; Dudukovic, M.P. 2007. Using a fiber-optic probe for the measurement of volumetric expansion of liquids. Ind. Eng. Chem. Res., 46(12), 4330.

117. Musie, G.; Wei, M.; Subramaniam, B.; Busch, D. 2001. Catalytic Oxidations in Carbon Dioxide-Based Reaction Media, Including Novel CO_2-Expanded Phases. Coord. Chem. Rev. 2001, 219-221, 789.

118. Munholand, L.; Soucy, G. 2005. Comparison of four conductive needle probe designs for determination of bubble velocity and local gas holdup. Rev. Sci. Instruments, 76, 6 p.

119. Nassar, A.F.; Zivkovic, G.; Genenger, B.; Durst, F. 2004. PDA measurements and numerical simulation of turbulent two-phase flow in stirred vessels. Bubbly Flows: Analysis, Modeling and Calculations. 337-351.

120. Nedeltchev, S.; Kumar, S.B.; Dudukovic, M.P. 2003. Flow regime identification in a bubble column based on both Kolmogorov entropy and quality of mixedness derived from CARPT data. Can. J. Chem. Eng., 81, 367-374.

121. Nienow, A.W.; Wisdom, D.J.; Middleton, J.C. 1997. The effect of scale and geometry on fooding, recirculation, and power in gassed stirred vessels. Proc. Eur. Conf. On Mixing, Paper F1, Cambridge.

122. Paglianti, A.; Pintus, S. 2001. An impedance probe for measurement of liquid hold-up and mixing time in two/three-phase stirred tank reactors. Experiments in Fluids, 31, 417-427.

123. Peng, D.Y.; Robinson, D.B. 1976. A New Two-Constant Equation of State. Ind. Eng. Chem., 15 (1), 59.

124. Peters, M.H.; Fan, L.S.; Sweeney, T.L. 1983. Study of particle ejections in the freeboard region of a fluidized bed with an image carrying probe. Chem. Eng. Sci., 38, 481-485.

125. Rammohan, A.R.; Kemoun, A.; Al-Dahhan, M.H.; Dudukovic, M.P. 2001. A Lagrangian description of flow in stirred tanks via computer-automated radioactive particle tracking (CARPT). Chem. Eng. Sci., 56, 2629-2639.

126. Rammohan, A.R. 2002. Characterization of single and multiphase flows in stirred tank reactors. Ph.D Thesis, Washington University in St. Louis.

127. Reese, J.; Mudde, R. F.; Lee, D. J.; Fan, L.S. 1996. Analysis of multiphase systems through particle image velocimetry. AIChE Symposium Series, 92(310), 161-167.

128. Reinecke, N.; Mewes, D. 1997. Investigation of the two-phase flow in trickle-bed reactors using capacitance tomography. Chem. Eng. Sci, 52, 2111-2127.

129. Reith, T.; Beek, W.J. 1968. Gas holdups, interracial areas and mass transfer coefficients in gas-liquid contactors. 4th European Symposium on Chemical Reaction Engineering, 191-204.

130. Roizard, C.; Poncin, S.; Lapicque, F.; Py, X.; Midoux, N. 1999.Behavior of fine particles in the vicinity of a gas bubble in a stagnant and a moving fluid. Chem. Eng. Sci., 54, 2317-2323.

131. Scargiali, F.; D'Orazio, A.; Grisafi, F.; Brucato, A. 2007. Modeling and simulation of gas-liquid hydrodynamics in mechanically stirred tanks. Trans. IChemE., 85(A5), 637-646.

132. Schafer, M.; Wachter, P.; Durst, F. 2000. Experimental investigation of local bubble size distribution in stirred vessels using Phase Doppler Anemometry. 10th European Conference on Mixing. 205-212.

133. Schmitz, D.; Mewes, D. 2000. Tomographic imaging of transient multiphase flow in bubble columns. Chem. Eng. J., 77, 99-104.

134. Schweitzer, J.M.; Bayle, J.; Gauthier, T. 2001. Local gas hold-up measurements in fluidized bed and slurry bubble columns. Chem. Eng. Sci., 56, 1103-1110.

135. Simonnet, M.; Gentric, C.; Olmes, E.; Midoux, E. 2007. Experimental determination of the drag coefficient in a swarm of bubbles. Chem. Eng. Sci., 62, 858-866.

136. Snieders, F.F.; Hoffmann, A.C.; Cheesman, D.; Yates, J.G.; Stein, M.; Seville, J.P.K. 1999. The dynamics of large particles in a four-compartment interconnected fluidized bed. Powder Technol., 101, 229-239.

137. Sommerfield, M; Decker, S. 2004. State of the art and future trends in CFD simulation of stirred vessel hydrodynamics. Chem. Eng. Technol., 27(3), 215-224.

138. Stegeman, D.; Ket, P.J.; Kolk, H.A. v.d.; Bolk, J.W.;Knop, P.A.; Westerterp, K.R. 1995. Interfacial area and gas holdup in an agitated gas-liquid reactor under pressure. Ind. Eng. Chem. Res., 34(1), 59-71.

139. Stein, M.; Ding, Y.L.; Seville, J.P.K.; Parker, D.J. 2000. Solids motion in bubbling gas fluidized beds. Chem. Eng. Sci., 55, 291-300.

140. Stitt, E.H. 2002. Alternative multiphase reactors for fine chemicals: a world beyond stirred tanks? Chem. Eng. J., 90, 47-60.

141. Stolojanu, V.; Prakash, A. 1997. Hydrodynamic measurements in a slurry bubble column using ultrasonic techniques. Chem. Eng. Sci., 52, 4225–4230.

142. Stravs, A.A.; Wahl, J.; von Stokar, U.; Reilly, P.J. 1987. Development of an ultrasonic pulse reflection method for measuring relative size distributions of air bubbles in aqueous solutions. Chem. Eng. Sci., 42, 1677-1987.

143. Subramaniam, B.; Lyon, C. J.; Arunajatesan, V. 2002. Environmentally Benign Multiphase Catalysis with Dense Phase Carbon Dioxide. Appl. Catal., 37, 279.

144. Sudiyo, R.; Andersson, B. 2007. Bubble trapping and coalescence at the baffles in stirred tank reactors. AIChE J., 53(9), 2232-2239.

145. Sun, H.; Mao, Z.S.; Yu, G. 2006. Experimental and numerical study of gas hold-up in surface aerated stirred tanks. Chem. Eng. Sci., 61, 4098-4110.

146. Taboada, B.; Vega-Alvarado, L.; Cordova-Aguilar, M.S.; Galindo, E.; Corkidi, G. 2006. Semi-automatic image analysis methodology for the segmentation of bubbles and drops in complex dispersions occurring in bioreactors. Experiments in Fluids, 41, 383-392.

147. Tang, W.T.; Fan, L.S. 1989. Hydrodynamics of a three-phase fluidized bed containing low-density particles. AIChE. J., 35, 355-364.

148. Tatterson, G.B.; Kyser, E.A. 1991. Mixing in fed-batch and continuous flow processes in nonstandard geometries. AIChE J., 37(2), 269.

149. Tayebi, D; Svenson, H.; Grislingas, A.; Mejdell, T.; Johannessen, K. 1999. Dynamics of fluidized bed reactors. Development and application of a new multi-fiber optical probe. Chem. Eng. Sci., 54, 2113-2122.

150. Thatte, A.R.; Ghadge, R.S.; Patwardhan, A.W.; Joshi, J.B.; Singh, G. 2004. Local gas holdup measurement in sparged and aerated tanks by γ-ray attenuation technique. Ind. Eng. Chem. Res., 43(17), 5389-5399.

151. Toye, D. 1996. Etude de l'ecoulement ruisselant dans les lits fixes par tomographie a rayons X. These de Doctorat en Sciences Appliquees, Universite de Liege, Belgium.

152. Utiger, M.; Stuber, F.; Duquenne, A.M.; Delmas, H.; Guy, C. 1999. Local measurements for the study of external loop airlift hydrodynamics. Can. J.Chem. Eng., 77, 375–382.

153. Utomo, M.B.; Warsito, W.; Sakai, T.; Uchida, S. 2001. Analysis of distributions of gas and TiO_2 particles in slurry bubble column using ultrasonic computed tomography. Chem. Eng. Sci., 56, 6073-6079.

154. Van Barneveld, J.; Smit, W.; Oosterhuis, N.M.G; Pragt, H.S. 1987. Measuring the liquid circulation time in a large gas-liquid contactor by means of a radio pill. Part 1. Flow pattern and mean circulation time. Ind. Eng. Chem. Res., 26(11), 2185-2192.

155. Veera, U.P.; Joshi, J.B., 2000. Measurement of gas hold-up profiles in bubble column by gamma ray tomography. Chem. Eng. Res. Des., 78, 425-434.

156. Vial, C.; Camarasa, E.; Poncin, S.; Wild, G.; Midoux, N. Bouillard, J. 2000. Study of hydrodynamic behaviour in bubble columns and external loop airlift reactors through analysis of pressure fluctuations. Chem. Eng. Sci., 55, 2957-2973.

157. Vial, C., Poncin, S., Wild, G., & Midoux, N. 2001. A simple method for regime identification and flow characterization in bubble columns and airlift reactors. Chem. Eng. Proc., 40, 35-151.

158. Vrabel, P.; van der Lans, R.G.J.M.; Luyben, K.C.A.M.; Boon, L.; Nienow, A.W. 2000. Mixing in large-scale vessels stirred with multiple radial or radial and axial up-pumping impellers: modeling and measurements. Chem. Eng. Sci., 55, 5881-5896.

159. Wang, G.; Ching, C.Y. 2001. Measurement of multiple gas-bubble velocities in gas–liquid flows using hot-film anemometry. Experiments in Fluids, 31, 428-439.

160. Wang, W.; Mao, Z.; Chao, Y. 2006a. Experimental and numerical investigation on gas holdup and flooding in an aerated stirred tank with Rushton impeller. Ind. Eng. Chem. Res., 45, 1141-1151.

161. Wang, F.; Mao, Z.S.; Wang, Y.; Yang, C. 2006b. Measurement of phase holdups in liquid-liquid-solid three-phase stirred tanks and CFD simulation. Chem. Eng. Sci., 61, 7537-7550.

162. Warsito, W.; Ohkawa, M.; Kawata, N.; Uchida, S. 1999. Cross-sectionaldistributions of gas and solid holdups in slurry bubble column investigated by ultrasonic computed tomography. Chem. Eng. Sci., 54, 4711-4728.

163. Warsito, W.; Fan, L.S. 2005. Dynamics of spiral bubble plume motion in the entrance region of bubble columns and three-phase fluidized beds using 3D ECT. Chem. Eng. Sci., 60, 6073-6084.

164. Wei, M.; Musie, G.T.; Busch, D.H.; Subramaniam, S. 2002. CO_2-expanded solvents: unique and versatile media for performing homogeneous catalytic reactions. J. Am. Chem. Soc., 124(11), 2513-2517.

165. Werther, J.; Hage, B.; Rudnick, C. 1996. A comparison of laser Doppler and single-fiber reflection probes for the measurement of the velocity of solids in a gas-solid circulating fluidized bed. Chem. Eng. & Proc., 35, 381-391.

166. Wu Q.; Ishii M. 1999. Sensitivity study on double-sensor conductivity probe for the measurement of interfacial area concentration in bubbly flow. Int. J. Multiphase Flow, 25, 155-173.

167. Xu, S.; Qu, Y.; Chaouki, J.; Guy, C. 2005. Characterization of Homogeneity of Bubble Flows in Bubble Columns Using RPT and Fibre Optics. Int. J. of Chem. Reactor Eng., 3, A54, 1-14.

168. Xue J.; Al-Dahhan M.H.; Dudukovic M. P.; Mudde R. F. 2003. Bubble dynamics measurements using four-point optical probe. Can. J. Chem. Eng., 81(3-4), 375-381.

169. Xue, J. 2004. Bubble velocity, size and interfacial area measurements in bubble columns. Ph.D Thesis, Washington University in St. Louis.

170. Xue, J.; Al-Dahhan, M.; Dudukovic, M.P.; Mudde, R.F. 2008a. Bubble velocity, size, and interfacial area measurements in a bubble column by four-point optical probe. AIChE J., 54(2), 350-363.

171. Xue, J.; Al-Dahhan, M.; Dudukovic, M.P.; Mudde, R.F. 2008b. Four-point optical probe for measurement of bubble dynamics: validation of the technique. Flow Measurement and Instrumentation, 19(5), 293-300.

172. Yang, G.Q.; Luo, X.; Lau, R.; Fan, L.S. 2000. Bubble formation inhigh-pressure liquid–solid suspensions with plenum pressure fluctuation. AIChE J., 46, 2162–2174.

173. Yang, W.; Wang, J.; Wang, T.; Yong, J. 2001. Experimental study on gas-liquid interfacial area and mass transfer coefficient in three-phase circulating fluidized beds. Chem. Eng. J., 84, 485-490.

174. Yang, G.Q.; Du, B.; Fan, L.S. 2007. Bubble formation and dynamics in gas-liquid-solid fluidization – a review. Chem. Eng. Sci., 62, 2-27.

Vita

Sean G. Mueller

Date of Birth   November 26, 1982

Place of Birth   Saint Louis, Missouri

Degrees   B.S. Magna Cum Laude, Chemical Engineering, May 2005
M.S. Energy, Environmental and Chemical Engineering,
December 2007
Ph.D. Energy, Environmental and Chemical Engineering,
August 2009

Professional   American Institute of Chemical Engineers
Societies   Tau Beta Pi
National Society of Collegiate Scholars

Publications   Mueller, S.G., Stallbaumer, P.J., Slade, D.A., Stagg-Williams, S.M. 2005. Segregation of Pt and Re During CO_2 Reforming of CH_4. Catalysis Letters, 103(1-2), 69-74.

Mueller, S.G., Werber, J.R., Al-Dahhan, M.H., Dudukovic, M.P. 2007. Using a Fiber-Optic Probe for the Measurement of Volumetric Expansion of Liquids. Industrial and Engineering Chemistry Research. 10(12), 4330-4334.

August 2009

Optical Measurements in G/L-STs,   Mueller,   Ph.D. 2009